

ALMA MATER STUDIORUM
UNIVERSITY OF BOLOGNA
Scuole di Ingegneria e Architettura · Sede di Forlì

MASTER's DEGREE IN AEROSPACE ENGINEERING
Class LM-20

Graduation Thesis in:
Simulation and Modeling in Fluid Dynamics

On the Momentum and Energy exchanges
in wind-wave interfacial flow

Candidate:
Federica Romoli

Supervisor:
Prof. Andrea Cimarelli

III Session
Academic year 2017/2018

Abstract

Nowadays, there is a particular interest in the problem of understanding the interaction phenomena between atmospheric wind and ocean waves. This is due to the fact that a better knowledge of these interactions might enhance our estimates of the momentum and energy exchanges at the air-sea interface. A full understanding of this mechanism might improve actual models for wave and atmosphere prediction, climate forecast and loads estimation on marine structures such as ships and offshore platforms. In this study different numerical simulations have been taken into account. In order to have a first insight of the momentum and heat transfers across the air, Direct Numerical Simulation (DNS) of a fully developed turbulent open channel with passive heat transfer is performed. Then momentum and passive heat transfers across sheared wind-driven gas-liquid interface have been investigated by means of DNSs of two-phase flows. The detailed analysis of the mean profiles, the kinetic and temperature budget equations and the two-points statistics allows to understand how the dynamic of a turbulent boundary layer is affected by ocean waves. At the mean time, it is possible to study how the structure of the ocean waves are influenced by the state of the turbulent boundary layer creating them.

Contents

1	General introduction	9
1.1	Air-water interaction	9
1.2	Wind waves	10
1.2.1	Wave classification	10
1.2.2	Wind wave generation and growth	12
2	State of the art	15
2.1	Atmosphere-ocean wave modeling system for evaluating air-sea interaction	15
2.1.1	Surface layer Parametrization	16
2.1.2	Wave model (WAM)	18
2.1.3	Weather Research Forecasting (WRF)	19
2.1.4	Two-way coupling between WAM and WRF	20
2.2	Turbulent boundary layer theory	21
2.3	Heat transfer as a passive scalar	25
3	Governing equations and numerical tools	27
3.1	Single Phase flow	27
3.1.1	Governing equations	27
3.1.2	PimpleFoam Solver	29
3.1.3	Modified PimpleFoam Solver	30
3.2	Two-Phase flow	31
3.2.1	The Volume of Fluid method	32
3.2.2	VOF problems with Conventional Discretizations	33
3.2.3	Governing equation of a two-phase flow	37
3.2.4	IneterFoam and Modified InterFoam Solvers	41
4	Turbulent open channel	43
4.1	Simulation details	43
4.1.1	Physical system and Mesh properties	43
4.1.2	Boundary conditions	45

4.1.3	Initial conditions	45
4.1.4	General simulation characteristics	47
4.2	Results	48
4.2.1	Turbulent structures	49
4.2.2	Statistics	53
5	Turbulent water channel	69
5.1	Simulation details	69
5.1.1	Physical system and Mesh properties	69
5.1.2	Boundary conditions	72
5.1.3	Initial conditions	73
5.1.4	General simulation characteristics	75
5.2	Results	77
5.2.1	Wind turbulent structures	77
5.2.2	Statistics	80
5.2.3	Wave height statistics	96
6	Laminar water channel	103
6.1	Initial Condition	103
6.2	Transitional wave state	104
7	Conclusions	107

List of Figures

1.1	Ocean wave classification	11
1.2	Frequency and period of ocean waves	11
1.3	Wind wave formation process	12
1.4	Representation of Miles-Phillips theory	13
2.1	CHAOS scheme	16
2.2	Communication between WRF and WAM is depicted in the multi-level flowchart.	21
2.3	Comparison between laminar and turbulent mean velocity profiles.	22
2.4	Inner scaling of a turbulent mean velocity profiles.	24
2.5	The thermal boundary layer regions	26
3.1	Example of indicator Scalar function distribution through the domain	33
3.2	Donor-acceptor scheme	34
3.3	Controlled dowinding improvements.	36
3.4	Forcing acting on the water molecule	38
3.5	Surface tension force	39
3.6	Surface tension force	40
4.1	Flow geometry	44
4.2	yz slices of the streamwise velocity	46
4.3	Streaks and spanwise vortexes interaction mechanism	50
4.4	Hairpin vortexes formation	50
4.5	Streaks and spanwise vortices	51
4.6	Two points correlations of wall-normal and streamwise velocity fluctuations	52
4.7	3D visualization of thermal streaks computed for $T = 292K$	53
4.8	Slices	54
4.9	Mean velocity profile	56
4.10	Turbulent intensity profiles.	57
4.11	Shear stress profiles.	57

4.12	Budget of turbulent kinetic energy	60
4.13	Velocity spectra in the spanwise direction.	61
4.14	Velocity spectra in the streamwise directions	62
4.15	Mean temperature profile	63
4.16	Streamwise turbulent heat flux and intensity of heat transfer profile.	64
4.17	Budget of turbulent heat transfer	66
4.18	Temperature spectra	67
5.1	Flow geometry	70
5.2	Dimensionless resolution in the wall-normal direction	72
5.3	Initial temperature and velocity fields	74
5.4	Streaks and spanwise vortices	78
5.5	Two points correlations of wall-normal and streamwise velocity fluctuations	79
5.6	3D visualization of thermal streaks computed for $T = 302K$	80
5.7	Slices	81
5.8	time evolution of \tilde{Re}_τ , \tilde{Nu} and \tilde{h}_{rms}	82
5.9	Plots of mean velocity gradient and mean velocity profiles where the red circle, localized at $y = 0.1508m$, identifies the interface position.	83
5.10	Mean velocity profile	83
5.11	Turbulent intensity profiles.	85
5.12	Shear stress profiles.	86
5.13	Budget of turbulent kinetic energy	87
5.14	Velocity structural functions	88
5.15	Velocity spectra in the spanwise direction.	89
5.16	Velocity spectra in the streamwise directions	90
5.17	Mean temperature profile	91
5.18	Streamwise turbulent heat flux and intensity of heat transfer profile.	92
5.19	Budget of turbulent heat transfer	93
5.20	Third-order temperature structure functions	94
5.21	Temperature spectra	95
5.22	Wave height and pressure field at the interface during the transient	97
5.23	Wave height and pressure field at the interface after the stationarity	98
5.24	Two points correlations of wall-normal and streamwise velocity fluctuations	99
5.25	Wave height spectra computed along the streamwise and spanwise directions	100
6.1	Initial velocity conditions	104
6.2	Wave height and pressure field at the interface during the transient	106

Chapter 1

General introduction

1.1 Air-water interaction

Near the interface of the atmosphere and the oceans, many interesting processes take place. Air-sea interaction involves those processes that influence the transport of momentum, heat, moisture, water evaporation and precipitation.

Since the oceans cover more than 70 % of the Earth's surface it is worthwhile to study the physical phenomena associated to air-sea interaction. Such studies have several applications. The growing interest for the climate change issue have brought to the necessity of more accurate and reliable climate models, where a correct representation of exchanges between atmospheres and ocean is crucial. Other applications where a deep knowledge of the air-sea interfacial phenomena plays an important role, are the water and waves forecasts. For weather prediction models, the boundary conditions above waters need to be specified while in wave models an accurate description of the energy input due to the wind is needed. Finally, there are many commercial interests, for example: offshore wind energy production, ship routing, design of offshore platforms and support of defensive operations.

In this work two basic air-sea interaction aspects are investigated using numerical simulation:

- *Wind-waves momentum exchange*, directly affected by the wind-waves interaction since the wind experiences resistance due to waves, while waves grow due to the wind action;
- *Wind-waves heat exchange*, related to different temperatures and thermal diffusivity of the two fluids.

The current thesis came into being as an extension and a further development of the satisfactory results achieved by Lorenzo Silvestri in *Numerical study of wind-wave interfacial phenomena* [1]. Silvestri's work takes into account only the

wind-waves momentum exchange, paying attention on the wave formation and growth mechanism. In the following subsection a brief review of the theory behind these concepts will be presented.

1.2 Wind waves

1.2.1 Wave classification

Waves affect a large number of marine activities and biochemical processes that take place on and below the ocean surface. Generally speaking, waves are oscillations of water surface that can be observed in any water basin, lakes, seas, and oceans.

Waves are primarily generated by:

- *gravitational forces* exerted by the Moon and Sun. This attraction creates tides that are characterized by having a long period (12-24 hours), a length scale comparable with the characteristic length of the basin and a velocity scale varying between 1 and 100 m/s;
- *wind*. Waves generated by wind are directly related to interfacial phenomena at sea interface. As a matter of fact air -water interaction affects turbulent regimes in the atmospheric surface layer and in the ocean's upper layer, resulting on momentum, energy, heat and moisture exchanges. Period, length and time scale of these waves are strictly dependent on the wind characteristics;
- *energy exchanges*. The heat flux, evaporation and precipitation due to the local temperature gradient might generate additional currents;
- *other secondary phenomena* such as oscillations of the Earth during earthquakes, volcanic activities, local meteorological phenomena and storms.

Since the present work focuses on the phenomena occurring at the air-sea interface highlighting the wind-wave interaction, only such wave generated by the blowing wind effort over the sea surface will be evaluated, the so called wind waves. Wind waves or surface wave can be classified in several ways. The most intuitive and commonly used classification is based on the wave period or on the associated wavelength. In Figure 1.1, a summary of the different types of wind waves with respect to wave period is presented. The associated originating forcing and restoring mechanisms are also reported. A graphical representation is provided in Figure 1.2, where an idealized wave energy spectrum shows the full range of ocean wave components.

Classification	Period band	Generating forces	Restoring forces
Capillary waves	<0.1 s	Wind	Surface tension
Ultragravity waves	0.1–1 s	Wind	Surface tension and gravity
Gravity waves	1–20 s	Wind	Gravity
Infragravity waves	20 s to 5 min	Wind and atmospheric pressure gradients	Gravity
Long-period waves	5 min to 12 h	Atmospheric pressure gradients and earthquake	Gravity
Ordinary tidal waves	12–24 h	Gravitational attraction	Gravity and Coriolis force
Transtidal waves	>24 h	Storms and gravitational attraction	Gravity and Coriolis force

Figure 1.1: Ocean wave classification

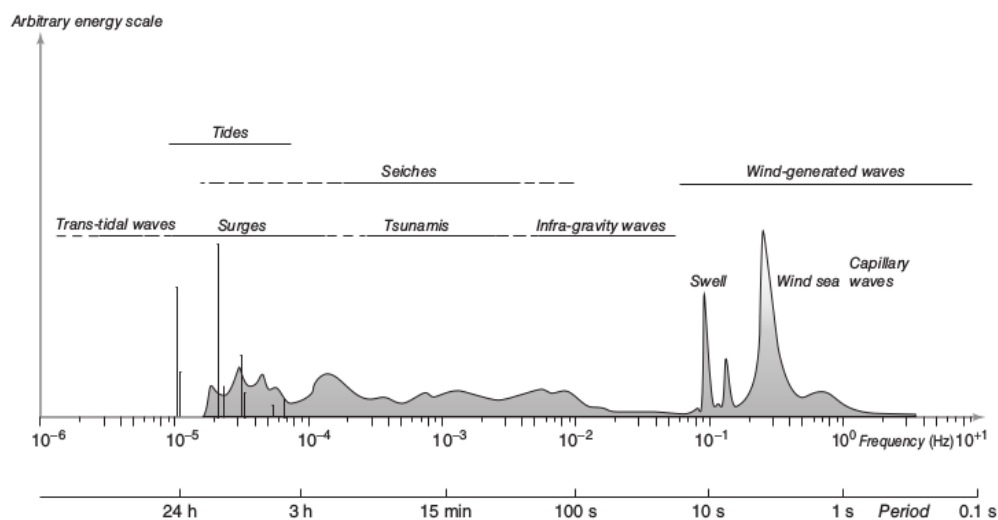


Figure 1.2: Frequency and period of ocean waves

In the wind wave generation the Capillary waves, commonly called Ripples, represent the very first step. Under the direct effect of the local wind, a large number of components with different wave periods, directions of propagation and phases are generated. The resulting wave field is an interaction of all these components, which generates an irregular pattern normally known as wind sea (first state of Gravity waves). When waves propagate over a depth that is much larger than the wavelength, i.e. when the water depth can be considered infinite, longer waves travel faster than shorter ones, dispersing from one another. As a consequence, long waves rapidly move outside the generating area and become known as swells (second state of Gravity waves).

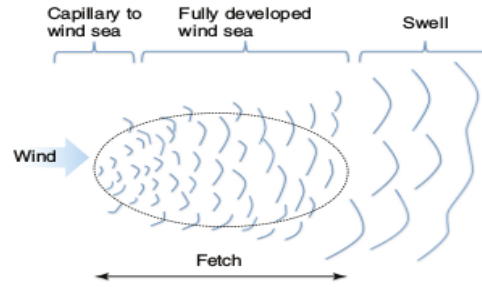


Figure 1.3: Wind wave formation process

1.2.2 Wind wave generation and growth

The most famous theory about water wave formation is the Miles-Phillips theory, i.e. the combination of two wave formation mechanisms described by two different scientists.

Phillips' theory

According to Phillips' theory [2], the formation and development of waves are due to the fluctuations of pressure, caused by the turbulent nature of wind. The different length scales and wave numbers of the eddies impinging on the water cause a random stresses distribution over the surface, that does not respond uniformly. In fact due to resonance mechanism, it will be more excited in the regions where the hitting eddies have a wave number close to the natural frequency of the sea surface. Therefore in that locations waves start growing by means of their increasing amplitude. The main results coming from this theory, is the linear relation between the early growth of the surface height and time:

$$\overline{\eta^2} = \frac{\overline{p^2}t}{2\sqrt{2\rho_w^2 U_c g}} \quad (1.1)$$

where $\overline{\eta^2}$ is the variance of square surface height, $\overline{p^2}$ the mean square turbulence pressure on the water wave surface, t the time, U_c the convection speed of the surface pressure fluctuations and ρ_w the water density.

Miles' theory

The Miles' theory [3], instead of Phillips, is based on the coupling between air flow and wave motion. The wave growth, according to Miles, depends on the instability of the wave motion that is related to the instability of wind at h_c , the critical height where the wind speed is equal to the wave speed. The instability of wind shear profile occurs when there is an inflectional point in the wind mean velocity $U(y)$. So if $\frac{\partial^2 U}{\partial y^2}|_{y=h_c} < 0$ the wave motion will be unstable and an increment of the wave

amplitude will arise. According to Miles, the growth rate of the waves shows an exponentially dependency on time and not linearly as described by Phillips:

$$\eta' = ae^{i(\omega t - kx)} \quad (1.2)$$

where η' is the surface height, ω is the angular frequency of the wave, k is the wave number and a is a constant.

An illustration of the Phillips-Miles mechanism is shown in Figure 1.4. The Phillips' one is the resonance phenomenon due to pressure fluctuations, while the Miles' one is due to shear instability of the wind profile.

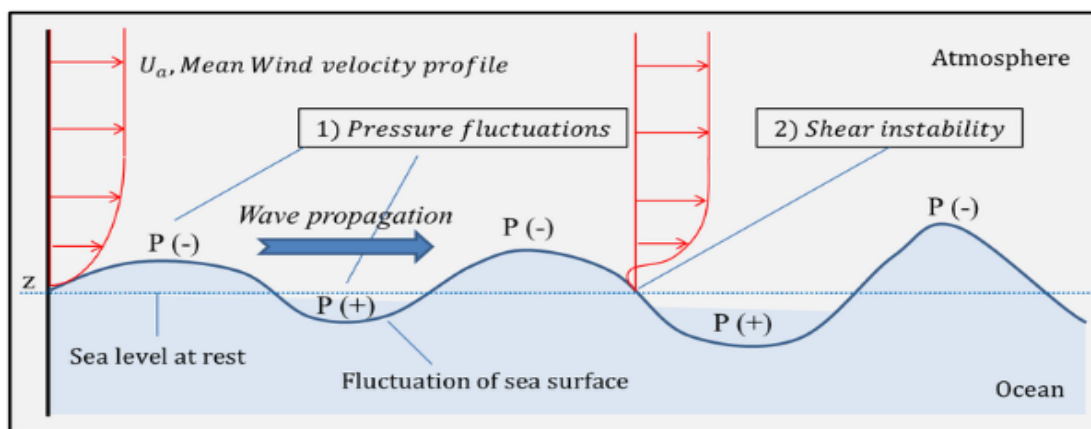


Figure 1.4: Representation of Miles-Phillips theory

Chapter 2

State of the art

2.1 Atmosphere-ocean wave modeling system for evaluating air-sea interaction

As the fact that wind plays a very important role in wave formation and growth has already been pointed out in Chapter 1, now one may ask what about the effect of waves on the marine atmospheric boundary layer (MABL)? This is a very crucial aspect because the presence of high frequency gravity waves along the sea surface, increases the sea roughness that influences momentum, temperature and moisture transfer between atmosphere and ocean. As a matter of fact the state of the wave field is related to the turbulent generation on the MABL and affects the mean wind profile and turbulence variances (*Sullivan et al.* [4]); moreover it acts as roughness elements, influencing the turbulent flow and the vertical wind speed profile, inducing oscillatory motions in the airflow (*Jenkins et al.* [5]).

Even if the strong coupling between wind and waves has been recognized, the current knowledge on the complex mechanisms of atmosphere-ocean interactions is still insufficient. For this reason it is essential to develop appropriate multi-model, multi-scale advanced prediction systems that simulate the atmospheric, wave and oceanic processes in a coupled way.

During the years a lot of coupling modeling systems have been proposed. Among the most recent and noteworthy there are:

- the modeling system made by *Jenkins et al.* [5], that involves Weather Research Forecasting (WRF) model and the Wave model (WAM) coupled by MCEL (Model Coupling Environment Library) coupler. It was built in order to study the impact of waves on the MABL over the North Sea and Norwegian Sea area;

- the two-way coupled atmosphere-ocean wave system (WEW), made by *Katsafados et al.* [6]. Built in order to investigate air-sea interaction under extreme weather conditions, WEW consists of the Workstation Eta as the atmospheric component and the WAM model as the ocean wave component;
- the two-way coupled atmosphere-ocean wave system called CHAOS (Chemical Hydrological Atmospheric Ocean wave System) and made by *Varlas et al.* [7]. This system consists of the Weather Research Forecasting (WRF) model with Chemistry (WRF-Chem) and Hydrology (WRF-Hydro) as the atmospheric component and the Wave model (WAM) as the ocean wave component. WRF and WAM models are coupled using the OASIS Model Coupling Toolkit (OASIS3-MCT) that enables models to communicate and exchange the information required to refine their simulation results. A scheme of the system is represented in Fig.2.1

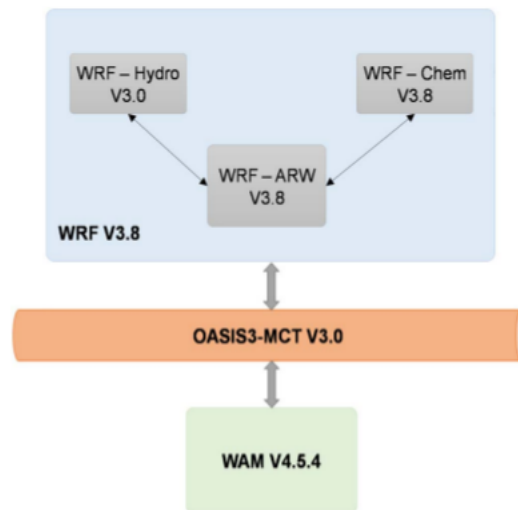


Figure 2.1: CHAOS scheme

In order to explain how the atmospheric and ocean models work and how the coupling between them occurs, CHAOS system will be taken as reference for all the following subsections.

2.1.1 Surface layer Parametrization

The surface layer scheme in CHAOS and in the other modeling systems is based on the Revised Monin-Obukhov similarity theory (*Jiménez et al.* [8]) where the

surface fluxes are parameterized as follows:

$$\tau = \rho_a u_\tau^2 = \rho_a C_d (U_a - U_w)^2 = \rho_a C_d U_a^2 \quad (2.1)$$

$$H = -\rho_a c_p u_\tau \theta_* = \rho_a c_p C_h U_a (\theta_w - \theta_a) \quad (2.2)$$

$$LH = L_v \rho_a u_\tau q_* = L_v \rho_a C_q U_a (q_w - q_a) \quad (2.3)$$

$$E = H + LH = \rho_a U_a [c_p C_h (\theta_w - \theta_a) + L_v C_q (q_w - q_a)] \quad (2.4)$$

where τ , H , LH and E are the fluxes of momentum, sensible heat, latent heat and enthalpy, respectively; ρ_a is the air density of the surface layer, u_τ is the friction velocity, U_a is the wind speed at the lower level (at the height of 28 m) and U_w is the sea surface current velocity, that can be considered null ($U_w = 0$) in a coordinate system moving with the sea surface current. Additionally, θ_* and q_* are the temperature and moisture scales, respectively; c_p is the specific heat capacity at constant pressure; L_v is the latent heat of vaporization; θ_a and θ_w are the air (at the lower level with height 28 m) and sea surface potential temperature, respectively; q_w is the interfacial value of the water vapor mixing ratio; q_a is the specific humidity of air at the lower level (at the height of 28 m) and C_d , C_h and C_q are the dimensionless bulk transfer coefficients for momentum, sensible heat and moisture.

The Monin–Obukhov similarity theory is used to calculate the transfer coefficients. The dimensionless wind shear and potential temperature gradient are usually expressed as (Araya [9])

$$\frac{\kappa y}{u_\tau} \frac{\partial u_a}{\partial y} = \Phi_m \left(\frac{y}{L} \right) \quad \frac{\kappa y}{\theta_*} \frac{\partial \theta}{\partial y} = \Phi_h \left(\frac{y}{L} \right),$$

where $\kappa = 0.4$ is the von Kármán constant, u_a is the wind speed at level y , and

$$L = -\frac{u_\tau^3}{\kappa \frac{g}{\theta_a} \rho_a c_p} = \frac{u_\tau^2}{\kappa g \frac{\theta_*}{\theta_a}}$$

is the Obukhov length (Obukhov [10]), that indicates the contribution of shear and boyant production to turbulent kinetic energy. Integrating the equations for wind speed gradient and potential temperature gradient with respect to y , leads to:

$$u_a = \frac{u_\tau}{\kappa} \left[\ln \frac{y}{y_0} - \psi_m \frac{y}{L} + \psi_m \frac{y_0}{L} \right] \quad (2.5)$$

$$\theta_a - \theta_w = \frac{\theta_*}{\kappa} \left[\ln \frac{y}{y_0} - \psi_h \frac{y}{L} + \psi_h \frac{y_0}{L} \right] \quad (2.6)$$

where y_0 is the roughness length while $\psi_{m,h}$ are the integrated similarity functions for momentum and heat that are defined as follows (Panofsky [11]):

$$\psi_{m,h}\left(\frac{y}{L}\right) \equiv \int_0^{y/L} [1 - \phi_{m,h}(\zeta)] \frac{d\zeta}{\zeta}.$$

Combining Eq.(2.1) and Eq.(2.5) and neglecting the contribution of $\psi_m(y_0/L)$ allows one to obtain the bulk transfer coefficient for momentum:

$$C_d = \frac{\kappa^2}{[\ln(\frac{y}{y_0}) - \psi_m(\frac{y}{L})]^2} \quad (2.7)$$

Instead, combining Eq.(2.2) with Eqs.(2.5) and (2.6) and neglecting the contribution of $\psi_h(y_0/L)$ allows one to obtain the bulk transfer coefficient for heat:

$$C_h = \frac{\kappa^2}{[\ln(\frac{y}{y_0}) - \psi_m(\frac{y}{L})][\ln(\frac{y}{y_0}) - \psi_h(\frac{y}{L})]} \quad (2.8)$$

A similar derivation to the one used to obtain the transfer coefficients for momentum and heat is used to compute the value of the bulk transfer coefficient for moisture (*Carlson and Boland* [12]; *Grell et al.* [13]):

$$C_q = \frac{\kappa^2}{[\ln(\frac{y}{y_0}) - \psi_m(\frac{y}{L})][\ln(\frac{\rho c_p \kappa u \tau y}{c_s} + \frac{y}{y_0}) - \psi_h(\frac{y}{L})]} \quad (2.9)$$

where c_s is the effective heat transfer coefficient for nonturbulent processes. These bulk transfer coefficients are associated with the stability of surface layer and the roughness length. In general, the integrated similarity functions for momentum and heat are calculated using empirical approaches for different stability conditions and slight modifications for the transfer coefficients are applied:

$$C_d = \frac{\kappa^2}{[\ln(\frac{y+y_0}{y_0}) - \psi_m(\frac{y+y_0}{L}) + \psi_m(\frac{y_0}{L})]^2} \quad (2.10)$$

$$C_h = \frac{\kappa^2}{[\ln(\frac{y+y_0}{y_0}) - \psi_m(\frac{y+y_0}{L}) + \psi_m(\frac{y_0}{L})][\ln(\frac{y+y_0t}{y_0t}) - \psi_h(\frac{y+y_0}{L}) + \psi_h(\frac{y_0}{L})]} \quad (2.11)$$

$$C_q = \frac{\kappa^2}{[\ln(\frac{y+y_0}{y_0}) - \psi_m(\frac{y+y_0}{L}) + \psi_m(\frac{y_0}{L})][\ln(\frac{y+y_0q}{y_0q}) - \psi_h(\frac{y}{L}) + \psi_h(\frac{y_0}{L})]} \quad (2.12)$$

y_{0t} and y_{0q} are the thermal and the humidity transfer roughness lengths.

2.1.2 Wave model (WAM)

The ocean wave component in CHAOS is the Wave model (WAM). In WAM waves, described by the wave spectrum $F(k; x, t)$, are governed by the energy balance

equation (*Komen et al.* [14])

$$\frac{\partial F}{\partial t} = S = S_{in} + S_{nl} + S_{ds} \quad (2.13)$$

where the source functions S represent the physics of wind input, dissipation by wave breaking and nonlinear wave interactions. Since this work is focused on the wind-wave interaction only the source term regarding the wind input will be considered. The input source term S_{in} is related to the roughness length y_0 that can be derived from the following empirical formula (*Smith* [15]):

$$y_0 = y_c + y_v = \frac{au_\tau^2}{g} + \frac{0.11v_a}{u_\tau} \quad (2.14)$$

where y_c is the roughness length component due to the wind stress, also called wave-induced roughness length, while y_v is the component due to the air viscosity that represents the roughness length in case of a smooth surface (without waves). Additionally, a is the dimensionless Charnock parameter, g is the gravity acceleration and v_a is the dynamical viscosity of air. In CHAOS, the Charnock parameter a is calculated by WAM following the quasi-linear theory of *Janssen* ([16], [17]) as:

$$a = \frac{\hat{a}}{\sqrt{1 - \frac{\tau_w}{\tau}}} \quad (2.15)$$

where $\hat{a} = 0.01$. The wave-induced stress τ_w and the total stress τ are then calculated as follows (*Bidlot* [18]):

$$\tau_w = \frac{\rho_w}{\rho_a} g \int S_{in} k d\omega d\varphi \quad (2.16)$$

$$\tau = \frac{u_\tau^2}{\rho_a} \quad (2.17)$$

where ω is the angular frequency, ρ_w is the water density, φ is the propagation direction and k is the wave number. Once S_{in} is determined by combining equations (2.15), (2.16) and (2.17), it can be substituted in the energy balance equation (2.13) to determine the two-dimensional wave spectrum. However in order to solve the equation (2.17) the friction velocity u_τ , computed by WRF, is needed.

2.1.3 Weather Research Forecasting (WRF)

The atmospheric component in CHAOS is the Weather Research Forecasting (WRF) model with Chemistry (WRF-Chem) and Hydrology (WRF-Hydro). The wind field at 10 m is estimated by WRF using the following expression (*Jiménez et al.* [8]):

$$u_{10m} = u_a \frac{\ln\left(\frac{10+y_0}{y_0}\right) - \psi_m\left(\frac{10+y_0}{L}\right) + \psi_m\left(\frac{y_0}{L}\right)}{\ln\left(\frac{y+y_0}{y_0}\right) - \psi_m\left(\frac{y+y_0}{L}\right) + \psi_m\left(\frac{y_0}{L}\right)} \quad (2.18)$$

Considering that the relation between $u(y)$ and u_τ is given by the logarithmic profile, the next relation can be derive:

$$u(10m) = \frac{u_\tau}{\kappa} \ln\left(\frac{10}{y_0}\right) \quad (2.19)$$

Now combining together equations (2.14), (2.18) and (2.19) the wind field at $10m$ u_{10m} , the friction velocity u_τ and the roughness length y_0 can be determined. Finally, the momentum, heat and moisture fluxes are computed by means of (2.10), (2.11) and (2.12) using y_0 , previously calculated.

2.1.4 Two-way coupling between WAM and WRF

The coupling of WRF and WAM models in CHAOS is achieved using OASIS3-MCT (Ocean Atmosphere Sea Ice Soil - Model Coupling Toolkit). WRF and WAM models utilize different domain projection, integration time step, grid geometry and cell size. Therefore, in order to enable the two models to operate in two-way coupling mode, major effort has been undertaken in order to homogenize, synchronize and handle the data exchange between the atmospheric and the ocean wave components of the system through the coupler.

A multi-level flowchart of the parallel execution of the system and the data exchanges between WRF and WAM through OASIS3-MCT are depicted in Fig.2.2. In this example, a typical configuration of WRF and WAM is assumed with time step ratio 1/10 and 3 exchanged fields, the horizontal wind components (u and v) at 10 m calculated by WRF and the Charnock parameter calculated by WAM. The time of exchange information between the models is set to the source time step of WAM. Each model utilizes the relevant OASIS3-MCT routines to send and receive data. WRF and WAM separately initialize the required Charnock parameter and the wind components, respectively, using background fields. The background fields can be produced using previous simulation results or other source of data (e.g. analysis data, custom values). At the beginning of simulation, these fields are appropriately interpolated from the WAM to the WRF grid and vice versa. At the next time steps, the models regularly exchange the winds at 10 m above sea surface (WRF to WAM) and the Charnock parameter (WAM to WRF) by applying the OASIS3-MCT transformations between the two grid structures. The regridding procedure is based on local bilinear approximations using auxiliary regridding files. To save computational time, these files are built at the beginning of simulation and are only rebuilt in the case where the grids of the models have been modified.

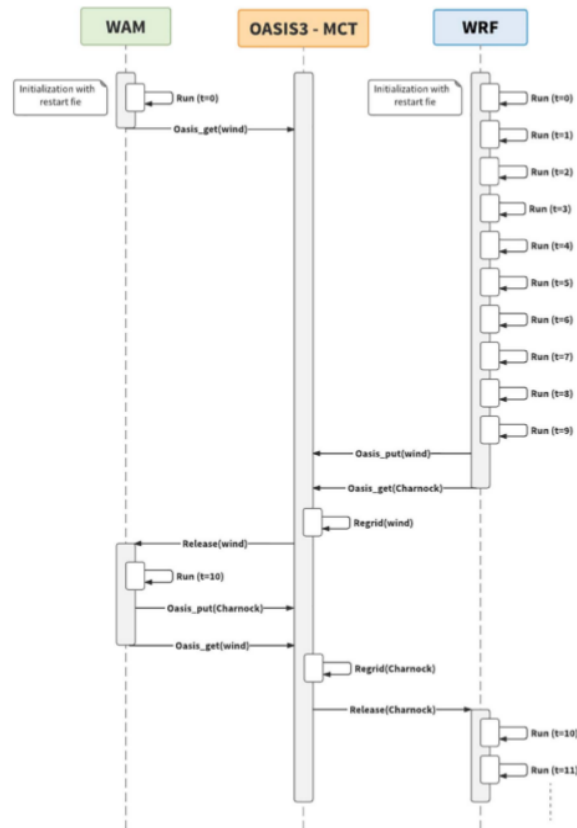


Figure 2.2: Communication between WRF and WAM is depicted in the multi-level flowchart.

2.2 Turbulent boundary layer theory

Disregarding the wave-induced stress, the wind blowing over the sea surface can be compared with air flow over a flat plate. In the light of this analogy, turbulent wall-bounded shear flow is analyzed in the present section.

Generally turbulence generates mixing and tends to smear out gradients, but in case of wall-bounded flows the presence of no-slip condition at solid wall completely changes the characteristic of the flow. In comparison of a laminar boundary layer one may say that the fluctuations in a turbulent boundary layer tends to decrease the gradients over the main part of the boundary layer, but in a thin region near the wall the viscous forces become important and force the velocity to adhere to the wall itself. In this thin region the gradient is much larger than for a corresponding situation in a laminar boundary layer (see Figure 2.3), thereby causing an high wall-shear stress, and hence, a much higher drag than for a laminar

boundary layer.

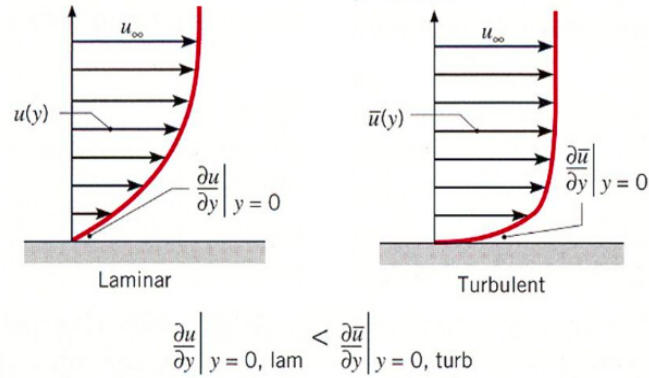


Figure 2.3: Comparison between laminar and turbulent mean velocity profiles.

This points to a central features of the wall-bounded flow, namely the distinction of two different layers (inner and outer regions) characterized by two different length scales. In order to deeply understand and analyze a turbulent flow near a solid boundary, a non-dimensional analysis is performed and the following limited set of flow properties is identified:

- ν – kinematic viscosity;
- ρ – density;
- U – mean velocity profile;
- τ_w – shear stress at the wall;
- $u_\tau = \sqrt{\frac{\tau_w}{\rho}}$ – friction velocity;
- $l_v = \frac{\nu}{u_\tau}$ – the inner (viscous) lengthscale, that is the appropriate scaling parameter for the near-wall inner region;
- δ – the outer lengthscale, that is the appropriate scaling parameter for the outer region. It represents the boundary layer thickness in a boundary layer flow, the pipe radius and the channel half-width in a pipe and in a channel flow, respectively.

The inner region

The dimensional parameters used to describe the inner region are 5 ($\nu, \rho, U, u_\tau, l_v$) while the physical dimensions involved are 3 (mass, length, time). By applying the

Buckingham theorem, two non-dimensional parameters expressing the normalized wall-distance and velocity, are derived:

$$y^+ \equiv \frac{y}{l_v} = \frac{yu_\tau}{\nu} \quad (2.20)$$

$$U^+ \equiv \frac{U}{u_\tau} \quad (2.21)$$

Now assuming the mean flow in the near-wall region not to be influenced by the outer length scale, the so called *law of the wall* can be formulated:

$$U^+ = f_1(y^+) \quad (2.22)$$

The outer region

The dimensional parameters used to describe the outer region are 5 ($\nu, \rho, U, u_\tau, \delta$) while the physical dimensions involved are 3 (mass, length, time). By applying the Buckingham theorem, two non-dimensional parameters expressing the normalized wall-distance and velocity, are derived:

$$\bar{y} \equiv \frac{y}{\delta} \quad (2.23)$$

$$\bar{U} \equiv \frac{U_\infty - U}{u_\tau} \quad (2.24)$$

Therefore considering the deviation from the free-stream velocity U_∞ , it is possible to write down the so called *velocity defect law*:

$$\bar{U} = f_2(\bar{y}) \quad (2.25)$$

The overlap or logarithmic region

For large enough Reynolds number an overlap region can be identified. In that region both y^+ -values ($y^+ \gg 1$) and small \bar{y} -values ($\bar{y} \ll 1$) are present. This means that both descriptions (2.22) and (2.25) hold simultaneously. Matching of the relative derivatives of the mean velocity profiles, they should be in independent of length scale, and hence, constant:

$$\frac{y}{u_\tau} \frac{\partial U}{\partial y} = y^+ \frac{df_1}{dy^+} = -\bar{y} \frac{df_2}{d\bar{y}} = \text{const.} \quad (2.26)$$

Integrating (2.26) a logarithmic mean velocity profiles in the overlap region is obtained

$$f_1(y^+) = \frac{1}{\kappa} \ln y^+ + B \implies U^+ = \frac{u_\tau}{\kappa} \ln y^+ + B \quad (2.27)$$

$$f_2(\bar{y}) = \frac{1}{\kappa} \ln \bar{y} + C \implies U_\infty - U = \frac{u_\tau}{\kappa} \ln \bar{y} + C \quad (2.28)$$

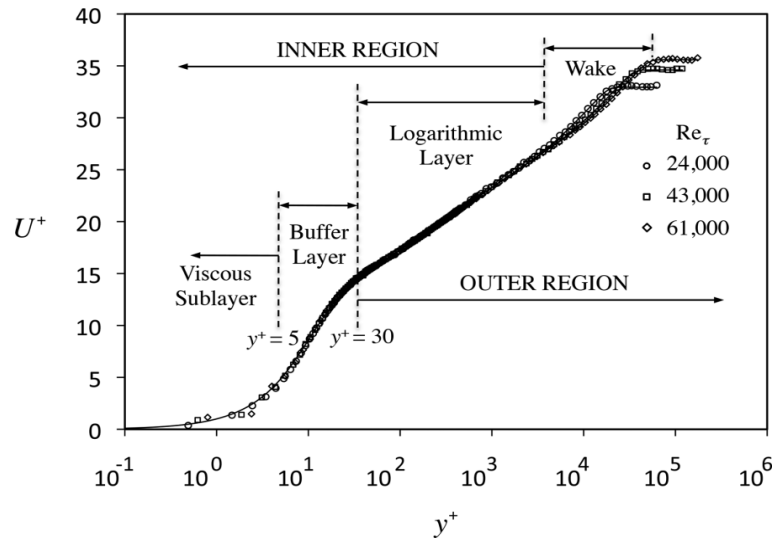


Figure 2.4: Inner scaling of a turbulent mean velocity profiles.

In Figure 2.4 some mean velocity profiles at different Reynolds numbers, plotted in semi-log coordinates with an inner scaling, are shown. As can be seen, an additional partition of the inner and outer layers is usually defined:

- the *Wake region* is the outer part of the boundary layer. It is characterized by large scales eddies, that resides in a region of low shear and as such have very long life-times. It is exactly for this reason that disturbances introduced into the outer part of the boundary layer take a very long time to die out;
- the *Logarithmic region* is characterized by eddies with length scales proportional to y^+ . These eddies possess energies higher than those found in the weak region and are the results of the interaction between the outer and near wall flow. The start of the logarithmic layer is not very distinct, and can be said to start in the interval $50 < y^+ < 200$;
- the *Buffer region* is very similar to the logarithmic region with the exception that the turbulent structures become very anisotropic and even more energetic. It is also the region from which most of the turbulent production mechanism originates. The maximum of turbulent production, i.e. where viscous and turbulent stress are equal in magnitude, is usually identified at $y^+ \approx 12$;
- the *Viscous sublayer* is the region in the immediate vicinity of the wall and is characterized by a linear variation $U^+ = y^+$. Its name is due to the fact that in this portion the turbulent stress are negligible with respect to the viscous stress. The viscous sublayer extends out to approximately $y^+ = 5$;

2.3 Heat transfer as a passive scalar

The transport of heat in turbulent flows is of great importance in many engineering applications. For small temperature differences, the turbulent velocity field drives the temperature field and the influence of the latter on the former is rather weak and can be neglected. In these cases, a passive scalar field can be determined independently by solving the conservation equation of the passive scalar for a given turbulent velocity field:

$$\frac{\partial T}{\partial t} + u_j \frac{\partial T}{\partial x_j} = \lambda \frac{\partial^2 T}{\partial x_j \partial x_j} \quad (2.29)$$

where T is the temperature field, u_j are the velocity components in three directions and λ is the molecular diffusivity of heat that can be computed starting from the Prandtl number Pr as $\lambda = \nu/Pr$.

The friction velocity u_τ , the inner length scale l_* and outer length scale δ are the basic normalization parameters for turbulent flow problems. Analogously, the normalization parameter used for the heat transfer problem has to be defined. It is called friction temperature and it is computed as:

$$\theta_\tau = \frac{\lambda \frac{\partial T}{\partial y}|_w}{u_\tau} \quad (2.30)$$

Fully developed thermal statistics in turbulent flow typically use inner and outer normalizations analogous to those used to describe the mean streamwise velocity profile. Defining Θ as the mean temperature profiles, the inner and outer scaling of temperature can be expressed by the following relations:

$$\text{Inner region: } \Theta^+ - \Theta_{wall}^+ = f_{\theta 1}(y^+) \quad (2.31)$$

$$\text{Outer region: } \frac{\Theta - \Theta_\infty}{\theta_\tau} = f_{\theta 2}(\bar{y}) \quad (2.32)$$

where $\Theta^+ = \Theta/\theta_\tau$ is the inner scaling mean temperature profile, Θ_{wall}^+ is the inner scaling wall temperature and Θ_∞ is the free stream temperature in a boundary layer flow or the center line temperature in a channel flow (Θ_{CL}). In the overlap region both descriptions (2.31) and (2.32) hold simultaneously. Matching of the relative derivatives of the mean temperature profiles, they should be independent of length scale, and hence, constant:

$$\frac{y}{\theta_\tau} \frac{\partial \Theta}{\partial y} = y^+ \frac{df_{\theta 1}}{dy^+} = \bar{y} \frac{df_{\theta 2}}{d\bar{y}} = const. \quad (= 1/\kappa_\theta) \quad (2.33)$$

which implies that

$$\frac{df_{\theta 1}}{dy^+} = \frac{1}{\kappa_{\theta} y^+} \quad (2.34)$$

Integrating (2.34), a logarithmic mean temperature profiles in the overlap region is obtained:

$$\Theta^+ - \Theta_{\infty}^+ = \frac{1}{\kappa_{\theta}} \ln y^+ + B_{\theta} \quad (2.35)$$

The common way to characterize the mean temperature profile is to following the analogy between heat and momentum transfer . Thus the thermal boundary layer

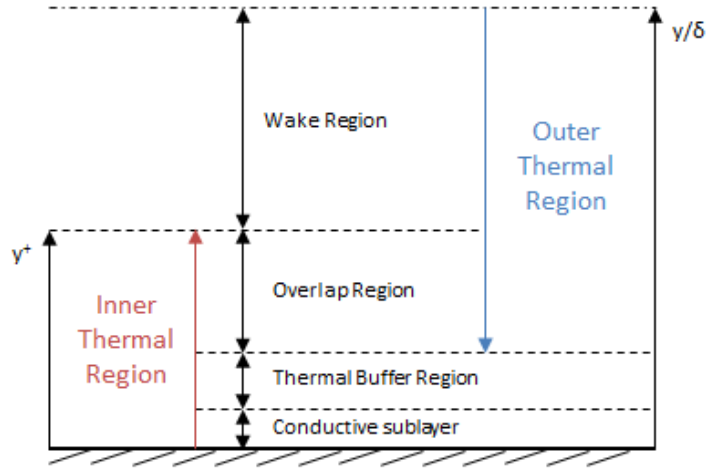


Figure 2.5: The thermal boundary layer regions

for wall bounded turbulent flow can be divided into the classical four layer structure within two separate scaling regions that are the Inner and the Outer Thermal regions (see Figure 2.5). The inner thermal region, localized close to the heated solid wall, is composed of a molecular or conductive sublayer and a thermal buffer layer, whereas an outer region commonly known as core thermal region extends to the centerline of the pipe or channel. The classical logarithmic layer and the outer or wake layer constitute the Outer thermal region.

Chapter 3

Governing equations and numerical tools

In this chapter all the governing equations and the numerical tools used in the current thesis will be analyzed. The chapter will be divided in two sections representing the two different flows dealt in the work:

- The single phase flow, studied in Chapter 4;
- The two phase flow, analyzed in Chapter 5 and 6.

For both of them, first the relative governing equations and the mathematics of the models describing the flow behavior will be addressed, and subsequently the OpenFOAM[®] solvers involved for the simulations will be introduced.

3.1 Single Phase flow

Classical studies of fluid dynamics concentrates on the flow of a single homogeneous phase, e.g., water, air. Their behavior can easily be described through the Navier-Stokes equations, that were formulated around the 1830.

3.1.1 Governing equations

In the present thesis, the main assumptions behind the governing equations describing the single phase flow behavior are the following:

1. the fluid, at the scale of interest, is a continuum. In other words it can be described without taking in to account the motion of the single molecule but considering the macroscopic properties (as density, pressure and velocity) of an infinitesimal volume elements called fluid particle;

2. the fluid is Newtonian. It means that the viscous stresses arising from the flow, at every point, are linearly proportional to the local strain rate. More precisely, a fluid is Newtonian only if the tensors that describe the viscous stress and the strain rate are related by a constant viscosity tensor that does not depend on the stress state and velocity of the flow. Adding the hypothesis of isotropic flow, the viscosity tensor reduces to two real coefficients, describing the resistance of the fluid to continuous shear deformation and continuous compression or expansion.
3. the Stokes' hypothesis is valid: the isotropic part of the stress tensor is completely determined by the thermodynamic pressure and its deviatoric part coincides with the viscous stress tensor. In other words, it means that isotropic dilatation of an elementary volume of fluid do not produce viscous stress.
4. no discontinuities , i.e. abrupt changes of the flow quantities, have to be present inside the flow volume. If this hypothesis is fulfilled, the localization lemma can be applied and the same equations are used to describe the flow state at each point and in each condition, even at rest.
5. the flow is incompressible. It means that the variations of density occurring in the fluid due to its motion may be neglected.
6. the temperature can be considered as a passive scalar. The word passive refers to the condition that temperature only cause density differences that are small enough to result in negligible influence on the flow.

By considering the previous assumptions, the governing equations for an incompressible Newtonian flow with heat transfer are given by the continuity equation, that together with the momentum equation forms the NS-equations, and by the passive scalar equation :

$$\nabla \cdot \vec{u} = 0 \quad (3.1)$$

$$\frac{\partial \vec{u}}{\partial t} + \nabla(\vec{u}\vec{u}) = -\frac{1}{\rho}\nabla p + \nabla(v\nabla\vec{u}) \quad (3.2)$$

$$\frac{\partial T}{\partial t} + \nabla(\vec{u}T) = \nabla(\lambda\nabla T) \quad (3.3)$$

where the velocity vector \vec{u} , the pressure and temperature field, respectively p and T , are the unknowns of the above system.

3.1.2 PimpleFoam Solver

The solution of the system, introduced in the previous section, is not straightforward because an explicit equation for the pressure is not available. One of the most common approaches, in order to solve the pressure-momentum coupling problem, is to derive an equation for the pressure by taking the divergence of the momentum equation (Eq.3.2) and by substituting it in the continuity equation (Eq.3.1). In order to solve the pressure-momentum coupling problem, three main algorithms have been developed in OpenFOAM®:

- SIMPLE algorithm. The Semi-Implicit-Method-Of-Pressure-Linked-Equations algorithm is used to solve steady-state problems, therefore the time derivation is neglected. Due to the inconsistency of the algorithm, the equations have to be under-relaxed to achieve the stability.
- PISO algorithm. The Pressure-Implicit-Split-Operator, algorithm is used to solve transient problems, therefore the time derivation is needed. In order to ensure the stability of the equations, the Courant number (deeply analyzed in Chapter 4) is held less than one.
- PIMPLE algorithm. The Merged PISO–SIMPLE algorithm combines both the previous algorithms, allowing bigger time-steps than PISO one. The problem is transient but the SIMPLE (steady-state) treatment is used to find the steady-state solution for each time step. This allows the Courant number to be larger than one without numerical instability.

In the current thesis the pressure momentum coupling for the single phase flow has been solved by using the PIMPLE algorithm, implemented in the *pimpleFoam* solver. As all the OpenFOAM® solvers, *pimpleFoam* is written in C++ language and by looking at the main file *pimpleFoam.C*, it is possible to understand how it works. In the following the most relevant and significant part of this file is reported.

```
73
74 // --- Pressure-velocity PIMPLE corrector loop
75 while (pimple.loop())
76 {
77 #include "UEqn.H"
78 // --- Pressure corrector loop
79 while (pimple.correct())
80 {
81 #include "pEqn.H"
82 }
```

```

83  if (pimple.turbCorr())
84  {
85  laminarTransport.correct();
86  turbulence->correct();
87  }
88  }
89

```

pimpleFoam.C

As it can be seen the solver is based on two different loops: an inner loop called "Pressure corrector loop" and an outer one named "Pressure-velocity PIMPLE corrector loop". In the Pressure corrector loop, first the momentum equation is solved by using the pressure values computed at the previous time step, then the velocity field coming from the momentum equation is introduced in the pressure equation to get the actual pressure field:

1. $\frac{\partial \vec{u}}{\partial t} + \nabla(\vec{u}\vec{u}) = -\frac{1}{\rho}\nabla p_{old} + \nabla(v\nabla\vec{u}) \longrightarrow \vec{u}_{uncorrected}$
2. $\nabla^2 p = f(\vec{u}_{uncorrected}, \nabla p) \longrightarrow p_{new}$

The new pressure field coming from the Pressure corrector loop is then used in the Pressure-velocity PIMPLE corrector loop where the corrected velocity field is computed:

3. $\frac{\partial \vec{u}}{\partial t} + \nabla(\vec{u}\vec{u}) = -\frac{1}{\rho}\nabla p_{new} + \nabla(v\nabla\vec{u}) \longrightarrow \vec{u}_{corrected}$

For all the simulations discussed in the next Chapters, the *pimpleFoam* solver has been set to perform the pressure-velocity PIMPLE corrector loop once time. This means that the SIMPLE mode has never been activated and the solver has just operated in PISO mode, fulfilling only the stability criterion based on the Courant number.

3.1.3 Modified PimpleFoam Solver

The *pimpleFoam* solver as implemented in OpenFOAM[®] does not solve the passive scalar equation for heat transfer (Eq.3.3) therefore some changes needed to be done. With this in mind a new solver called *my_pimpleFoam* has been created. Once both the pimple loops are ended and the final pressure and velocity fields are calculated, *my_pimpleFoam* solver computes the equation for the temperature field called TEqn. This can be clearly seen looking at the solver main file reported in the following.

```
73
74 // --- Pressure-velocity PIMPLE corrector loop
75 while (pimple.loop())
76 {
77 #include "UEqn.H"
78 // --- Pressure corrector loop
79 while (pimple.correct())
80 {
81 #include "pEqn.H"
82 }
83 if (pimple.turbCorr())
84 {
85 laminarTransport.correct();
86 turbulence->correct();
87 }
88 }
89 #include "TEqn.H"
90
```

my_pimpleFoam.C

In order to be computed by the solver, the TEqn might be first written and defined in a .H file shown below.

```
1
2 fvScalarMatrix TEqn
3 (
4 fvm::ddt(T)
5 + fvm::div(phi,T)
6 - fvm::laplacian(DT,T)
7 );
8 TEqn.relax();
9 TEqn.solve();
10
```

TEqn.H

3.2 Two-Phase flow

Two-phase flows occur in a wide variety of natural phenomena and technical processes such as bubbles rising in a carbonated drink, raindrops falling through the

air, gasoline and air reacting in an automotive engine, water and steam circulating through a nuclear reactor. Common to all two-phase flows is the existence of discernible interfaces that separate one phase from the other. Whether the flow involves two immiscible liquids or a liquid and a vapor, the interfacial topology constantly changes as the phase interact exchanging energy, momentum and mass. These interactions and changes in interfacial topology are the most difficult aspect of two phase flow to model and imply accurate analysis on the validity of the governing equations introduced in section 3.1.1. for a two-phase flow. The two-phase flow analyzed in this thesis is made by air and water, two fluids that can be considered incompressible and characterized by different densities:

$$\rho = \begin{cases} \rho_a = 1 & \text{kg/m}^3 \\ \rho_w = 1000 & \text{kg/m}^3 \end{cases}$$

Since velocity is a continuous function through the interface in the whole domain, the continuity equation (Eq.3.1) for each phase is still valid. Special reference needs to be made for momentum equation (Eq.3.2): nevertheless the continuity of velocity, the abrupt change of density causes the discontinuity of momentum (ρu) at the interface. As a consequence, the momentum equation, which is valid for a continuous and differentiable momentum function over the whole flow domain, can not be used anymore. In order to overcome this problem and writing the momentum equation in a suitable way for the two-phase flow, a proper method to take into account the discontinuities at the interface, has to be introduced.

3.2.1 The Volume of Fluid method

Among all the existing method for the computation of two-phase flows, the one selected for this thesis is the Volume of Fluid method commonly known as VOF. Introduced by Hirt and Nichols in 1981 [21], the VOF method uses an indicator scalar function α to express the fraction of cell volume occupied by a certain fluid. In the specific case of air-water flow, the indicator scalar function has been considered with respect to the water component and for this reason it was defined as follows:

$$\alpha = \frac{V_{water}}{V_{cell}} \quad \alpha = \begin{cases} 1 & \text{if the cell is inside water} \\ 0 & \text{if the cell is inside air} \\ 0 < \alpha < 1 & \text{if the cell contains the interface} \end{cases} \quad (3.4)$$

In this method the tracking of the surface is attained by solving the continuity equation of the volume fraction which consists in the classical transport equation used for describing a substance transported by a bulk motion:

$$\frac{\partial \alpha}{\partial t} + \nabla(\vec{u}\alpha) = 0 \quad (3.5)$$

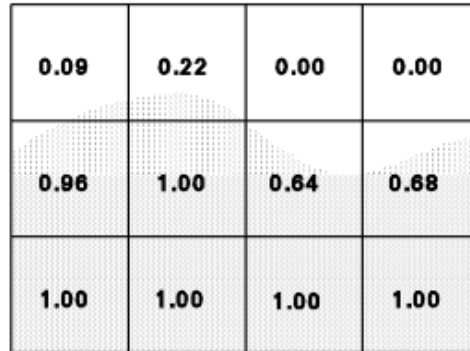


Figure 3.1: Example of indicator Scalar function distribution through the domain

The VOF method has been introduced to overcome the problem of momentum discontinuity due to the dual nature of the two-phase flow, therefore the definition of the volume fraction as a step function given in Eq.3.4 can not be used. In order to represent α , a twice differentiable function smoothly varying from 0 to 1 in a transition region of finite thickness δ , placed between the two fluids, has been defined as follows:

$$\alpha = \begin{cases} 1 & \text{if the cell is inside water} \\ 0 & \text{if the cell is inside air} \\ 0 < \alpha_\delta < 1 & \text{if the cell is inside the transition region } \delta \end{cases} \quad (3.6)$$

The definition of this continuous function allows to determine a single momentum equation for the two phase flow system, where each fluid property should be calculated as a weight function considering the volume occupied by the fluid in the cells. In Eq 3.7 the new continuous functions for density and viscosity are given:

$$\begin{cases} \rho = \rho_w \alpha + \rho_a (1 - \alpha) \\ \mu = \mu_w \alpha + \mu_a (1 - \alpha) \end{cases} \quad (3.7)$$

3.2.2 VOF problems with Conventional Discretizations

The success of the VOF method depends heavily on the scheme used for advecting the α field. When conventional discretization scheme as central, downwind and upwind differencing are used to discretized the advection equation of α (Eq 3.5) two main problems can occur:

- **The boundedness of α :** when the equation is discretized following the conventional scheme some no-physical values of the volume fraction can

arise. It means that the volume fraction conservation is not held during the transport between the cells and some fluid mass are generated from nowhere.

- **Smearing of sharp interface:** the discretization with classical schemes introduces a numerical diffusion term that modifies the the sharp configuration of the interface smearing it over several cells.

The first problem is solved by introducing a controlled downwinding inside the donor-acceptor scheme. The donor-acceptor scheme was originally introduced by Ramshaw and Trapp in 1976 [22], and extended in the work of Hirt. A synthetic representation of the scheme is presented in Figure 3.2.a. The donor cell (D) is in

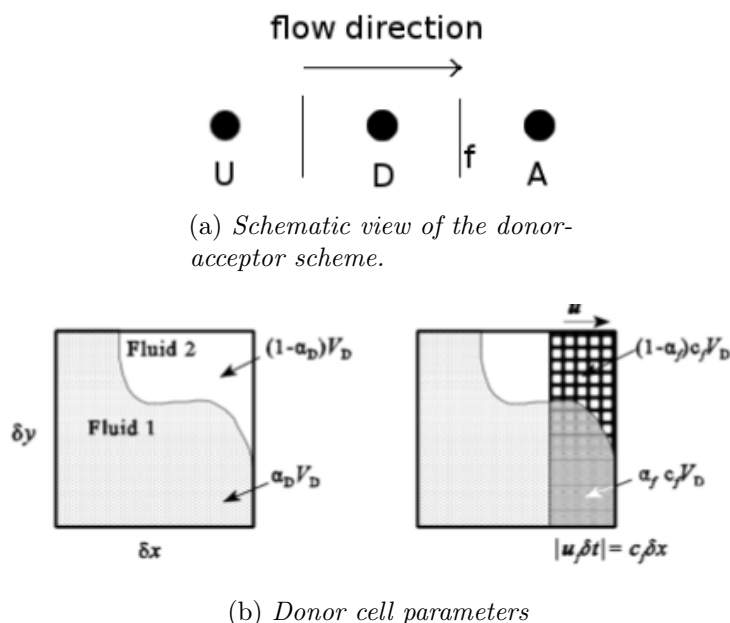


Figure 3.2: Donor-acceptor scheme

the centre and has two neighbours, namely the acceptor cell (A) and the upwind cell (U). The acceptor cell receives fluid from the donor cell and its locations is determined by the flow direction. Thus, in this case it is on the right side of the donor cell, separated by face f . By considering a donor cell of total volume V_D with a phase fraction equal to α_D , it is possible define the amount of water and air presented in the donor cell:

$$\begin{cases} V_{wD} = \alpha_D V_D \\ V_{aD} = (1 - \alpha_D) V_D \end{cases} \quad (3.8)$$

Similarly the same quantities can be defined for the acceptor cell:

$$\begin{cases} V_{wA} = \alpha_A V_A \\ V_{aA} = (1 - \alpha_A) V_A \end{cases} \quad (3.9)$$

Choosing an appropriate differentiation scheme means finding a correct way to define the volume fraction α_f , which is the volume fraction transported from the donor cell to the acceptor one in the time interval δt . The classical downwinding scheme uses only the acceptor cell volume fraction imposing $\alpha_f = \alpha_A$ and ignoring if the acceptor cell requests more fluid than what is actually present in the donor one. This may give rise to non-physical volume fractions where α is not bounded between zero and one. To avoid such a condition, controlled downwinding scheme is introduced. It is based on the accomplishment of two criteria:

1. **Boundedness:** the α value has to be bounded between zero and one i.e the fluid mass can not be created and destroyed but can only be transported inside the flow domain.
2. **Availability:** the amount of a fluid convected over a face during a time step has to be less than or equal to the amount available in the donor cell.

Mathematically the above criteria can be expressed by considering the Courant number trough the face f. If the Courant number on face f is $C_f = u\delta t/\delta x$ and α_f is the volume fraction of the fluid convected over the face in one time step, then $\alpha_f C_f V_D$ is the amount of water convected through the cell face during a time step and $(1 - \alpha_f) C_f V_D$ is the corresponding amount air. Now the availability criterion states that the amount of water convected over a face cannot be greater than the amount available in the donor cell:

$$\alpha_f C_f V_D \leq \alpha_D V_D \quad \longrightarrow \quad \alpha_f \leq \frac{\alpha_D}{C_f} \quad (3.10)$$

And similarly for air:

$$(1 - \alpha_f) C_f V_D \leq (1 - \alpha_D) V_D \quad \longrightarrow \quad \alpha_f \leq \frac{\alpha_D}{C_f} - \frac{1 - C_f}{C_f} \quad (3.11)$$

By combining the above inequalities, one attains:

$$\frac{\alpha_D}{C_f} - \frac{1 - C_f}{C_f} \leq \alpha_f \leq \frac{\alpha_D}{C_f} \quad (3.12)$$

By applying the requirement $\alpha_f = \alpha_A$ to the above equation, the final form for donor-acceptor face value approximation can be written as:

$$\alpha_f = \min \left\{ \max \left(\frac{\alpha_D}{C_f} - \frac{1 - C_f}{C_f}, \alpha_A \right), \frac{\alpha_D}{C_f} \right\} = \min \left\{ \alpha_A + \max \left((1 - \alpha_A) - \frac{1 - \alpha_D}{C_f}, 0 \right), \frac{\alpha_D}{C_f} \right\}. \quad (3.13)$$

The above equation is the basis of the controlled downwinding scheme. By means of it both boundedness and availability criteria are ensured. In Figure 3.3 a clear example of the controlled downwinding improvements with respect to the normal downwinding, are shown. In case a) the donor cell contains the interface, while the

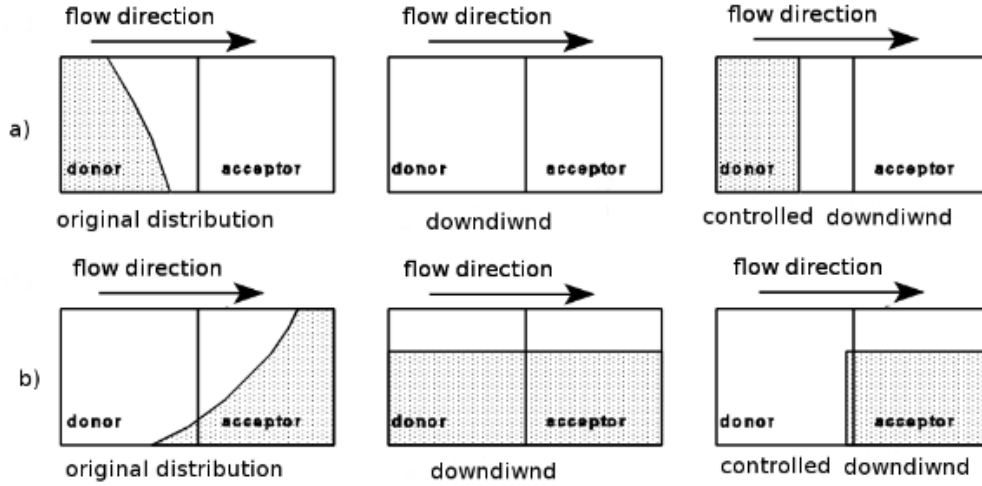


Figure 3.3: Controlled downwinding improvements.

acceptor cell is completely filled with a single fluid. By downwinding, the donor cell has to donate the same fluid as presently contained by the acceptor cell. Thus, the presence of the interface in the donor cell is ignored. However, the donor cell contains both fluids and cannot donate more of one fluid than available inside it. With controlled downwinding, the donor cell will first donate all the available fluid required by the acceptor cell and then start to donate the other fluid. The situation is similar in case b), where the interface is distributed over both cells. Through downwinding, the acceptor cell demands the same fluid proportion as currently contained by it. By controlled downwinding, the donor cell will first comply with this demand, but will start to donate of the other fluid once it has run out of the first one.

The application of a controlled downwinding scheme dose not solve the second problem given by the non-realistic deformation of the interface. The advection

equation of the volume fraction (Eq 3.5) dose not contain any diffusion term, therefore α should be transported through the flow domain without changing the interface shape, but when a downwinding discretization scheme is introduced the advection equation becomes:

$$\frac{\partial \alpha_j}{\partial t} + u \frac{\alpha_{j+1} - \alpha_j}{\Delta x_i} = 0 \quad (3.14)$$

By Taylor expanding α_{j+1} , the following equation is obtained:

$$\frac{\partial \alpha}{\partial t} + u \frac{\partial \alpha}{\partial x_i} + \underbrace{u \frac{\Delta x_i}{2} \frac{\partial^2 \alpha}{\partial x^2}}_{\text{Truncation Error}} + u O(\Delta x_i^2) = 0 \quad (3.15)$$

The truncation error introduced by the downwind scheme becomes a numerical diffusion term in the transport equation and therefore the sharp shape of α is not maintained over the time, but it diffuses over the other cells. In order to avoid the interface diffusion effect a compressive term is added to the advection equation:

$$\frac{\partial \alpha}{\partial t} + \nabla(\bar{u}\alpha) + \underbrace{\nabla(\vec{u}_r \alpha(1 - \alpha))}_{\text{Compressive Term}} = 0 \quad (3.16)$$

where

$$\begin{cases} \bar{u} = \alpha \vec{u}_w - (1 - \alpha) \vec{u}_a & \text{is the wighted averaged velociy} \\ \vec{u}_r = \vec{u}_w - \vec{u}_a & \text{is the compression velocity} \end{cases} \quad (3.17)$$

Following this model the evolution of the free surface is related to the air and water relative velocity \vec{u}_r and it is proportional to their phase fractions. Clearly, the compressive term becomes active only close to the interface, precisely in the transitional region where $0 < \alpha < 1$.

3.2.3 Governing equation of a two-phase flow

Once the VOF method has been introduced and explained, all the governing equations describing the two phase flow can be collected together:

- **Continuity equation for each phase**

$$\nabla \cdot \vec{u} = 0 \quad (3.18)$$

- **Phase fraction definition**

$$\alpha = \frac{V_{water}}{V_{cell}} \quad \alpha = \begin{cases} 1 & \text{if the cell is inside water} \\ 0 & \text{if the cell is inside air} \\ 0 < \alpha_\delta < 1 & \text{if the cell is inside the transition region } \delta \end{cases} \quad (3.19)$$

- **Advection equation of the phase fraction**

$$\frac{\partial \alpha}{\partial t} + \nabla(\bar{u}\alpha) + \nabla(\vec{u}_r\alpha(1-\alpha)) = 0 \quad \text{with} \quad \begin{cases} \bar{u} = \alpha\vec{u}_w - (1-\alpha)\vec{u}_a \\ \vec{u}_r = \vec{u}_w - \vec{u}_a \end{cases} \quad (3.20)$$

- **New continuous functions for density and viscosity**

$$\begin{cases} \rho = \rho_w\alpha + \rho_a(1-\alpha) \\ \mu = \mu_w\alpha + \mu_a(1-\alpha) \end{cases} \quad (3.21)$$

- **Momentum equation**

Due to density and viscosity definition given in Eq 3.21, the momentum discontinuity problems through the interface are solved and the conservation of momentum can be written as:

$$\frac{\partial(\rho\vec{u})}{\partial t} + \nabla(\rho\vec{u}\vec{u}) = -\nabla p + \nabla(\mu\nabla\vec{u}) + \rho\vec{g} + \vec{f}_\sigma \quad (3.22)$$

where $\rho\vec{g}$ represents the gravity force while \vec{f}_σ is a force term related to the surface tension acting on the air-water interface. In order to completely define the momentum equation, an expression for \vec{f}_σ is needed, hence a deeper analysis on its nature and its characteristics is required. In an air-water interface (see Figure 3.4), surface tension results from the greater attraction of water molecules to each other (due to cohesion) than to the molecules in the air (due to adhesion). The net effect is an inward force at the interface that causes the water to behave as if its surface were covered with a stretched elastic membrane. Against the inward force, work has to be performed to

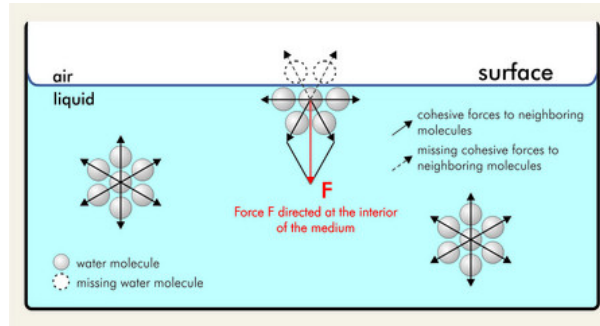


Figure 3.4: Forcing acting on the water molecule

move something through this layer or to expand the interface surface. For this reason the surface tension σ is defined as the amount of work (Nm)

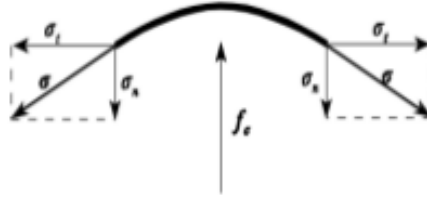


Figure 3.5: Surface tension force

necessary to expand the surface (m^2) of a liquid by one unit. For water and air at room temperature a surface tension coefficient of $\sigma = 0.07N/m$ should be considered. When air and water are in equilibrium, since the tangential components σ_t of the surface tension σ cancel out each others, over the interface there should exist a normal force \vec{f}_σ , called surface tension force, that balances the resultant of the normal components σ_n of the surface tension. If \vec{f}_σ is larger or smaller than the sum of σ_n components, the non zero resultant along the normal direction causes the acceleration of the air-water interface. The amount of \vec{f}_σ depends on the pressure jump through the air-water interface, which is a function of the surface tension σ and the interface curvature κ :

$$\Delta P = \sigma \kappa. \quad (3.23)$$

By considering that the surface tension acts only close the interface, \vec{f}_σ can be write as

$$\vec{f}_\sigma = \int_{S(t)} \sigma \kappa_{fs} \vec{n}_{fs} \delta(\vec{x} - \vec{x}_{fs}) dS \quad (3.24)$$

where κ_{fs} , \vec{n}_{fs} and \vec{x}_{fs} are the mean curvature, the normal and position vector at the interface, respectively. The function $\delta(\vec{x} - \vec{x}_{fs})$ is defined as

$$\delta(\vec{x} - \vec{x}_{fs}) = \begin{cases} 1 & \text{if the point belongs to the interface } (\vec{x} = \vec{x}_{fs}) \\ 0 & \text{if the point dose not belong to the interface } (\vec{x} \neq \vec{x}_{fs}) \end{cases} \quad (3.25)$$

and translates in mathematical terms the limited influence of the surface tension force on the air-water interface.

The model described till now for the surface tension force presents two main problems: the first is the discontinuity through the flow domain introduced by Eq 3.25 and the second is the dependence of the surface tension force on interface shape and position that are unknown variables since the interface is not tracked explicitly by VOF method. This two problems are solved by modeling the surface tension force with the continuous surface force model (CFS). In this model \vec{f}_σ is considered to be a volume force, as gravity, acting

only in the transition region i.e where α smoothly changes from 1 to 0. In Figure 3.6 an example of the pressure (related to \vec{f}_σ) and the α variation through the transition region is reported. In the CSF model a definition for

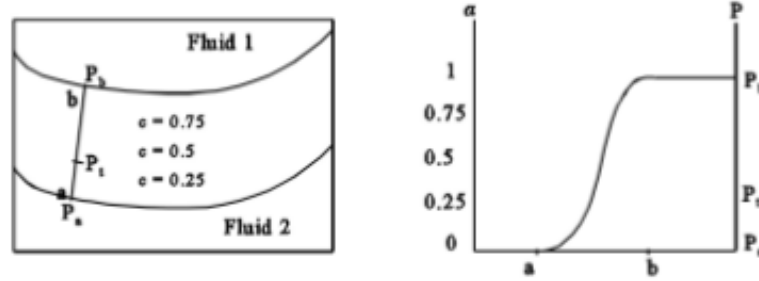


Figure 3.6: Surface tension force

both the unknown variables are given for each layer of the transition region: the position normal vector is defined as the gradient of the indicator function α while the interface curvature is determined with the gradient of the normal vector:

$$\vec{n} = \nabla\alpha \quad (3.26)$$

$$\kappa = -\nabla \cdot \frac{\vec{n}}{|\vec{n}|} \quad (3.27)$$

Since α has been defined in the VOF method as twice differentiable, both \vec{n} and κ are continuous function and the surface tension force can be approximated as:

$$\vec{f}_\sigma = \int_{S(t)} \sigma \kappa_{f_s} \vec{n}_{f_s} \delta(\vec{x} - \vec{x}_{f_s}) dS \approx \sigma \kappa \vec{n} \quad (3.28)$$

- **Heat transport equation**

As for the single phase flow, the temperature is analyzed as a passive scalar. This means that both the phase change and the density differences due to temperature are not considered. The equation describing the heat transfer is hence the same as for single phase flow:

$$\frac{\partial T}{\partial t} + \nabla(\vec{u}T) = \nabla(\lambda \nabla T) \quad (3.29)$$

where the thermal diffusivity is defined as

$$\lambda = \lambda_w \alpha + \lambda_a (1 - \alpha) \quad (3.30)$$

3.2.4 IneterFoam and Modified InterFoam Solvers

The governing equations, introduced in the previous section, are solved by using the OpenFOAM® solver called *interFoam*, which employs the VOF method in order to capture the interface between two incompressible, isothermal, immiscible fluids and the PIMPLE algorithm to solve the pressure-momentum coupling. In the following the most relevant and significant part of the *interFoam.C* file is reported.

```
101
102 // --- Pressure-velocity PIMPLE corrector loop
103 while (pimple.loop())
104 {
105 #include "alphaControls.H"
106 #include "alphaEqnSubCycle.H"
107
108 mixture.correct();
109
110 #include "UEqn.H"
111
112 // --- Pressure corrector loop
113 while (pimple.correct())
114 {
115 #include "pEqn.H"
116 }
117
118 if (pimple.turbCorr())
119 {
120 turbulence->correct();
121 }
122 }
123
```

interFoam.C

As *pimpleFoam*, the *interFoam* is based on two different loops where the momentum (UEqn.H), the pressure (pEqn.H) and advection equation for α (alphaEqnSubCycle.H) are solved. Since *interFoam* has been implemented for two isothermal fluids the Eq.3.29 for heat transfer can not be solved, therefore a new solver called *my_interFoam* has been created. Once both the pimple loops are ended and the final pressure, velocity and indicator function fields are calculated, *my_interFoam* solver computes the equation for the temperature field called TEqn. This can be clearly seen looking at the solver main file reported in the following.

```
101
102 // --- Pressure-velocity PIMPLE corrector loop
103 while (pimple.loop())
104 {
105 #include "alphaControls.H"
106 #include "alphaEqnSubCycle.H"
107
108 mixture.correct();
109
110 #include "UEqn.H"
111
112 // --- Pressure corrector loop
113 while (pimple.correct())
114 {
115 #include "pEqn.H"
116 }
117
118 if (pimple.turbCorr())
119 {
120 turbulence->correct();
121 }
122 }
123 #include "TEqn.H"
```

my_interFoam.C

Chapter 4

Turbulent open channel

In this chapter, the direct numerical simulation (DNS) of a fully developed turbulent open channel with passive heat transfer will be presented. Pre-processing, simulation running and post-processing are performed with the aid of three different softwares:

- **OpenFOAM[®]**, involved for pre-processing and simulation running;
- **ParaView**, used to visualize all the flow topology and variable in the three dimensional view;
- **Matlab**, employed to compute all the statistical quantities describing the flow.

4.1 Simulation details

In this section the numerical details of the simulation will be addressed. The simulation has been successfully performed by means of the modified solver *my_pimpleFoam* described in Chapter 3 while all the simulation setting and parameters are introduced and explained in the following.

4.1.1 Physical system and Mesh properties

The flow geometry and the coordinate system are illustrated in Figure 4.1 in which u, v and w are the streamwise, wall-normal and spanwise components of the fluid velocity, respectively; l_x, l_y and l_z represent the length, height and width of the flow domain; and finally T_{top} and T_{bottom} are the temperature imposed at the top and bottom boundaries, held constant during the simulation.

The numerical conditions are tabulated in Table 4.1, where $R_\tau = u_\tau h/\nu$ is the turbulent Reynolds number based on a friction velocity u_τ and flow depth $h (= l_y)$,

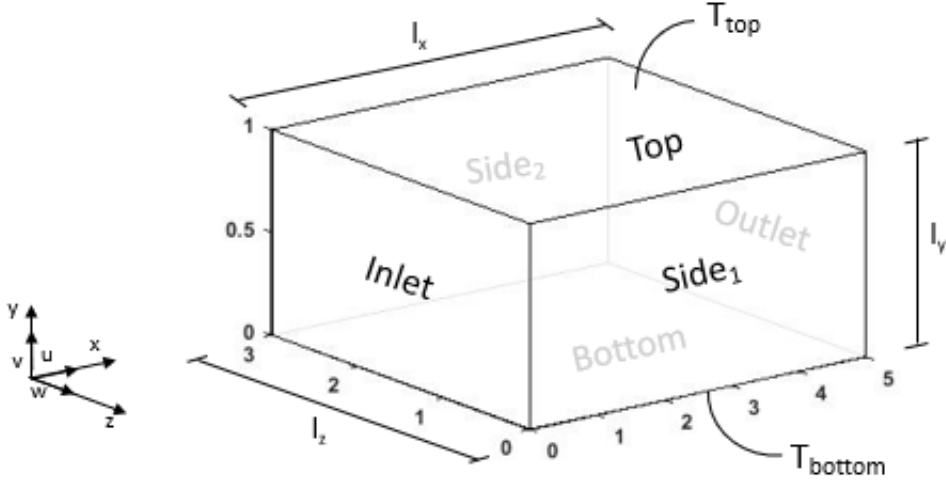


Figure 4.1: Flow geometry

Re_τ	Grid Points			Domain Sizes			Resolution			U_{bar}^+	Nu	Pr
	N_x	N_y	N_z	l_x	l_y	l_z	Δx^+	Δy_{min}^+	Δz^+			
382.5	128	256	128	5 m	1 m	3 m	14.94	0.36	8.96	17.45	8.98	0.7

Table 4.1: Numerical conditions

$U_{bar}^+ = U_{bar}/u_\tau$ is the bulk mean velocity normalized by a friction velocity, $Pr = \nu/\lambda$ is the Prandtl number and $Nu = \frac{h(\partial\Theta/\partial y)|_w}{\Delta T}$ is the Nusselt number, where $\frac{\partial\Theta}{\partial y}|_w$ is the mean temperature gradient at the wall and ΔT is the temperature difference between T_{top} and T_{bottom} . In order to discretized the flow domain, a number of points $(N_x, N_y, N_z) = (128, 256, 128)$ has been used and equally distributed in the wall-parallel directions while an inhomogeneous distribution has been used in the vertical one. To determine the dimensionless parameters for mesh resolution $(\Delta x^+, \Delta y^+, \Delta z^+)$, the dimensional resolution is scaled with the viscous length $l_v = \nu/u_\tau$:

$$\Delta x^+ = \frac{\Delta x}{l_v} = \frac{l_x}{N_x l_v} = 14.94$$

$$\Delta z^+ = \frac{\Delta z}{l_v} = \frac{l_z}{N_z l_v} = 8.96$$

Because of the nonuniform resolution in the y-direction, to obtain the lowest dimensionless resolution, the height of first cell above the wall has to be computed.

Along a length l_y , if N_y cells are requested with a ratio R larger than 1 between the last and first cells, the size of the smallest cell, Δy_{min} , is given by:

$$\Delta y_{min} = l_y \frac{R^{\frac{1}{N_y-1}} - 1}{R^{\frac{N_y}{N_y-1}} - 1}$$

Since in the simulation, a value of $R = 10.702$ has been chosen, Δy_{min} is equal to $0.00095 m$. Now the smallest dimensionless resolution along y-direction can be computed:

$$\Delta y_{min}^+ = \frac{\Delta y_{min}}{l_v} = 0.36.$$

4.1.2 Boundary conditions

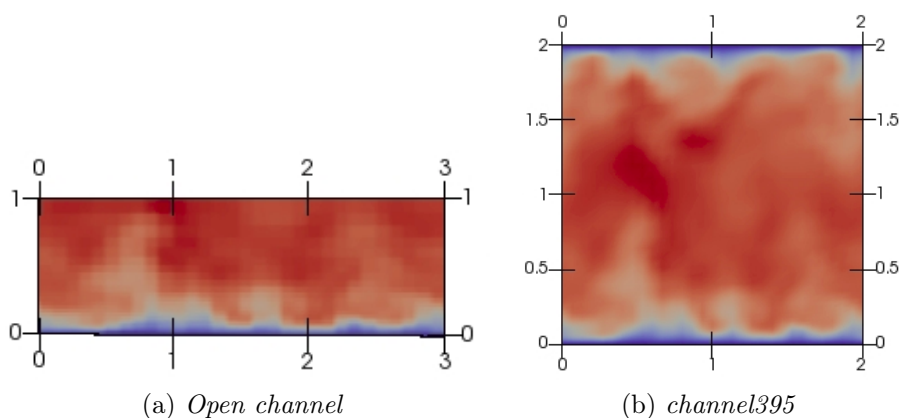
Setting appropriate boundary conditions is vital for a successful simulation. Ill-posed boundary conditions will lead to physically incorrect predictions, and in many cases simulation failure. Therefore, translating the physical system into the numerical one with some boundary conditions applied to, is a very important task. All the boundary conditions set in the current simulation are summarized in Table 4.2. The cyclic boundary condition is a coupling condition between a pair of patches (in this case Inlet-Outlet, Side1-Side2): if a field of a certain flow quantity is present at one patch, it will be reflected at the associated patch exactly as it was. Therefore applying the cyclic boundary condition for all the quantities on the Inlet, Outlet and Sides of the channel is like having the same channel repeated backward and forward, on the left and on the right. This can be seen as an extension of the process studied on a virtual bigger domain. The slip and no slip boundary conditions for the velocity field are applied respectively to the top and bottom of the channel in order to simulate the boundary layer profile of the flow: in this way at the top the velocity vertical gradient will be null as the wall normal velocity fluctuations, while at the bottom the flow will have a zero velocity value. With the purpose of holding the free surface and the wall at a constant temperature the fixed value boundary condition for the top and bottom is chosen. The zero gradient condition is then imposed for the pressure field.

4.1.3 Initial conditions

Initial values for all solved variables need to be set before the solution can begin. In order to reach the fully developed turbulent state in a faster way a disturbed initial condition has to be used. A strong perturbed velocity field is available in the OpenFOAM[®] tutorial *channel395*, which is referred to a channel having $l_x = 4m$, $l_y = 2m$, $l_z = 2m$ and $(N_x, N_y, N_z) = (40, 50, 30)$. The mismatch between the

Variable	Patches			
	Top	Bottom	Sides	Inlet/Outlet
U	Slip	No slip	Cyclic	Cyclic
p	Zero Gradient	Zero Gradient	Cyclic	Cyclic
T	Fixed value at 288K	Fixed value at 303K	Cyclic	Cyclic

Table 4.2: Boundary conditions

Figure 4.2: yz slices of the streamwise velocity

domain size and number of grid elements of the two different channels, has required some additional tricks with respect to the traditional use of the OpenFOAM[®] utility *MapFields*:

1. A temporary channel have been created. It had the same length, width and half height of the *channel395* and the same grid elements of the *Open channel*;
2. By means of *MapFields*, the velocity field relative to half channel of *channel395* has been mapped into the temporary channel;
3. Finally the file of the initial velocity field relative to the temporary channel has been used as initial condition for the *Open channel*, getting a more stretched velocity field as it can be seen in Figure 4.2.

The same procedure is repeated also for initializing the pressure field. As regards the temperature fields a uniform value of 303 K has been applied in the whole domain.

4.1.4 General simulation characteristics

- **The external forcing of the system**

In the current simulation the flow is driven by a pressure gradient, adding a term to the momentum equation introduced in the subsection 3.1.1. Nevertheless the pressure gradient is not directly initialized in the simulation, but it is applied by imposing an average velocity U_{bar} in the channel, where U_{bar} is defined as:

$$U_{bar} = \frac{\int_V \vec{u} dV}{\int_V dV} \quad (4.1)$$

Therefore at every time step the pressure gradient is refreshed and the new value, needed for fulfilling the requirement on U_{bar} , is addressed. The average velocity is initialized in the *fvOptions* file, located in the *constant* folder.

```

16
17     momentumSource
18     {
19         type            meanVelocityForce;
20         active          yes;
21         meanVelocityForceCoeffs
22         {
23             selectionMode    all;
24             fields           (U);
25             Ubar              (0.1335 0 0);
26         }
27     }
28

```

fvOptions file

- **Transport properties**

All the flow transport properties are recapped in the *transportProperties* file, partially reported in the following

```

17
18     Ubar              [0 1 -1 0 0 0 0] (0.1335 0 0);
19     DT                [0 2 -1 0 0 0 0] 2.857e-5;
20     nu                [0 2 -1 0 0 0 0] 2e-05;
21

```

transportProperties

As it can be seen three quantities are requested: U_{bar} , that has already introduced, DT , the thermal diffusivity and ν , the kinematic viscosity, that in this work have been respectively identified as λ and ν . For all the quantities, the physical dimensions have to be specified followed by their numerical value.

- **Turbulent properties**

Since a Direct Numerical Simulation (DNS) has to be performed, all the possible turbulent models available in OpenFOAM[®] have to be deactivated.

```
19
20     simulationType laminar;
21
```

turbulentProperties

This is done by typing the word *laminar* close to *simulationType* in *turbulentProperties*, located in the *constant* folder.

- **Time control**

Since in the current simulation *my_pimpleFoam* solver runs in PISO mode, to achieve temporal accuracy and numerical stability a Courant number less than 1 is required. The Courant number is defined for one cell as:

$$Co = \frac{\delta t |U|}{\delta x} \quad (4.2)$$

where δt is the time step, $|U|$ is the magnitude of the velocity through that cell and δx is the cell size in the direction of the velocity. The flow velocity varies across the domain and a $Co < 1$ must be ensure everywhere. For this reason the time step in the simulation is not fixed but it is continuously adjusted in order to fulfill the required on the maximum Courant number that is set to be 1.

- **Numerical schemes**

In order to ensure the accuracy of the solution, proper discretized schemes have to be selected for each operator present inside the numerical model. All the numerical schemes presented in the current simulation are listed and briefly explained in Table 4.3

4.2 Results

In this section the results coming form the turbulent open channel simulation will be shown and explained.

Operator	Numerical scheme
Time Derivative	Backward. It is a second order implicit time scheme, using previous, actual and next time step data.
Divergence	Gauss linear. The Gauss keyword specifies the standard finite volume discretization of Gaussian integration which requires the interpolation of values from cell centers to face centers. The Gauss entry must be followed by the choice of interpolation scheme. It would be extremely unusual to select anything other than general interpolation schemes and in most cases the linear scheme is an effective choice. The Gauss linear scheme is second order accurate and unbounded from stability.
Gradient	Gauss linear
Laplacian	Gauss linear corrected. For Laplacian schemes the Gauss scheme is the only choice of discretization and requires a selection of both an interpolation scheme for the diffusion coefficient and a surface normal gradient scheme. With the word corrected an explicit non-orthogonal correction is applied for the surface normal gradient scheme.

Table 4.3: Normal schemes

4.2.1 Turbulent structures

As anticipated in Chapter 2, most of the turbulent production occurs in a region close to the wall called, buffer layer. Kinematic studies have deeply investigated this region, highlighting the presence of well defined turbulent structures. One generally refers to these as streamwise velocity streaks and quasi-streamwise vortices. The streamwise velocity streaks are streaky structures of a positive and negative streamwise velocity fluctuations that occur in alternated way while quasi-spanwise vortices are relatively thin eddies elongated in the streamwise direction. These two structure strongly relate to each other: as shown in Figure 4.3 the interaction between a pair of counter-rotating streamwise vortices and the mean shear gives rise to alternated streamwise velocity fluctuations creating interchanging streaks of positive and negative longitudinal velocity fluctuations. Nevertheless the streaks in turn have an high influence on the streamwise eddies. It might be specified, indeed that the latter actually are the tips of another turbulent structure called hairpin vortex, i.e. a vortex loop which spans the boundary layer, arching up from the surface. As it can be seen from the first imagine of Figure 4.4, the unperturbed mean flow is associated with a vorticity field $\vec{\omega} = (0, 0, \omega_z)$, that can be imagined

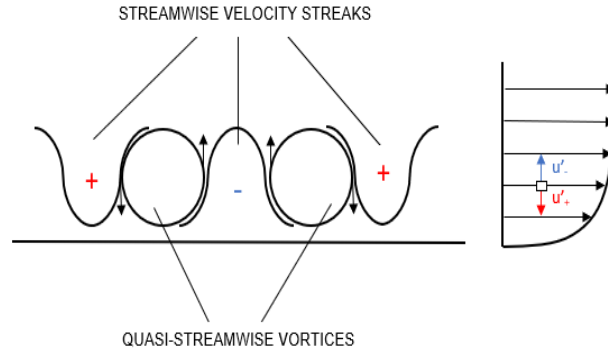


Figure 4.3: Streaks and spanwise vortices interaction mechanism

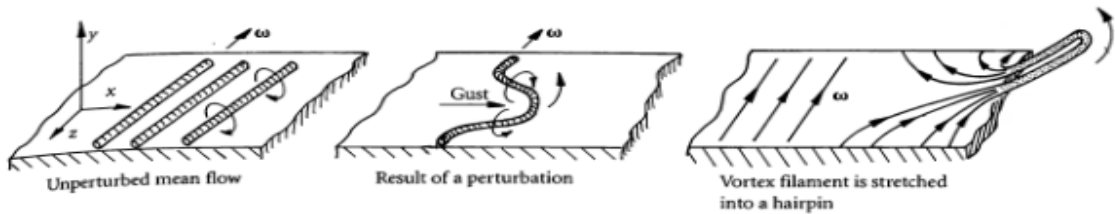
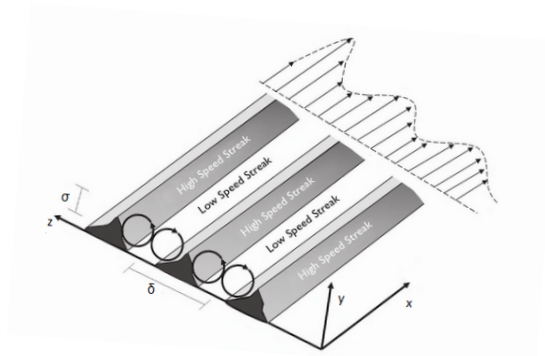


Figure 4.4: Hairpin vortices formation

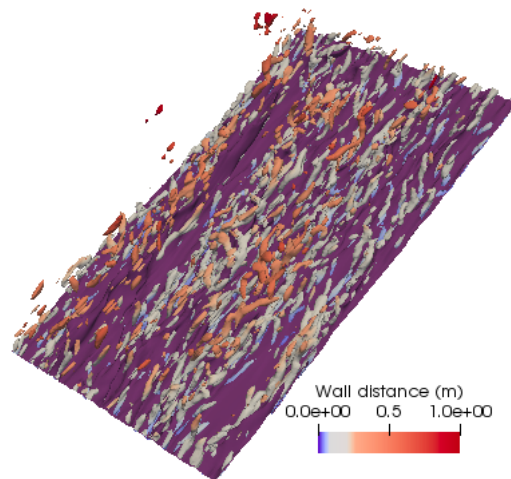
as composed of a multitude of vortex filament or tubes. These structures are then stretched along the streamwise direction by means of the streamwise perturbations introduced by the streaks, giving rise to the hairpin vortices. Due to the streaks rapid oscillations, the elongation of the hairpin vortex goes on until it breaks down into finer-scale motions, known as bursting. What it has been describing till now is nothing more than a self-sustaining cycle of turbulence localized in the near-wall region that can survive without any input from the rest of the flow. This process is known as near-wall autonomous cycle.

In order to visualize these turbulent structures in the simulated open channel two different techniques have been used for the streamwise vortices and the streaks. A large number of vortex-identification methods, vortex definitions, and vortex-core visualization techniques have been proposed in the literature during last three decades, anyway in this thesis the vortex-identification scheme called λ_2 -criterion has been used. The λ_2 parameter is related to the decomposition of the velocity gradient tensor $\frac{\partial u_i}{\partial x_j}$ into a symmetric part S_{ij} , called strain-rate tensor and an antisymmetric part Ω_{ij} , called rotation tensor. A vortex is defined as "a connected

region with two negative eigenvalues of $[S_{ij}^2 + \Omega_{ij}^2]$ [19]. Since $[S_{ij}^2 + \Omega_{ij}^2]$ is symmetric, it has real eigenvalues only, and by ordering the eigenvalues $\lambda_1 \leq \lambda_2 \leq \lambda_3$ the definition becomes equivalent to requiring that $\lambda_2 < 0$. According to this method, streamwise vortices are then visualized by looking at isosurfaces of a certain value for $-\lambda_2$. Since streaks are structures of positive and negative streamwise velocity fluctuations, isosurfaces of streamwise velocity are just required to visualize them. A 3D visualization of streak and vortex structures relative to the open channel is shown in the following (Figure 4.5(b)). It is taken for a $\lambda_2 = -0.05$ and $u = 0.09$ m/s, once the flow has reached its fully developed state.



(a) *Simplified scheme where δ and σ are the streaks spacing and spanwise vortex size, respectively.*



(b) *3D visualization where streaks are colored purple while streamwise vortices by means of the wall distance.*

Figure 4.5: Streaks and spanwise vortices

The presence of turbulent structures involving the near-wall region can be investigated also computing the two point correlation of the streamwise and wall-normal velocity fluctuations, R_{uu} and R_{vv} , in the spanwise direction. The correlations have been calculated as:

$$R_{uu}(y, r_z) = \left\langle \frac{1}{N_x N_z} \sum_{i=1}^{N_x} \sum_{k=1}^{N_z} u'(x_i, y, z_k, t) u'(x_i, y, z_k + r_z, t) \right\rangle \quad (4.3)$$

$$R_{vv}(y, r_z) = \left\langle \frac{1}{N_x N_z} \sum_{i=1}^{N_x} \sum_{k=1}^{N_z} v'(x_i, y, z_k, t) v'(x_i, y, z_k + r_z, t) \right\rangle \quad (4.4)$$

where N_x and N_z are the number of grid elements, respectively along the streamwise and spanwise direction, u' and v' are the velocity fluctuations, r_z is the distance between sampling points while $\langle \rangle$ is the time average.

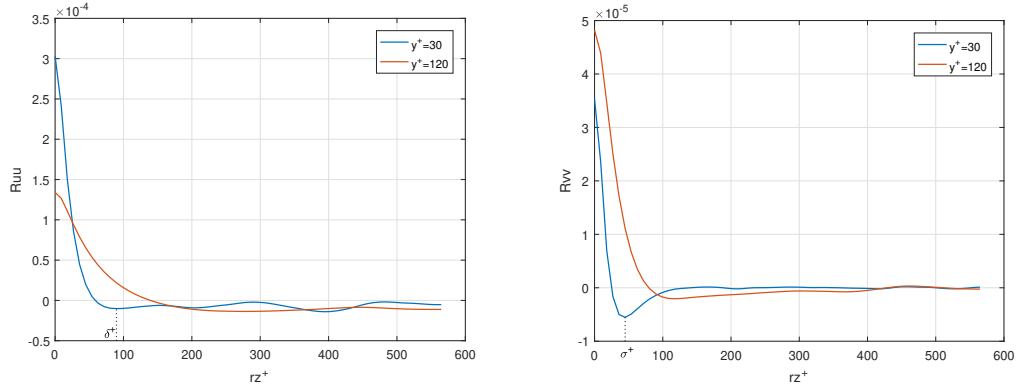


Figure 4.6: Two points correlations of wall-normal and streamwise velocity fluctuations

In Figure 4.6 the plots, showing the correlation trend with respect to the dimensionless distance between sampling points $r_z^+ = r_z/l_v$ at two different heights from the wall, are presented. As it can be seen, a well defined minimum value is reached for both the correlation functions computed at $y^+ = 30$: the minimum relative to the two points correlation of the streamwise velocity fluctuations R_{uu} allows to quantify the dimensionless streaks spacing δ^+ :

$$\delta^+ = \frac{\delta}{l_v} = \frac{r_{zmin}}{l_v} \approx 89.6$$

while the minimum value reached by the two points correlation of the wall-normal velocity fluctuations R_{vv} allows the determinations of the dimensionless spanwise vortex size σ^+ :

$$\sigma^+ = \frac{\sigma}{l_v} = \frac{r_{zmin}}{l_v} \approx 44.8.$$

Obviously the evidence of a minimum value for the correlation functions becomes less and less marked farther from the wall ($y^+ = 120$). This can be explained by the fact that streaks and spanwise vortexes are typically wall turbulent structure and then they are localized in a limited domain region close to the wall.

The phenomenon explained till now can be extended for the thermal boundary layer too. The interaction between the counter-rotating spanwise vortex with the wall temperature gradient causes positive and negative temperature fluctuations, that similarly to the streamwise fluctuations, create the so called thermal streaks. Analogously to the streamwise velocity streaks, the thermal streaks can be visualized with an isosurface of temperature as shown in Figure 4.7. The parallelism between temperature and velocity turbulent structures is then highlighted in Figure 4.8, where yz and xz slices of streamwise velocity and temperature fields are reported.

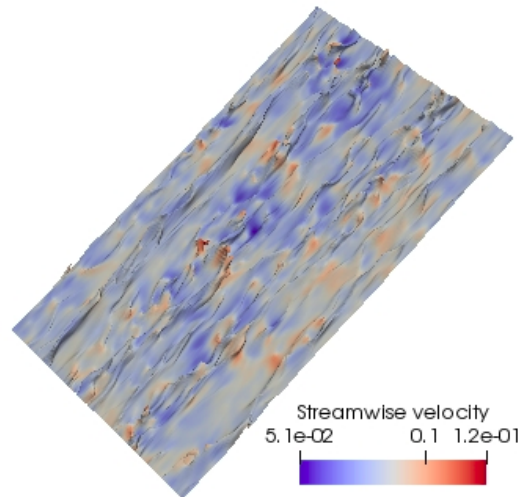
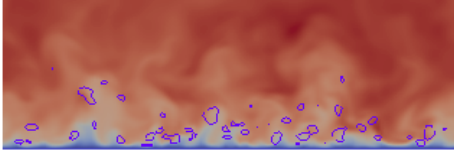


Figure 4.7: 3D visualization of thermal streaks computed for $T = 292K$.

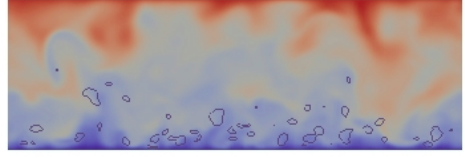
4.2.2 Statistics

The evaluation of all the statistical quantities necessary for analyzing turbulent velocity and turbulent heat transfer may start only once the flow has reached its fully developed state. A flow is said to be fully developed when it is statistically stationary i.e. when all its statistics are steady in time.

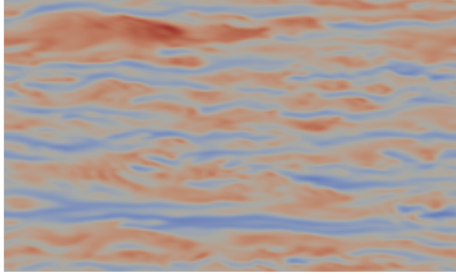
In order to understand at which time the flow reaches its fully developed state, the spatial averages of velocity and temperature field along the homogeneous directions



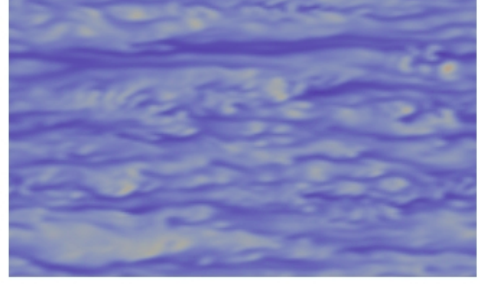
(a) *yz slice at $x = 2.5m$ of streamwise velocity with isolines of $\lambda_2 = -0.05$*



(b) *yz slice at $x = 2.5m$ of temperature with isolines of $\lambda_2 = -0.05$*



(c) *xz slice at $y = 0.05m$ of streamwise velocity*



(d) *xz slice at $y = 0.05m$ of temperature*

Figure 4.8: Slices

have to be computed. Due to the application of cyclic boundary conditions, the flow can be considered homogeneous along the streamwise and spanwise direction, while because of the no slip condition at the bottom, the slip condition at the top, the fixed value condition for temperature both at the top and the bottom and the pressure gradient along the streamwise direction, the mean velocity and temperature profiles exhibit a strong gradient along the wall-normal direction. Therefore the flow can not be considered homogeneous along y-direction. Thanks to the spatial discretization imposed by the grid, the spatial averages of velocity and temperature fields can be computed as follow:

$$\tilde{U}_j(y, t) = \frac{1}{N_x N_z} \sum_{i=1}^{N_x} \sum_{k=1}^{N_z} u_j(x_i, y, z_k) \quad \text{with } j = 1, 2, 3 \quad (4.5)$$

$$\tilde{\Theta}(y, t) = \frac{1}{N_x N_z} \sum_{i=1}^{N_x} \sum_{k=1}^{N_z} T(x_i, y, z_k) \quad (4.6)$$

Once the velocity and temperature field have been spatially averaged, it is possible to evaluate the stationarity of the whole process by looking at the time evolution of two parameters: the friction Reynolds number Re_τ , used to investigate the

achievement of the fully developed turbulent state and the Nusselt number Nu , employed as indicator for the stationarity of the heat transfer. They are computed as:

$$\widetilde{Re}_\tau = \frac{hu_\tau}{\nu} = h \sqrt{\left. \frac{1}{\nu} \frac{\partial \widetilde{U}}{\partial y} \right|_w} \quad (4.7)$$

$$\widetilde{Nu} = \frac{h \left. \frac{\partial \widetilde{\Theta}}{\partial y} \right|_w}{\Delta T} \quad (4.8)$$

where $|_w$ stands for "computed at the wall" and ΔT is the temperature difference between top and bottom $\Delta T = T_{top} - T_{bottom} = 303K - 288K = 15K$. Investigating the time evolution of friction Reynolds number \widetilde{Re}_τ and Nusselt number \widetilde{Nu} , it has been found that both the parameters stabilize around a constant value after 2000s. After this time, that will be the starting point of the statistical analysis, the mean Re_τ is about 382.5 and the mean Nu is about 8.98. Since the stationarity of the flow has been addressed, the concept of time averaging can be introduced. All the statistics that will be presented in this chapter, have been evaluated starting from the time average of the velocity and temperature fields, considering a time window going from $t_0 = 2000s$ to $t_f = 3000s$ with a sample time $t_s = 10s$ and a number of samples $N = 101$. Therefore the time and spatially averaged velocity and temperature field are calculated as follows:

$$U_j(y) = \frac{1}{N} \sum_{n=1}^N \widetilde{U}_j(y, t_n) \quad \text{with } j = 1, 2, 3 \quad (4.9)$$

$$\Theta(y) = \frac{1}{N} \sum_{n=1}^N \widetilde{\Theta}(y, t_n) \quad (4.10)$$

4.2.2.1 Turbulent velocity statistics

Due to its homogeneity along the streamwise and spanwise directions, the velocity statistics of the fully developed open channel flow have no dependence on x and z ($\frac{\partial}{\partial x} \langle \cdot \rangle = 0$ and $\frac{\partial}{\partial z} \langle \cdot \rangle = 0$). This means that the continuity equation is trivially satisfied and by considering

$$U = U(y) \quad V = 0 \quad W = 0 \quad \langle u'v' \rangle = \langle u'v' \rangle(y)$$

the averaged momentum equation, generally called Reynolds equation, can be reduced to:

$$0 = -\frac{1}{\rho} \frac{\partial P}{\partial x} + \frac{\partial}{\partial y} \left(\nu \frac{\partial U}{\partial y} - \langle u'v' \rangle \right) \quad (4.11)$$

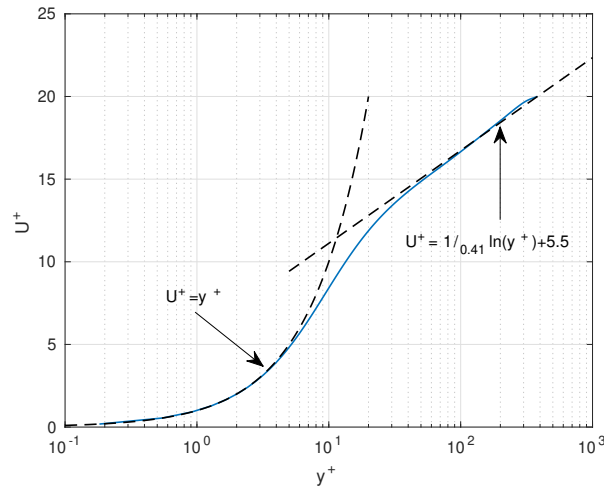


Figure 4.9: Mean velocity profile

where P is the mean pressure while $v \frac{\partial U}{\partial y}$ and $-\langle u'v' \rangle$ are the viscous and Reynolds (introduced by turbulence) shear stress.

As it is already pointed out in Chapter 2, four different layers can be seen by plotting the mean velocity profile of a wall-bounded flow. For the simulated open channel, the viscous sublayer (see Figure 4.9), dominated by universal small turbulent scales, extends up to $y^+ \approx 5$. It is then followed by the buffer layer, roughly localized in the interval $5 < y^+ < 70$, and the logarithmic layer, limited in the region between $y^+ = 70$ and $y^+ = 180$ where the divergence of the mean velocity profile from the logarithmic law states the beginning of the wake region. Looking at the turbulent intensity profiles in Figure 4.10, it is clear as near the free-surface region ($300 < y^+ < 400$) the vertical velocity fluctuations are constrained due to the presence of the impermeability condition but streamwise and spanwise velocity fluctuations are increased. This is due to the fact that close to the top boundary, the turbulent kinetic energy of the wall-normal velocity fluctuations is shared-out between the other two components. Figure 4.11 shows the shear stress profiles and the budget of Reynolds shear stress along the channel height. While the total shear stress $v \frac{\partial U}{\partial y} - \langle u'v' \rangle$ shows always a linear variation, the Reynolds shear stress $-\langle u'v' \rangle$ is almost negligible near the wall. This is in good agreement with the theory: in the immediate wall proximity turbulent effects can be neglect with respect to viscous ones due to the presence of the viscous sublayer.

Obviously a more detailed study of turbulence velocity fluctuations has to be done. In order to understand how they get their energy and what they ultimately

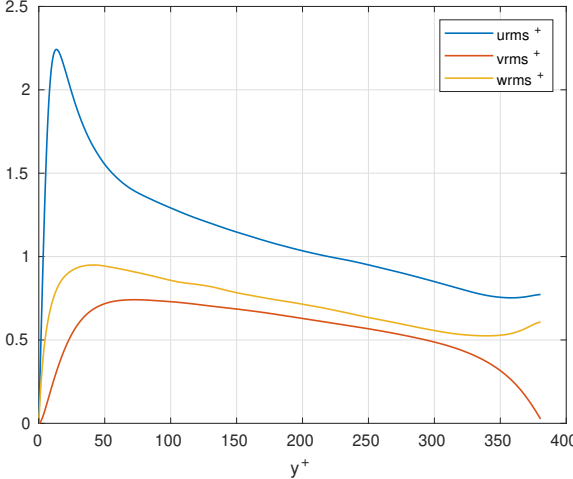


Figure 4.10: Turbulent intensity profiles.

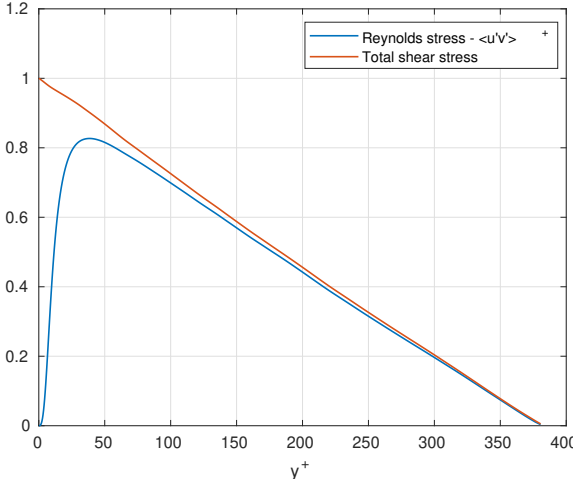


Figure 4.11: Shear stress profiles.

do with it, the balance equation of turbulent kinetic energy has to be introduced:

$$\begin{aligned}
 \frac{\partial \langle k \rangle}{\partial t} = & - \underbrace{\frac{\partial \langle kv' \rangle}{\partial y}}_{\text{Turbulent diffusion term}} - \underbrace{\frac{1}{\rho} \frac{\partial \langle p'v' \rangle}{\partial y}}_{\text{Pressure diffusion term}} + \underbrace{v \frac{\partial^2 \langle k \rangle}{\partial y \partial y}}_{\text{Viscous diffusion term}} + \\
 & \underbrace{- \langle u'v' \rangle \frac{\partial U}{\partial y}}_{\text{Production term}} - \underbrace{v \left\langle \frac{\partial u'_i}{\partial x_j} \frac{\partial u'_i}{\partial x_j} \right\rangle}_{\text{Dissipation}} \quad \text{with } i, j = 1, 2, 3 \\
 & \underbrace{\hspace{10em}}_{\text{Source terms}}
 \end{aligned} \tag{4.12}$$

where $k = (u'^2 + v'^2 + w'^2)/2$ is the turbulent kinetic energy and i, j are indexes which identify the streamwise, wall-normal and spanwise directions. In Eq.4.12 the definition of five distinct terms is given:

- *the Production term*, which represents the production of turbulence kinetic energy. By means of it, kinetic energy is subtract from the mean flow to feed the turbulent fluctuations. It is generally active at large scale and it gives most of its contribution in the buffer region;
- *the Dissipation term*, which expresses the dissipation of turbulence kinetic energy. By means of it, turbulent kinetic energy is dissipated into heat due to viscosity;
- *Three transport terms*, which describes the transport of turbulent kinetic energy due to the pressure fluctuations, turbulence itself, and viscous stresses. A negative value of transport term means that turbulent kinetic energy is drained to feed other regions while a positive value means that energy is received from other regions. This concept can be further explained by looking equation 4.12 as:

$$\frac{\partial \phi}{\partial t} = \psi \tag{4.13}$$

where ϕ is the sum of the turbulent fluxes, i.e $\phi = - \langle kv' \rangle - \langle p'v' \rangle + v \frac{\partial \langle k \rangle}{\partial y}$ while ψ is the source term. As a matter of fact by looking at the sign of turbulent fluxes, it is possible to assert that their negative value is associated to a migration of the flow toward the wall, while a positive one to a migration towards the free surface.

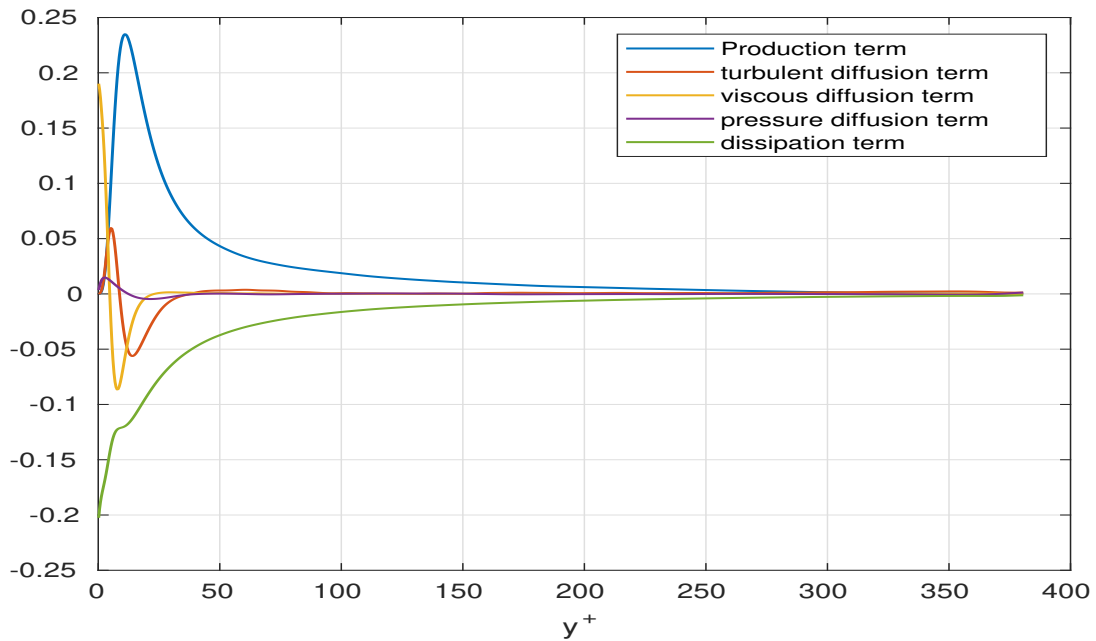
Figure 4.12 represents the budget of turbulent kinetic energy for the simulated open channel. As it can be seen, in the viscous sublayer the dissipation shows a very high value with respect to the negligible production term, which instead reaches its maximum value in the buffer layer. In the region where the mean

velocity profile follows the log-law ($70 < y^+ < 180$), the difference between the values of production and dissipation terms can be considered negligible and the production rate equalizes the dissipation one. At $y^+ > 180$, where free-surface effects become evident, the dissipation is larger than the production, but in the immediate vicinity of the free-surface ($y^+ = 370$) the dissipation rapidly decreases indicating the presence of large-scale vortices. Looking at the transport terms, a predominance of viscous transport is shown in the immediate wall proximity while just outside the viscous sublayer, viscous and turbulence terms start to be comparable. Close to the free-surface a positive value for the total transport term occurs. This is due to the impermeability condition imposed at the free-surface.

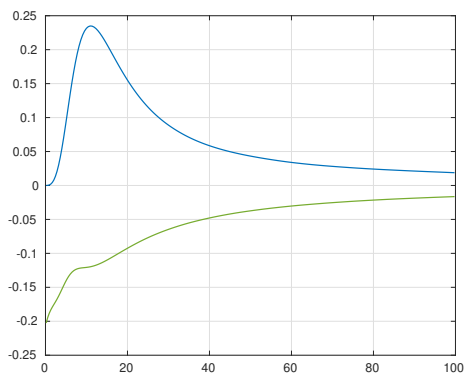
Finally a spectral analysis has been performed by investigating the turbulent velocity spectra. According to the theory, velocity spectra consist of three ranges:

- *the Production range* characterized by low wave numbers due to the fact that turbulent production occurs at large scales. In this region the velocity spectrum generally follows the k^{-1} law, as explained by V.Nikora [20];
- *the Inertial subrange*, where the turbulent energy is not produced or dissipated, it is only transferred from larger to smaller turbulent scales giving rise to the so called energy cascade. In this range the velocity spectrum shows a $k^{-5/3}$ dependency with the wave number;
- *the Viscous range*, where spectra decay much faster than in the inertial subrange due to dissipation. It is characterized by small turbulent scale and so by high wave numbers.

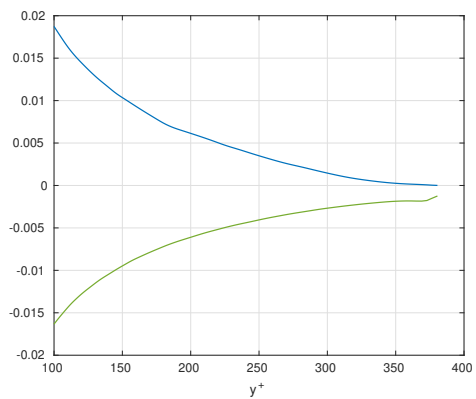
Figure 4.13 and 4.14 show the one-dimensional velocity spectra at two different heights, where k_z and k_x denote the wavenumber in the spanwise and streamwise direction respectively. As it can be seen from Figure 4.13(a) both the streamwise and wall normal velocity spectra show a peak respectively at $k_z \approx 14.66$ and $k_z \approx 16.75$. They can be associated to the characteristic wave length of the streamwise velocity streak spacing and the streamwise vortex size. Looking at the wall normal velocity spectrum, it is clear how the production region occurs for intermediate wave numbers, generating a reversed energy cascade by which turbulent energy is transfer from smaller to larger scales. Instead, far from the wall turbulent production is limited to large scales and most of the velocity spectra are dominated by the inertial subrange (see Figure 4.13(b)). By evaluating the velocity spectra along the streamwise direction (look at Figure 4.14), it is clear how close to the wall the production extends up to relatively high wave numbers while far from the wall the transfer of turbulent energy dominates for almost the whole wave numbers range.



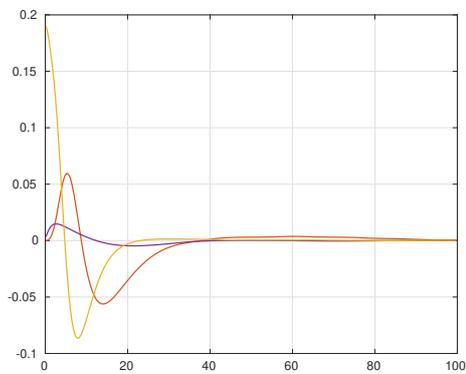
(a) Budget of turbulent kinetic energy



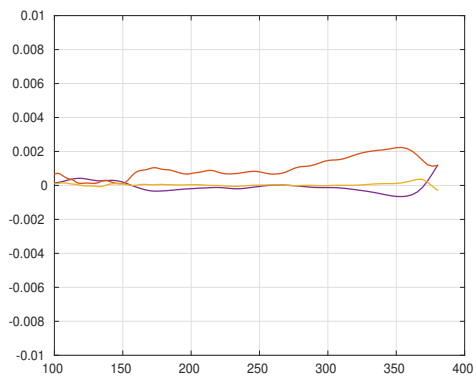
(b) Budget of source terms near the wall



(c) Budget of source terms near the free-surface

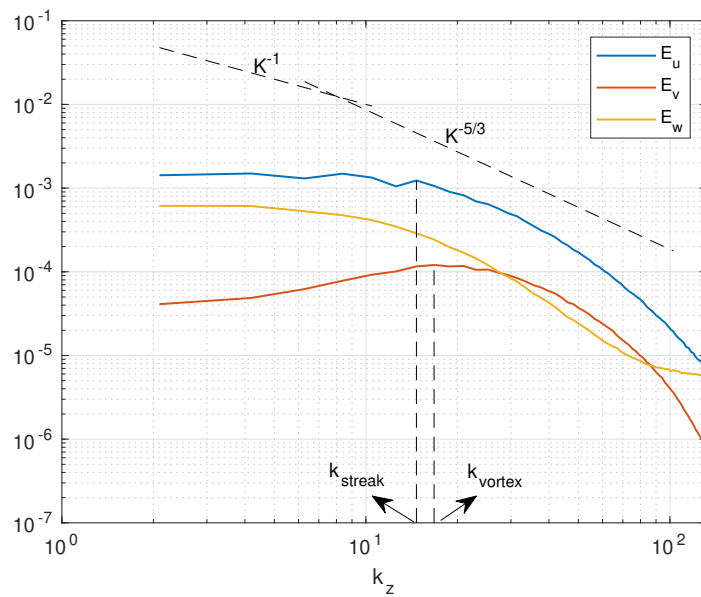


(d) Budget of transport terms near the wall

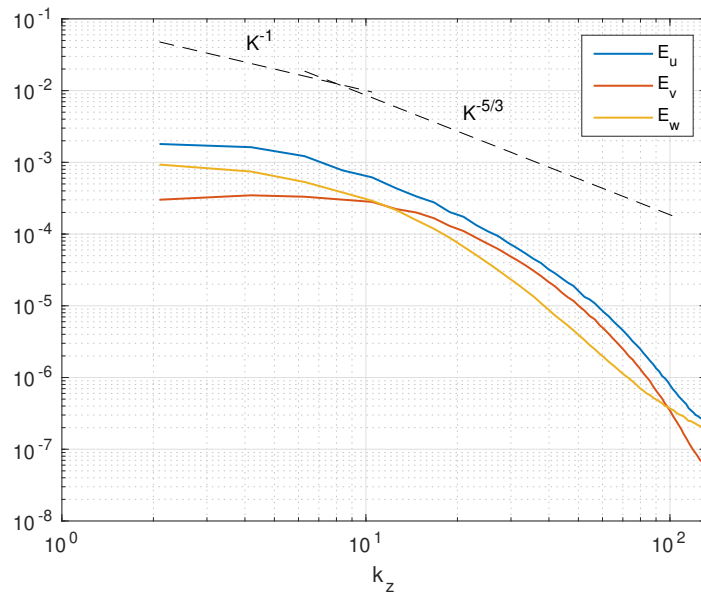


(e) Budget of transport terms near the free surface

Figure 4.12: Budget of turbulent kinetic energy

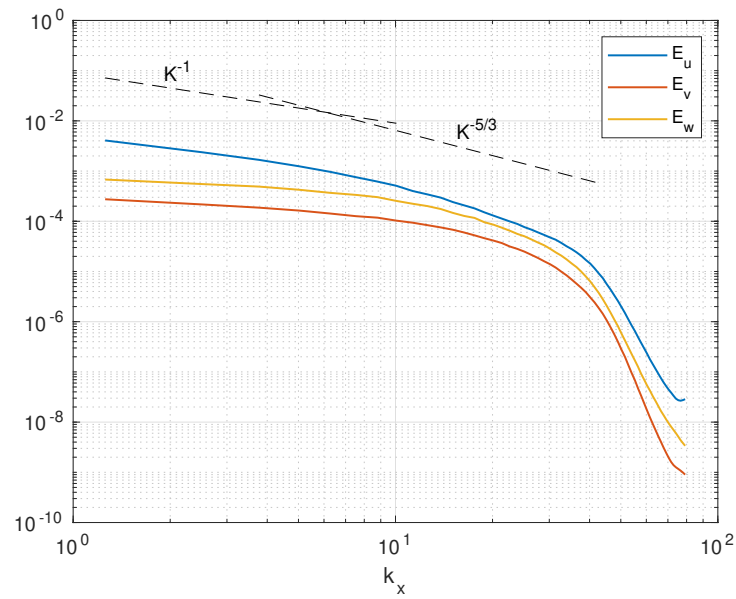


(a) Velocity spectra in the spanwise direction at $y^+ = 30$

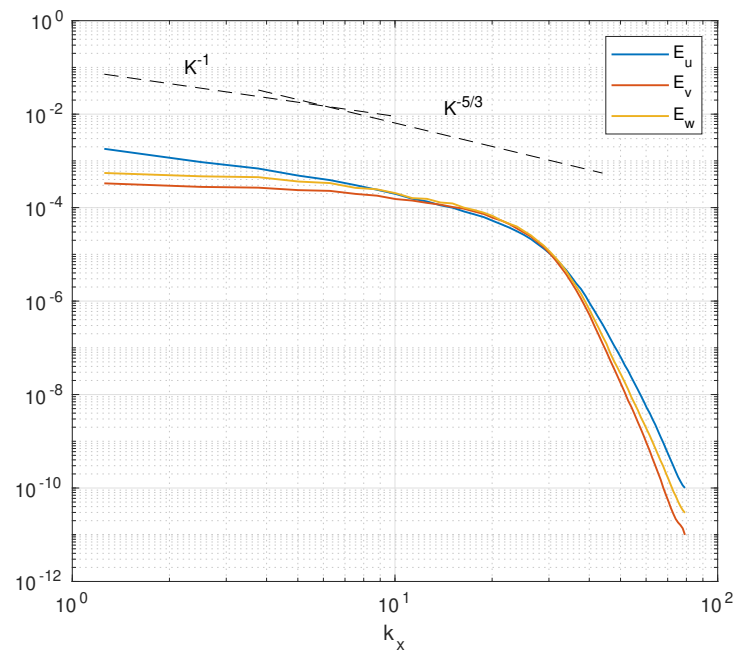


(b) Velocity spectra in the spanwise direction at $y^+ = 120$

Figure 4.13: Velocity spectra in the spanwise direction.



(a) Velocity spectra in the streamwise direction at $y^+ = 30$



(b) Velocity spectra in the streamwise direction at $y^+ = 120$

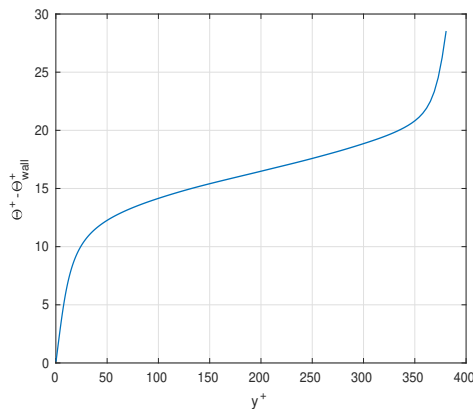
Figure 4.14: Velocity spectra in the streamwise directions

4.2.2.2 Turbulent passive heat transport statistics

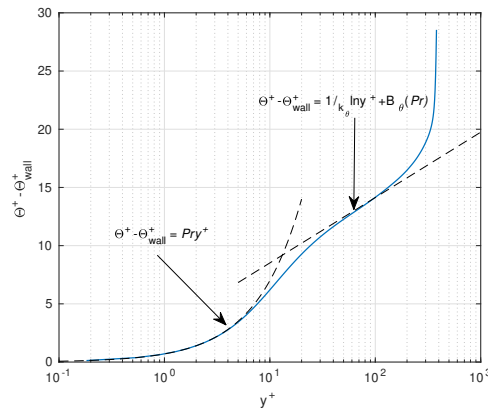
As for velocity, the heat transport statistics of the fully developed open channel flow have not dependence on x and z ($\frac{\partial}{\partial x} \langle \rangle = 0$ and $\frac{\partial}{\partial z} \langle \rangle = 0$). This means that in case of a passive scalar the average heat transport equation can be reduced to:

$$0 = \frac{\partial}{\partial y} \left(\lambda \frac{\partial \Theta}{\partial y} - \langle v' \theta' \rangle \right) \quad (4.14)$$

where $\Theta = \Theta(y)$ is the mean temperature profile, θ' are the temperature fluctuations and $-\langle v' \theta' \rangle$ is the wall-normal turbulent heat flux. The mean temperature profile has been plotted in Figure 4.15. In analogy with the the mean velocity profile, there exists a so called conduction sublayer, where the mean temperature linearly varies with the distance from constant temperature surfaces, showing a proportionality constant equal to the Prandtl number. The conduction sublayer can be localized in the immediate proximity both of the wall and free surface where two fixed values for temperature field have been chosen as boundary conditions. From the wall distance $y^+ \approx 70$ to approximately $y^+ \approx 120$, it is possible to see the matching of the mean temperature profile with a log-low having a von Karman constant equal to $\kappa_\theta \approx 0.41$ and B_θ dependent on the Prandtl number. Since the mean temperature profile has been plotted with respect to the wall distant, the linearity relation with the free surface distance and the subsequent logarithmic low can not be visualized. In Figure 4.16(a), the streamwise turbulent heat flux $\langle u' \theta' \rangle$ and the temperature



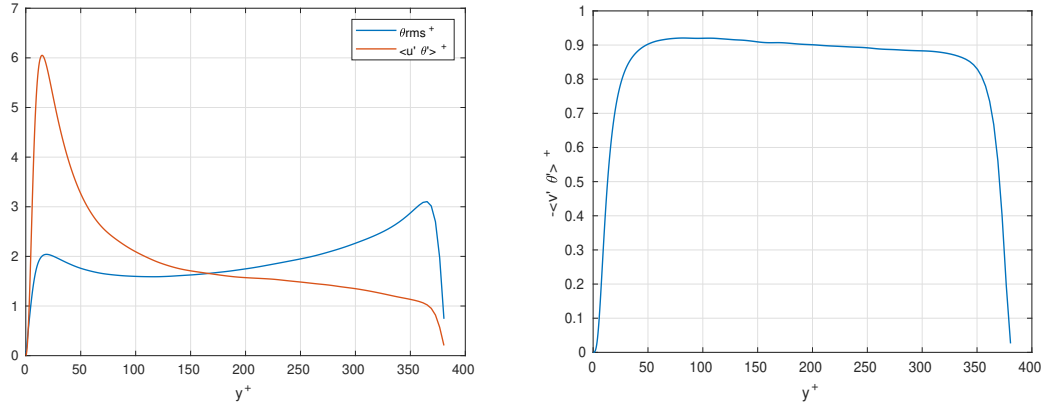
(a) Mean temperature profile



(b) Mean temperature profile in a semi-logarithmic scale

Figure 4.15: Mean temperature profile

variance θ_{rms} are represented. Looking at θ_{rms} , it can be seen as the temperature fluctuations show two different peaks near the wall and the free surface, this is



(a) Streamwise turbulent heat flux and temperature variance profile.

(b) Spanwise turbulent heat flux

Figure 4.16: Streamwise turbulent heat flux and intensity of heat transfer profile.

due to the different temperature gradients occurring on them. The high value of streamwise turbulent heat flux in the near wall regions with respect to the free-surface proximity, can be justified by the Prandtl number. As a matter of fact for $Pr = \nu/\lambda = 0.7$, the time scale of the temperature diffusion is slower compared to the time scale of the fluid motion and therefore the velocity fluctuations give a major contribution on the heat flux with respect to the temperature fluctuations. The wall-normal heat flux profile is shown in Figure 4.16(b). As it can be seen, the effect of the higher temperature gradient close the free stream is balanced by the smaller value of the relative wall-normal velocity fluctuations, giving a more or less constant wall-normal turbulent heat flux (except in proximity of the wall and the free surface).

Keeping the analogy with the velocity statistics analysis, the temperature balance have been proposed in order to deeply investigate the temperature fluctuations:

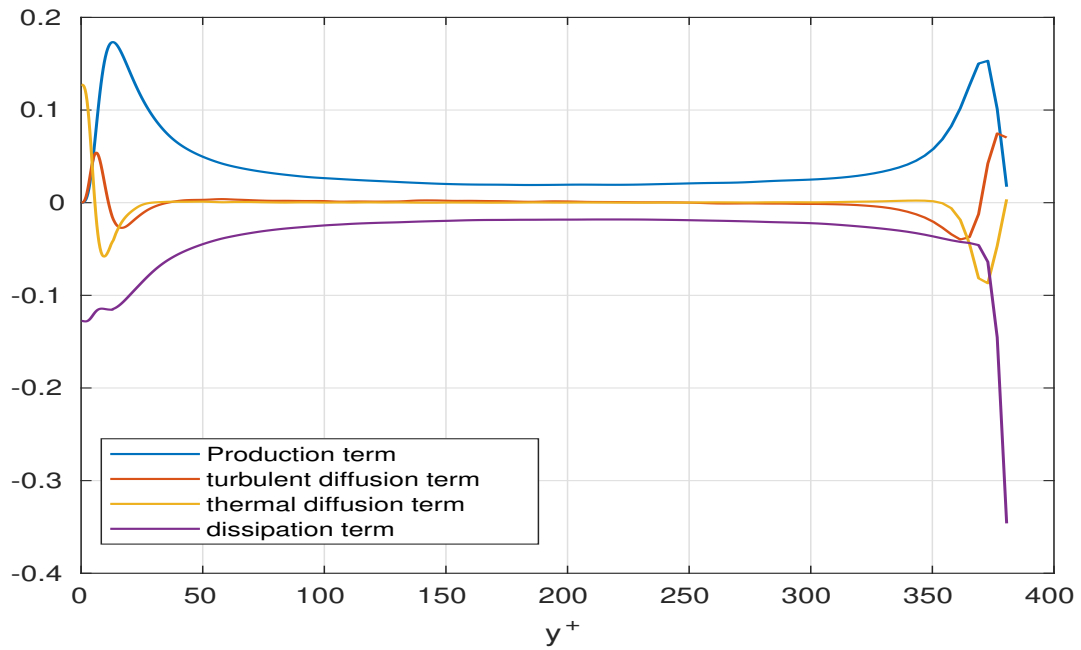
$$\begin{aligned}
 \frac{\partial \langle \theta'^2 \rangle}{\partial t} &= \underbrace{-\frac{1}{2} \frac{\partial \langle v' \theta'^2 \rangle}{\partial y}}_{\text{Turbulent diffusion term}} + \underbrace{\frac{\lambda}{2} \frac{\partial^2 \langle \theta'^2 \rangle}{\partial y \partial y}}_{\text{Thermal diffusion term}} \\
 &\quad \underbrace{\hspace{10em}}_{\text{Transport terms}} \\
 &= \underbrace{-\langle v' \theta' \rangle \frac{\partial T}{\partial y}}_{\text{Production term}} + \lambda \underbrace{\langle \frac{\partial \theta'}{\partial x_j} \frac{\partial \theta'}{\partial x_j} \rangle}_{\text{Dissipation}} \quad \text{with } j = 1, 2, 3 \\
 &\quad \underbrace{\hspace{10em}}_{\text{Source terms}}
 \end{aligned} \tag{4.15}$$

In Eq.4.15 the definition of four distinct terms is given:

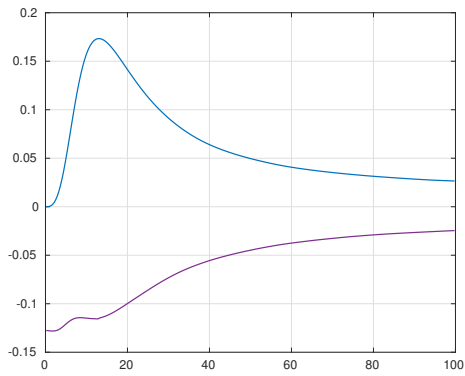
- *the Production term*, which represents the production of temperature fluctuations. By means of it, the temperature is subtract from the mean temperature to feed the temperature fluctuations. It gives most of its contribution in the near wall and free-surface regions;
- *the Dissipation term*, which expresses the dissipation of temperature fluctuations. Its maximum contributions are localized in the immediate proximity of the wall and free surface where the conductive sublayer occurs.
- *Two transport terms*, which describes the transport of temperature fluctuation due to the turbulence and thermal diffusivity.

Figure 4.17 shows the thermal budget for the simulated open channel. In the wall proximity (up to $y^+ \approx 5$) the flow is characterized by a very high value for dissipation and a negligible value of production. This can be explained by the presence of the conduction sublayer: the fixed temperature imposed at the wall damps the temperature fluctuations creating even smaller turbulent scales towards the wall. After the conduction sublayer, the buffer region occurs. It is characterized by a positive contribution of the source terms, reaching a production peak in the range between $y^+ \approx 10$ and $y^+ \approx 20$. As confirmed by the perfect balance between the dissipation and production terms, the logarithmic region can be localized between $70 < y^+ < 350$. It is then followed again by a buffer region and a subsequent conduction sublayer. Close to the free surface, the production and dissipation behavior should be analogous to the that of the wall region, but while the production term is in good agreement with physics of the phenomenon the the dissipation one is not. This can be explained by the cell size increment towards the free surface: since the production is a large scale phenomenon is not considerably affected by the lower resolution while the small scale nature of dissipation causes a wrong estimation of its value. Looking at the transport terms, a predominance of viscous thermal diffusion is shown in the immediate wall proximity while just outside the conduction sublayer, thermal and turbulence terms start to be comparable.

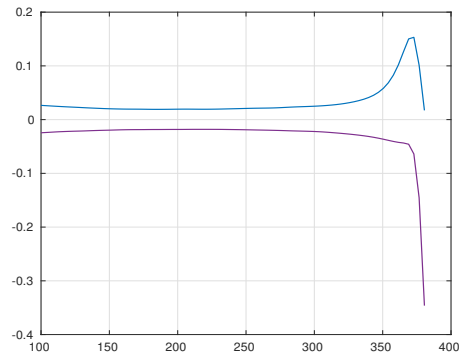
Figure 4.18 shows the one-dimensional temperature spectra along the streamwise and spanwise directions at two different wall-distances. As it can be seen from Figure 4.18(a) the spectrum computed at $y^+ = 30$ shows a peak at $k_z = 14.66$, that can be associated to the characteristic wave length of thermal streak spacing. Looking at both the streamwise and the spanwise spectra it is clear how close to the wall the production extends up to relatively high wave numbers while far from the wall the transfer of turbulent energy dominates for almost the whole wave number range.



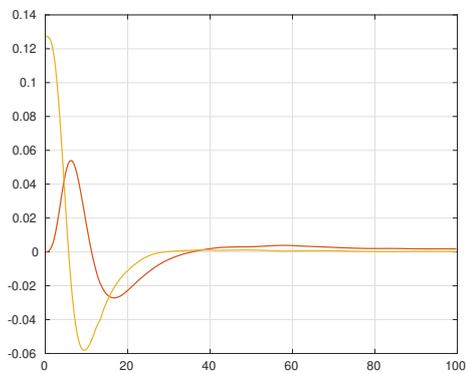
(a) Budget of turbulent heat transfer



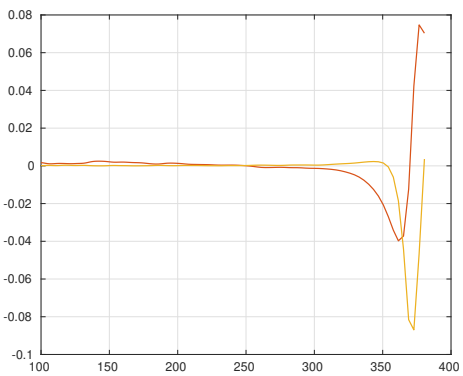
(b) Budget of source terms near the wall



(c) Budget of source terms near the free-surface



(d) Budget of transport terms near the wall



(e) Budget of transport terms near the free-surface

Figure 4.17: Budget of turbulent heat transfer

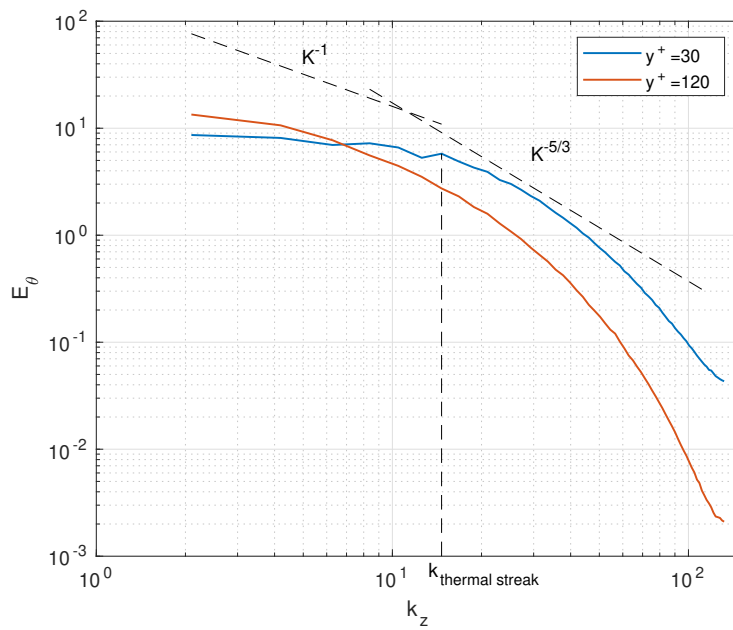
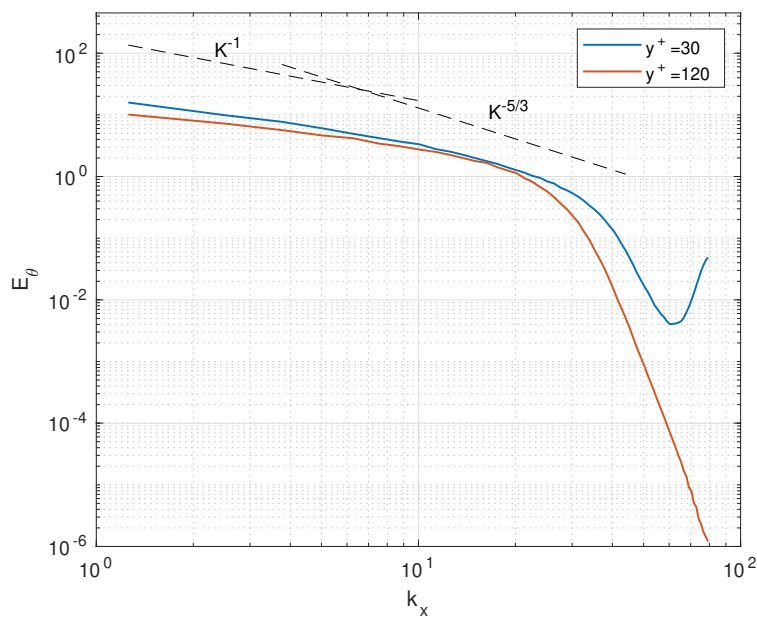
(a) *Temperature spectra in the spanwise direction*(b) *Temperature spectra in the streamwise direction*

Figure 4.18: Temperature spectra

Chapter 5

Turbulent water channel

In this chapter, momentum and passive heat transfers across a sheared wind-driven gas–liquid interface have been investigated by means of a DNS of two-phase open channel flow. As for the turbulent open channel, pre-processing, simulation running and post-processing are performed by using the same softwares:

- **OpenFOAM**[®], involved for most of the pre-processing and simulation running;
- **ParaView**, used to visualize all the coherent turbulent structures of the gas-phase flow and the wave height evolution on time;
- **Matlab**, employed for part of the pre-processing and to compute all the statistical quantities describing the flow.

5.1 Simulation details

Because of the two-phase nature of the flow, the simulation has been performed by means of the modified solver *my_interFoam* described in Chapter 3. All the simulation setting and parameters are collected and explained in the following subsections.

5.1.1 Physical system and Mesh properties

The flow geometry and the coordinate system are illustrated in Figure 5.1. As for the open channel flow, u , v and w are the streamwise, wall-normal and spanwise velocity components respectively; l_x , l_y and l_z represent the length, height and width of the system domain and finally T_{top} and T_{bottom} are the temperature of the air free surface and wall, held constant during the simulation. All the numerical

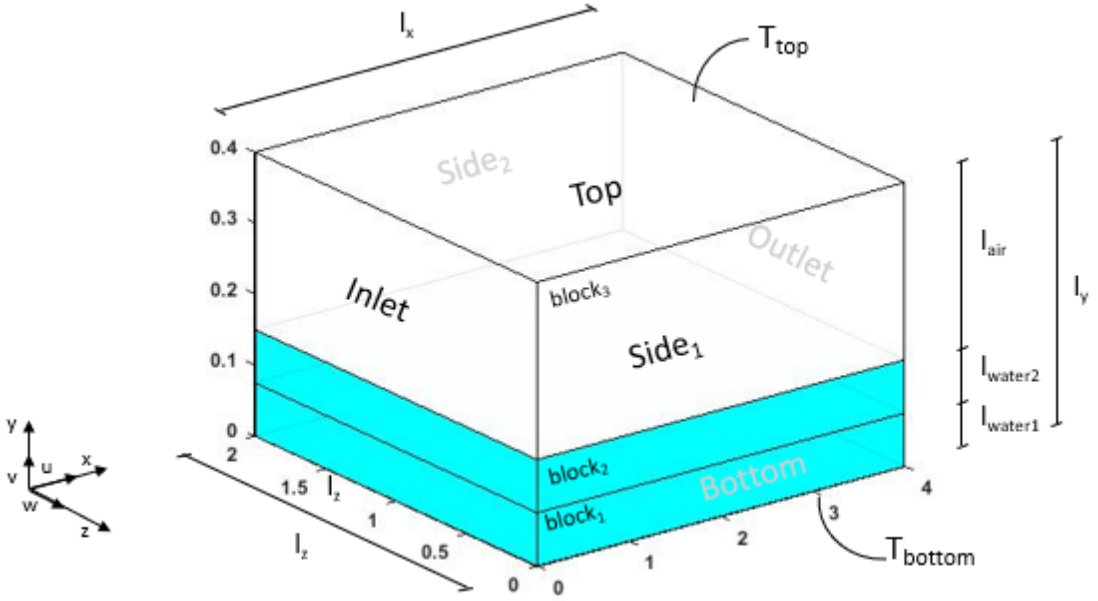


Figure 5.1: Flow geometry

Re_τ	Grid Points			Domain Sizes			U_{bar}^+	Nu	Pr_{air}	Pr_{water}
	N_x	N_y	N_z	l_x	l_y	l_z				
327.4	256	205	192	4m	0.4 m	2 m	15.2	4.9	0.7	0.5

Table 5.1: Numerical conditions

conditions are summarized in Table 5.1. In order to accurately analyzed the wave properties and the wind boundary layer an higher mesh resolution is required close the air-water interface, while a coarser mesh can be employed for the water column where the velocity field is expected to be practically null . With this in mind the domain has been divided in three blocks along the wall normal direction. As reported in Table 5.2, each block is characterized by an own height, an own number of elements in the y-direction and an own coefficient R , that represents the ratio between the last and the fist cell again in the y-direction. Since all the blocks show the same length, width and number of grid elements along the streamwise and spanwise directions, the dimensionless parameters for mesh resolution Δx^+ , Δz^+ , can be computed as:

$$\Delta x^+ = \frac{\Delta x}{l_v} = \frac{l_x}{N_x l_v} = 20.5$$

	Grid Points			Block Size			R	Block Resolutions		
	N_x	N_y	N_z	l_x	l_y	l_z		Δx^+	Δy_{min}^+	Δz^+
Block 1	256	25	192	$4m$	$l_{water1} = 0.075m$	$2m$	6	20.5	1.4	13.6
Block 2	256	45	192	$4m$	$l_{water2} = 0.075m$	$2m$	0.036	20.5	0.26	13.6
Block 3	256	135	192	$4m$	$l_{air} = 0.25m$	$2m$	30	20.5	0.27	13.6

Table 5.2: Domain discretization

$$\Delta z^+ = \frac{\Delta z}{l_v} = \frac{l_z}{N_z l_v} = 13.6$$

In order to understand how the dimensionless resolution Δy^+ varies along the domain height, its maximum and minimum values have to be computed inside each block.

- **Block 1** Since for the first block R is larger than 1, the sizes of the smallest and largest cell are given by:

$$\Delta y_{min} = l_{water1} \frac{R_1^{\frac{1}{N_{y1}-1}} - 1}{R_1^{\frac{N_{y1}}{N_{y1}-1}} - 1} = 0.00106m \quad \Delta y_{max} = R_1 \Delta y_{min} = 0.0064m$$

Therefore in the first block the smallest and larger dimensionless resolutions along the y-direction are:

$$\Delta y_{min}^+ = \frac{\Delta y_{min}}{l_v} = 1.4 \quad \Delta y_{max}^+ = \frac{\Delta y_{max}}{l_v} = 8.4$$

- **Block 2** Since R is smaller than 1, the second block shows a mesh resolution decreasing with the wall-distance. Therefore the sizes of the smallest and largest cell are given by:

$$\Delta y_{min} = l_{water2} \frac{R_2^{\frac{1}{N_{y2}-1}} - 1}{(1 - R_2^{\frac{-N_{y2}}{N_{y2}-1}} - R_2^{\frac{-1}{N_{y2}-1}}) R_2^{\frac{1}{N_{y2}-1}} - 1} = 0.0002m$$

$$\Delta y_{max} = \frac{\Delta y_{min}}{R_2} = 0.0057m$$

while the smallest and larger dimensionless resolutions along the y-direction can be computed as:

$$\Delta y_{min}^+ = \frac{\Delta y_{min}}{l_v} = 0.26 \quad \Delta y_{max}^+ = \frac{\Delta y_{max}}{l_v} = 7.46$$

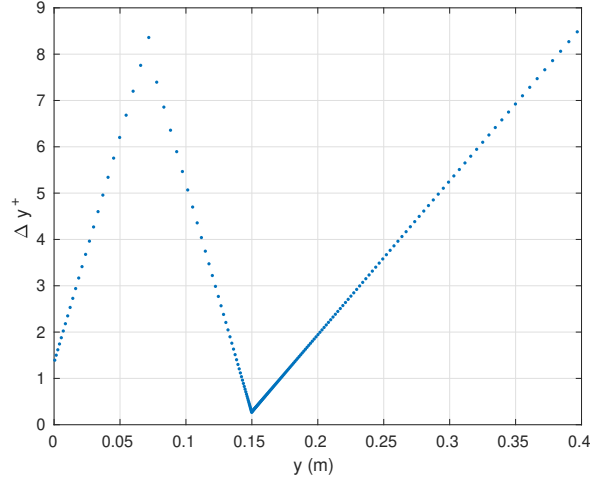


Figure 5.2: Dimensionless resolution in the wall-normal direction

- **Block 3** Similarly to the first block, for the third block the smallest and larger dimensionless resolutions along the y-direction are:

$$\Delta y_{min} = l_{air} \frac{R_3^{\frac{1}{N_{y3}-1}} - 1}{R_3^{\frac{N_{y3}}{N_{y3}-1}} - 1} = 0.00021m \quad \Delta y_{max} = R_3 \Delta y_{min} = 0.0064$$

$$\Delta y_{min}^+ = \frac{\Delta y_{min}}{l_v} = 0.27 \quad \Delta y_{max}^+ = \frac{\Delta y_{max}}{l_v} = 8.38$$

In Figure 5.2 it has been reported the evolution of the dimensionless resolution in the wall normal direction along the domain height.

5.1.2 Boundary conditions

Since what has to be simulated is still an open channel, the boundary conditions are the same of those used for the single-phase channel flow and are recapped in Table 5.3. Here the static pressure p has been substitute with another kind of pressure indicated as p_{rgh} . This is due to the fact that both *interFoam* and *my_interFoam* do not use the static pressure in the computation because it complicates the settings of the boundary conditions: since the static pressure contains inside a term due to the hydrostatic component $\rho \vec{g} \vec{x}$, all the boundary conditions on pressure are function of the position of the cell. Instead if a new variable, called static contact pressure and defined as $p_{rgh} = p - \rho \vec{g} \vec{x}$, is substituted inside the momentum equation, uniform boundary conditions on p_{rgh} can easily be defined over the whole domain, without considering where is a fluid rather than another.

Variable	Patches			
	Top	Bottom	Sides	Inlet/Outlet
U	Slip	No slip	Cyclic	Cyclic
p_{rgh}	Zero Gradient	Zero Gradient	Cyclic	Cyclic
α	Zero Gradient	Zero Gradient	Cyclic	Cyclic
T	Fixed value at 288K	Fixed value at 303K	Cyclic	Cyclic

Table 5.3: Boundary conditions

5.1.3 Initial conditions

The initial condition for the velocity fields plays a very important role on the wave development and consequently on the wind boundary layer turbulent structures. In the present simulation a highly perturbed wind is considered to blow over a water column at rest without any kind of disturbance applied on the two-fluid interface. In order to translate this particular initial condition in terms of initial velocity field some steps have been followed:

1. By using the same strategy described in Chapter 4, the velocity field relative to the last time sample of the *Open Channel* simulation has been mapped in a temporary channel having the same dimensions of the *Water channel* third block. Afterwards some time steps for the temporary channel have been simulated. This is done in order to avoid a grainy velocity field as initial condition. As a matter of fact, a stretched velocity field mapped in a very fine mesh could result in a strong gradient, that close to the interface translates into a compressible water flow.
2. The complete velocity field has been reconstructed by means of a Matlab script, that assigned a null velocity value $\vec{u} = (0, 0, 0)$ to each points inside the water column (first and second bolcks) and maps the velocity field of the simulated temporary channel in the third block.
3. Finally the velocity field written in a Matlab format has been transformed in a compatible file with OpenFOAM[®] and used as initial condition for the *Water channel* (see Figure 5.3 a)

Giving as initial condition a uniform temperature value for the whole domain could lead to a slow achievement of temperature stationarity, therefore a procedure similar to the velocity fields has been followed to initialize temperature:

1. The temperature field relative to the last time sample of the *Open Channel* simulation has been mapped in the temporary channel, that has run for some time steps.
2. The complete temperature field has been reconstructed by means of a Matlab script. In the water column, the temperature has been made varying between $T_{bottom} = 288K$ and $T_{interface} = 300.5K$ with the following linear law:

$$\begin{cases} 288 = q \\ 300.5 = 0.15m + q \end{cases} \implies T(y) = 83.3y + 288 \quad \text{with } 0 \leq y \leq 0.15$$

The air temperature field has been obtained rescaling the temperature field of the simulated temporary channel by means of a linear function computed with a $T_{interface}$ equal to $300.5K$ instead of $288K$:

$$\begin{cases} 1 = 0.4m + q \\ \frac{300.5}{288} = 0.15m + q \end{cases}$$

↓

$$\begin{cases} f(y) = -0.172y + 1.068 \\ T(y) = T_{\text{temporary channel}}(y)f(y) \quad \text{with } 0.15 \leq y \leq 0.4 \end{cases}$$

3. Finally the temperature field has been written in a compatible format with OpenFOAM[®] and used as initial condition for the *Water channel* (see Figure 5.3 (b))

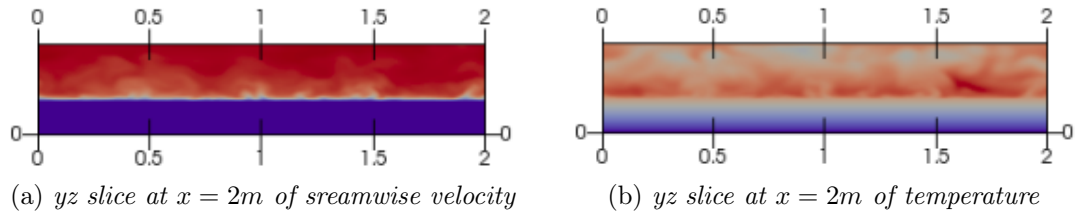


Figure 5.3: Initial temperature and velocity fields

As regard the volume fraction α , it has been initialized to 1 in the first and second blocks while to 0 in the third one. Finally, a zero value for the static contact pressure p_{rgh} has been considered in the whole domain.

5.1.4 General simulation characteristics

- **The external forcing of the system**

As for the single-phase open channel flow, the two-phase open channel flow is driven by means of a pressure gradient. This is initialized by imposing the average velocity U_{bar} in the *fvOption* file:

```
21
22     momentumSource
23     {
24     type            meanVelocityForce;
25     active          yes;
26     meanVelocityForceCoeffs
27     {
28     selectionMode   all;
29     fields          (U);
30     Ubar            (0.295 0 0);
31     }
32     }
33
```

fvOptions file

- **Transport properties**

All the flow transport properties are recapped in the *transportProperties* file, partially reported in the following

```
20
21     water
22     {
23     transportModel  Newtonian;
24     nu              [0 2 -1 0 0 0 0] 1e-06;
25     rho             [1 -3 0 0 0 0 0] 1000;
26     DT              [0 2 -1 0 0 0 0] 2e-6;
27     }
28
29     air
30     {
31     transportModel  Newtonian;
32     nu              [0 2 -1 0 0 0 0] 1.48e-05;
33     rho             [1 -3 0 0 0 0 0] 1;
34     DT              [0 2 -1 0 0 0 0] 2.114e-5;
```

```

35     }
36     sigma          [1 0 -2 0 0 0 0] 0.07;
37

```

transportProperties file

As it can be seen for each phase three quantities are specified: the kinematic viscosity, the density and the thermal diffusivity. Some words need to be spend for the water thermal diffusivity. As it has already been specified the thermal diffusivity is computed starting from the Prandtl number as:

$$\lambda = \frac{\nu}{Pr}$$

Since for water at $293K$ the Prandtl number is about 7, the water thermal diffusivity would be equal to $\lambda_w = 1.43 \times 10^{-7} m^2/s$. In order to be numerically stable, an advection-diffusion equation as Eq.3.29, must respect a limitation on the maximum value of a certain quantity called Peclet number. The Peclet number is defined as the ratio between the advection and diffusion transport rates and for each cell of the domain it can be expressed as:

$$Pe = \frac{\text{advection transport rate}}{\text{diffusion transport rate}} = \frac{T \frac{\delta t}{\delta x}}{\lambda \frac{\delta t}{\delta x^2}} = \delta x \frac{T}{\lambda}$$

Since the water thermal diffusivity is very small, the increment on the Pe number could be so high to exceed the limitation value and cause numerical instability in temperature computation. In order to avoid this problem an higher value of water thermal diffusivity is considered. As can be seen from the *transportPropertie* file, a λ_w of $2 \times 10^{-6} m^2/s$ has been chosen: this is the results of a trade off between the numerical stability, for which an higher λ_w is required, and the good representation of the heat transfer, where a large difference between the air and water thermal diffusivity determines an easier temperature diffusion in air rather then in water.

- **Turbulent properties**

In order to run a Direct Numerical Simulation (DNS), all the possible turbulent models have to be deactivated.

- **Time control** For a two-phase flows simulation, it is not enough imposing the $Co < 1$ to achieve temporal accuracy and numerical stability. A further Courant number, controlling the stability, of the advection equation for the volume fraction (Eq.3.20) has to be considered and imposed lesser than 1.

```

49
50 maxCo          1;
51 maxAlphaCo    1;
52

```

controlDict file

- **Numerical schemes**

All the numerical schemes presented in the current simulation are listed and briefly explained in Table 5.4

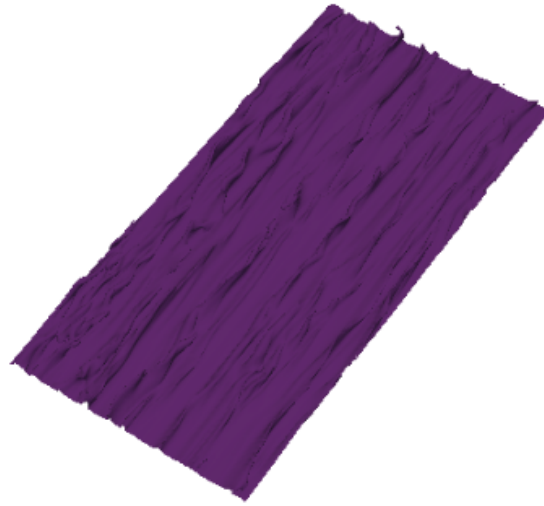
Operator	Numerical scheme
Time Derivative	Euler Implicit. It is a first order implicit time scheme and its region of absolute stability includes the whole left half of the complex plane. This makes the Euler Implicit scheme suitable for the solution of stiff equations.
Divergence	Gauss linear
Gradient	Gauss linear
Laplacian	Gauss linear corrected

Table 5.4: Normal schemes

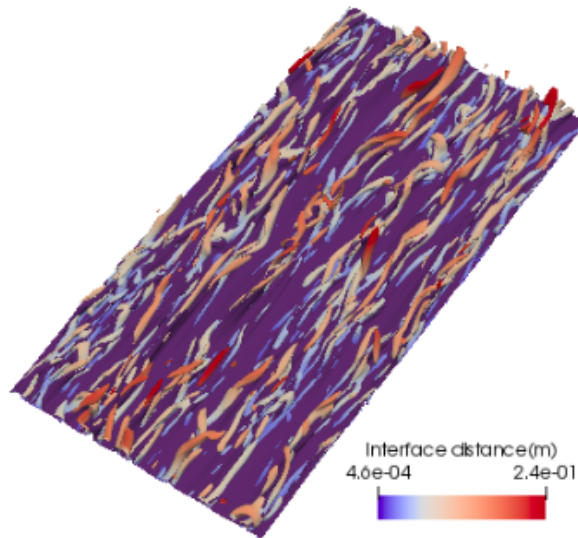
5.2 Results

5.2.1 Wind turbulent structures

In the current section, the turbulent structures generated close the interface are analyzed and compared with the wall turbulent structure described in Chapter 4. Streaks and streamwise vortices are visualized in Figure 5.4 by looking at isosurfaces of λ_2 equal to -0.8 and streamwise velocity of $0.4m/s$. The comparison between Figure 5.4 (b) and Figure 4.5 (b) shows the presence of more elongated turbulent structures in the two-phase open channel case. This can be explained by considering a dynamic roughness associated to the wave development: the wave motion effect on the air boundary layer can be comparable to that induced by a wall with a changeable roughness. The larger size of the turbulent structure can be confirmed also by plotting the two point correlation of the streamwise and wall-normal velocity fluctuations, R_{uu} and R_{vv} , in the spanwise direction. As shown



(a) *3D visualization of streaks*



(b) *3D visualization where streaks are colored purple while streamwise vortices by means of interface distance.*

Figure 5.4: Streaks and spanwise vortices

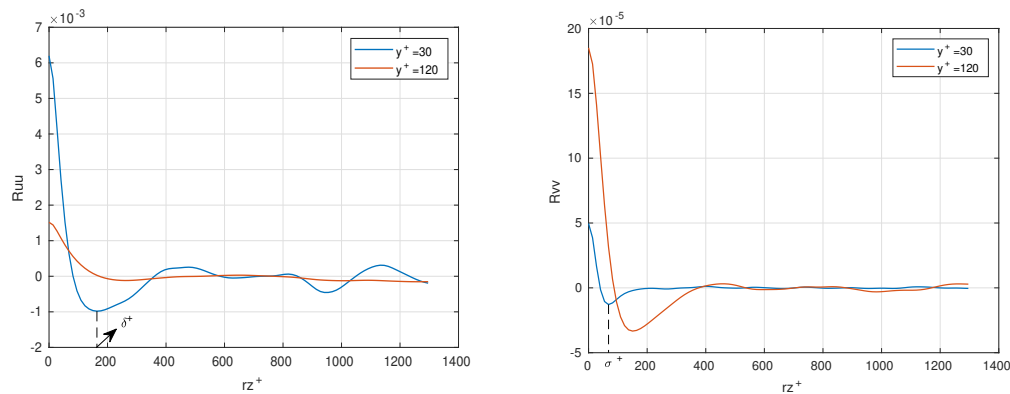


Figure 5.5: Two points correlations of wall-normal and streamwise velocity fluctuations

in Figure 5.5, the minimum values of R_{uu} and R_{vv} , associated to dimensionless streaks spacing δ^+ and spanwise vortex size σ^+ , are larger than the corresponding values for the single-phase open channel flow:

$$\delta^+ = \frac{\delta}{l_v} = \frac{r_{zmin}}{l_v} \approx 163.7$$

$$\sigma^+ = \frac{\sigma}{l_v} = \frac{r_{zmin}}{l_v} \approx 68.2$$

The presence of wave motion has also an analogous effect on thermal turbulent structures: the thermal streaks visualized in Figure 5.6 show a more elongated shape along the streamwise direction. This highlights once again the analogy, between temperature and velocity fields that can be further observed by looking at Figure 5.7, where yz and xz slices of streamwise velocity and temperature fields are reported.

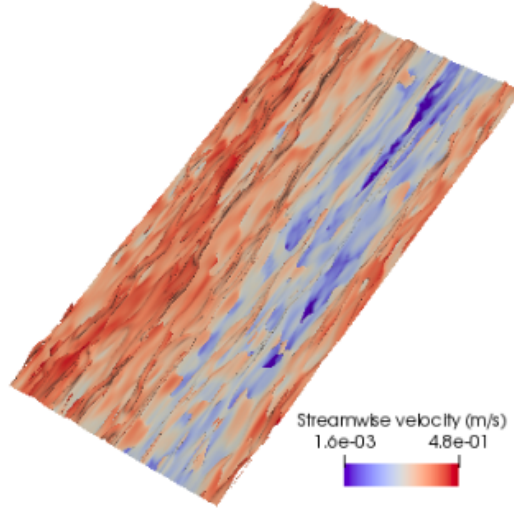


Figure 5.6: 3D visualization of thermal streaks computed for $T = 302K$.

5.2.2 Statistics

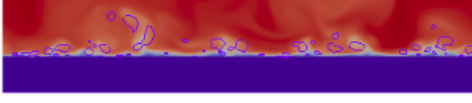
The evaluation of the statistical quantities may start only once all the processes considered in the flow analysis have reached the stationarity. As already explained, to investigate the stationarity of momentum and temperature transfer, the time evolutions of the friction Reynolds number Re_τ and Nusselt number Nu , computed close the interface, have to be monitored. In order to evaluate the stationarity of the wave state, the time stability of a further parameter has to be achieved. As a matter of fact the wave motion can be evaluated by computing the root mean square of the wave elevation as

$$\tilde{h}_{rms}(t) = \sqrt{\frac{1}{N_x N_z} \sum_{i=1}^{N_x} \sum_{k=1}^{N_z} (h(x_i, z_k, t) - H)^2} \quad (5.1)$$

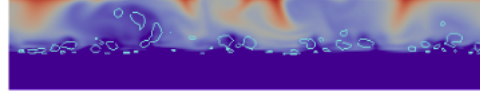
where H is the mean water depth height and $h(x, z, t)$ is the water depth defined as the distance of the interface from the wall:

$$h(x, z, t) = y_{\text{interface}}(x, z, t). \quad (5.2)$$

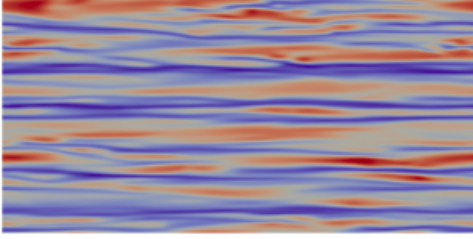
It has been found that two of the three parameters stabilize around a constant value after 300s (Figure 5.8). Even if the \tilde{h}_{rms} has not reach yet the stationarity conditions, the statistical quantities have been calculated starting from 300s because of time limitations giving by the high computational costs of the simulation. Therefore all the statistics presented in this chapter have been evaluated starting from the



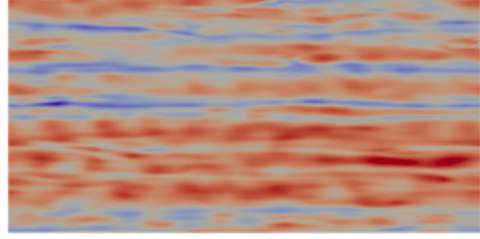
(a) *yz slice at $x = 2m$ of streamwise velocity with isolines of $\lambda_2 = -0.8$*



(b) *yz slice at $x = 2m$ of temperature (rescaled in a range between 302K and 303K) with isolines of $\lambda_2 = -0.8$*



(c) *xz slice at $y = 0.16m$ of streamwise velocity*



(d) *xz slice at $y = 0.16m$ of temperature*

Figure 5.7: Slices

time average of the velocity field, temperature field and water depth, considering a time window going from $t_0 = 300s$ to $t_f = 420s$ with a sample time $t_s = 5s$ and a number of samples $N = 25$. Therefore the time and spatially averaged velocity field, temperature field and water depth are calculated as follows:

$$U_j(y) = \langle \tilde{U}(y, t) \rangle = \frac{1}{N} \sum_{n=1}^N \tilde{U}_j(y, t_n) \quad \text{with } j = x, y, z \quad (5.3)$$

$$\Theta(y) = \langle \tilde{\Theta}(y, t) \rangle = \frac{1}{N} \sum_{n=1}^N \tilde{\Theta}(y, t_n) \quad (5.4)$$

$$H = \langle \tilde{H}(t) \rangle = \frac{1}{N} \sum_{n=1}^N \tilde{H}(t_n) = \frac{1}{N} \sum_{n=1}^N \left(\frac{1}{N_x N_z} \sum_{i=1}^{N_x} \sum_{k=1}^{N_z} h(x_i, z_k, t_n) \right) \quad (5.5)$$

5.2.2.1 Turbulent velocity statistics

In order to calculate the wind boundary layer statistics, first the water free surface has to be localized. Wall turbulence is generally analyzed by referring to a constant wall position in time, so it is simple to know exactly where the wall is located. The same thing can not be said for a wavy moving surface: the time-dependent wave

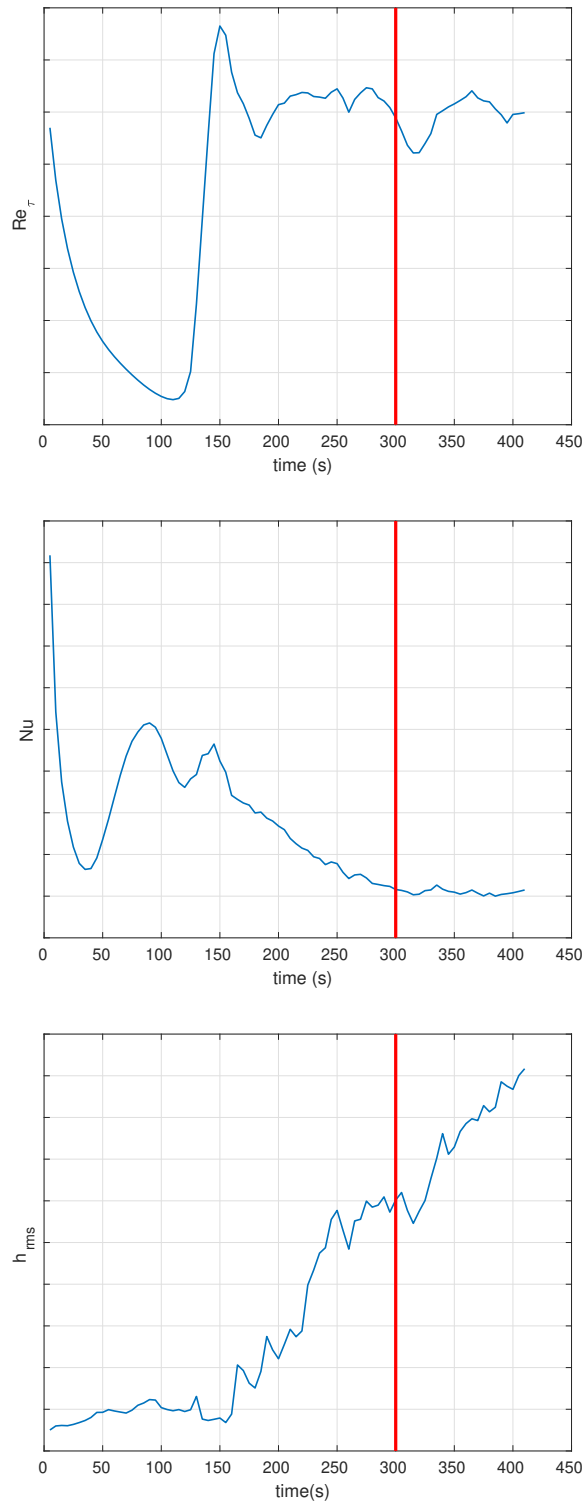


Figure 5.8: time evolution of \tilde{Re}_τ , \tilde{Nu} and \tilde{h}_{rms}

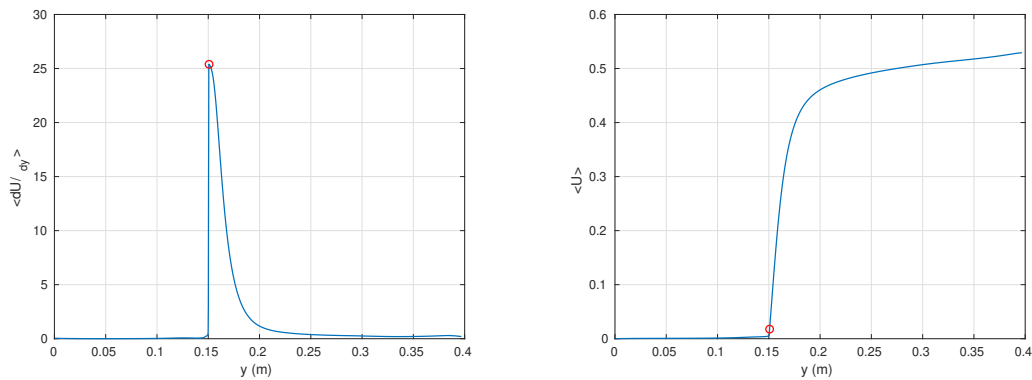


Figure 5.9: Plots of mean velocity gradient and mean velocity profiles where the red circle, localized at $y = 0.1508m$, identifies the interface position.

state makes more complicated to identify the interface and a method to establish the exact location of the water free surface along the wall normal direction is required. By considering the analogy with the wall turbulence, it is possible to assert that the interface can be localized in correspondence of the maximum of mean velocity gradient, as shown in Figure 5.9. Following this criterion the mean velocity and wall normal coordinates can be rescaled in order to get the usual law of wall turbulence. As for the single-phase open channel flow, four different layers can be seen by plotting the mean velocity profile of the wind boundary layer (Figure 5.10):

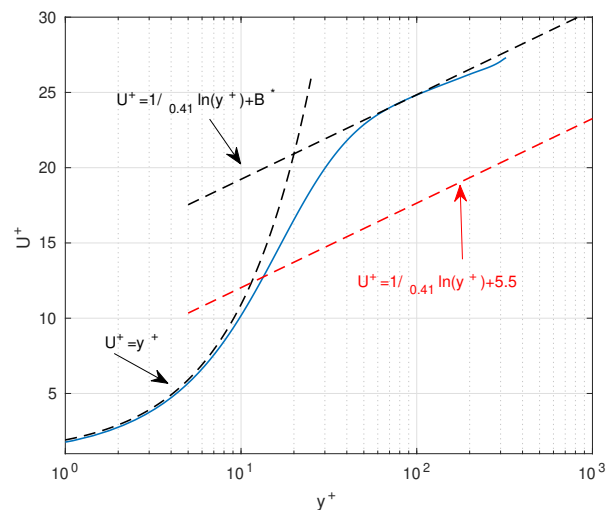


Figure 5.10: Mean velocity profile

- *the viscous sublayer*, that is characterized by a linear relation between the mean velocity and the distance from water free surface and extends up to $y^+ \approx 5$;
- *the buffer layer* roughly localized in the interval between $y^+ \approx 5$ and $y^+ \approx 70$;
- *the logarithmic region*, that has a smaller extension with respect to the single-phase open channel flow. As a matter of fact it starts at $y^+ \approx 70$ and extends up to $y^+ \approx 100$. Because of the wave presence, the mean velocity evolution can be described by the logarithmic law associated to a turbulent flow over a rough wall

$$U^+ = \frac{1}{\kappa} \log(y^+) + B^* \quad (5.6)$$

where κ is equal to 0.41 while B^* is a little bit different from the usual values since it depends on the roughness induced by the wave state. The B^* constant is usually determined as:

$$U^+ = \frac{1}{\kappa} \log\left(\frac{y^+}{y_0^+}\right) + B \implies B^* = B - \frac{1}{\kappa} \log(y_0^+) \quad (5.7)$$

where $B \approx 5.5$ and y_0^+ is the roughness length previously introduced in Chapter 2 and normalized with the inner length scale. By considering Eq 5.7 the roughness length can be expressed as:

$$y_0 = \frac{v_a}{u_\tau} e^{-\kappa(B^*-B)} \quad (5.8)$$

Since in this simulation a B^* value of 12.7 has been obtained, a roughness length of $3.98^{-5}m$ has been computed and therefore its dimensionless value is equal to $y_0^+ = y_0/l_v \approx 0.0522$. As it has been already pointed out in Chapter 2, most of the wind-wave coupling models use empirical equations to determine the roughness length (see Eq 2.14), therefore the procedure shown till now could be a good alternative in the y_0 evaluation;

- *the wake region* that extends from $y^+ \approx 100$ to the air free surface;

By looking at the turbulent intensity profiles in Figure 5.11, the effect of impermeability boundary condition on the upper wall is evident: the positive streamwise and spanwise fluctuations close the air free surface are the result of energy redistribution caused by the damping of wall normal fluctuations. Comparing Figure 5.11 with the turbulent intensity profiles of the single phase open channel, shown in Figure 4.10, some differences may be seen: firstly the relative magnitude of the streamwise fluctuations with respect to the spanwise and vertical ones, is much higher than in a wall bounded turbulent flow; secondly, the magnitude of u_{rms} is much higher

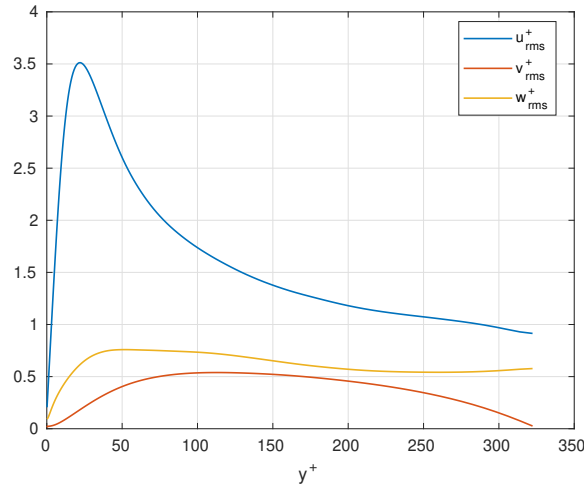


Figure 5.11: Turbulent intensity profiles.

than for the single-phase open channel and the peak, associated with the maximum of turbulent production, is moved towards the air free surface. Analogous considerations can be done also for Reynolds shear stress plotted in Figure 5.12: by taking into account Figure 4.11, it is clear how the absolute magnitude of $-\langle u'v' \rangle$ is reduced and its maximum value is reached for an larger interface distance.

Figure 5.13 represents the budget of turbulent kinetic energy for the two-phase open channel. As it can be seen, in the viscous sublayer the dissipation shows a lower value in magnitude with respect to the same term in the single-phase open channel: this means that the flow over the current wavy surface is less dissipative than the same flow over a smooth wall. According the production term, the magnitude is more or less comparable to the one computed in the single-phase case, but the maximum value is reached further away from the water free surface. Another difference arises in the localization of the logarithm region: the production rate equalizes the dissipation one only in a reduced region between $y^+ \approx 70$ and $y^+ \approx 100$. This is in good agreement with the mean velocity profile, which follows the logarithmic law exactly in the same range. Looking among the transport terms, the main difference is given by the turbulent diffusion one: it shows an higher magnitude in the outer region of the turbulent boundary layer. The large differences on the dissipation and turbulent transport term requires further consideration about the energy exchanges. According to the Kolmogorov's four-fifths law [23], one among the main features of a high Reynolds number turbulent flow is the energy transfer from large to small scales. In this theory the third-order structure function plays a very important role. The third-order structure function can be defined as

$$\langle \delta u_i^2 \delta u_j \rangle \quad \text{where} \quad \delta u_i = u'_i(x_j + r_j, t) - u'_i(x_j, t) \quad (5.9)$$

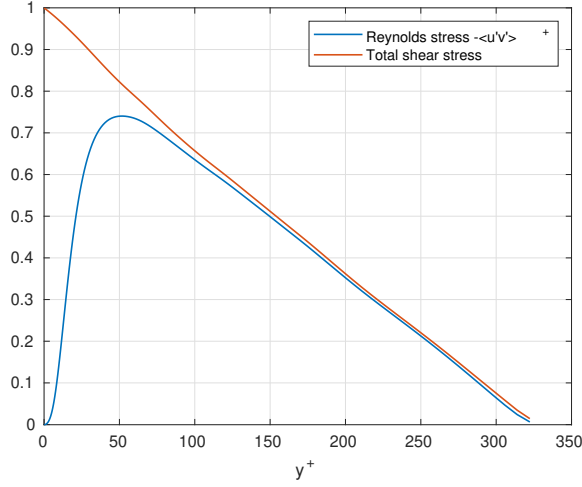
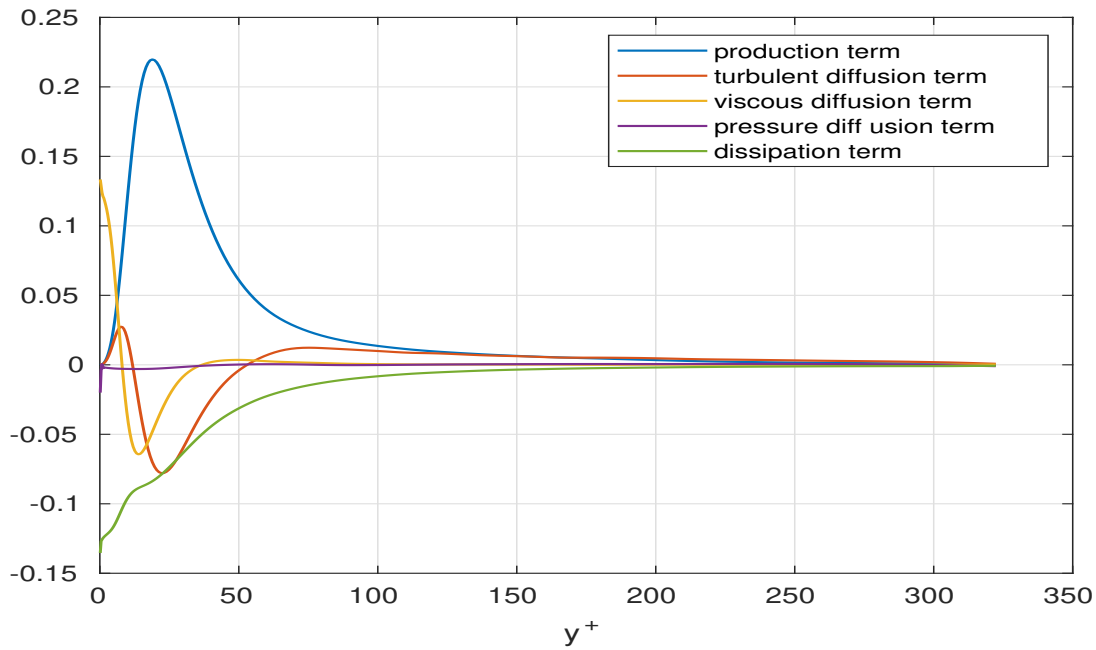


Figure 5.12: Shear stress profiles.

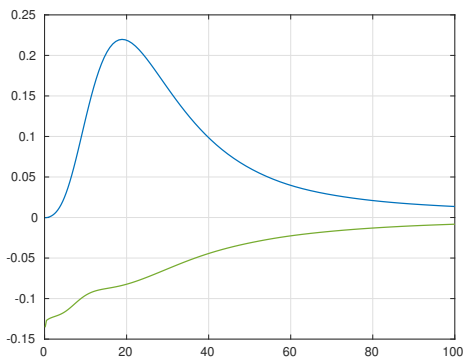
and according to Kolmogorov's theory, it is proportional to the separation distance r_j and to the average dissipation rate:

$$\langle \delta u_i^2 \delta u_j \rangle = -\frac{4}{5} \langle \epsilon \rangle r_j \quad (5.10)$$

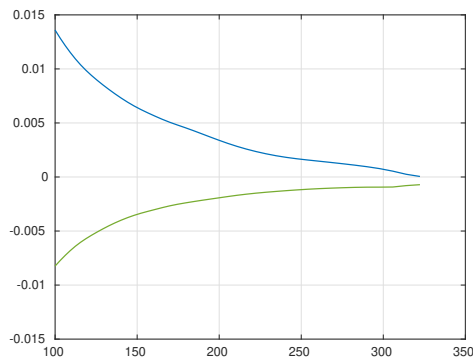
Therefore by looking at their evolution it is possible to have informations about the energy exchange between turbulent scales. In Figure 5.14, the streamwise and spanwise third-order structure functions have been plotted for two different interface distances. Analyzing these graphs, it is clear that along the streamwise direction the energy is normally transferred from large to small scales, while along the spanwise direction after a certain length scale, turbulent energy follows a reverse energy cascade and is transferred from small to large scales. This mechanism is at the basis of the generation of larger turbulent structures with respect to the wall-bounded case and could have strong repercussions both for turbulence theories and closures. The origin of such a phenomenon could be represented by the low dissipative nature of the water surface and hence by the tendency of the flow to transfer the near water surface energy excess towards the air interface rather than towards the water surface. Figure 5.15 and 5.16 show the one-dimensional velocity spectra at two different heights from the interface. As it can be seen from Figure 5.15(a), both the streamwise and wall normal velocity spectra show a peak respectively at $k_z \approx 21.99$ and $k_z \approx 43.98$, which are associated to the streaks spacing and streamwise vortex size. As for the single phase open channel, the production region of the wall normal velocity spectrum occurs at intermediate scales, generating the reversed energy cascade, that contrary to the single phase case, can be visible also at $y^+ = 120$. The main difference with respect to the single



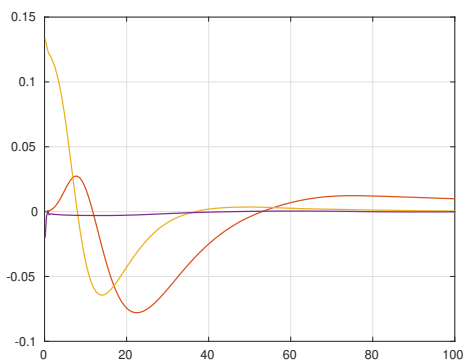
(a) Budget of turbulent kinetic energy



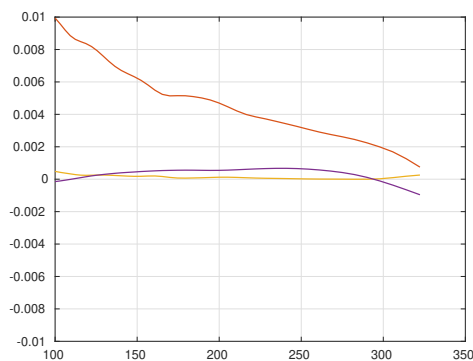
(b) Budget of source terms near the wall



(c) Budget of source terms near the free-surface

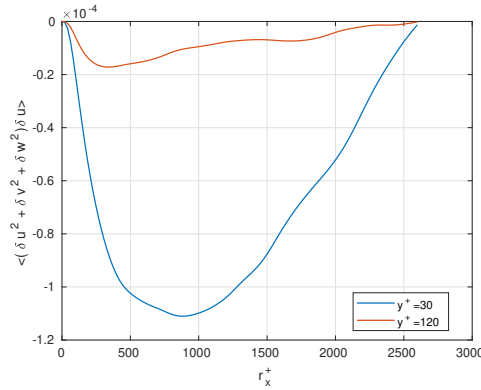


(d) Budget of transport terms near the wall

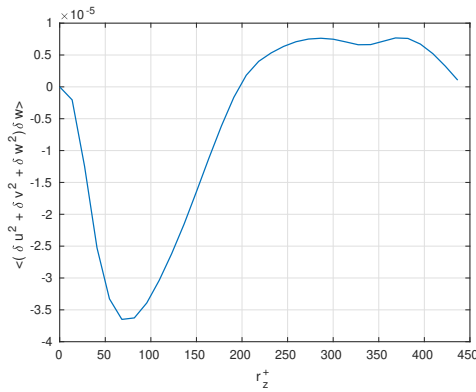


(e) Budget of transport terms near the free surface

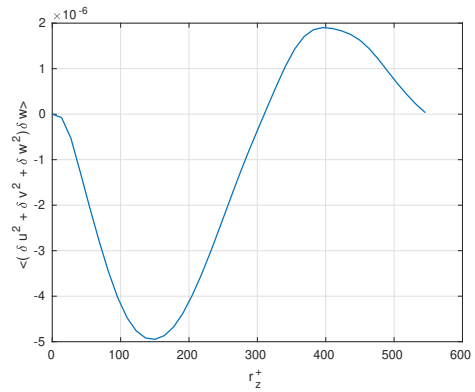
Figure 5.13: Budget of turbulent kinetic energy



(a) Third-order structure functions along the streamwise direction



(b) Third-order structure function along the spanwise direction computed at $y^+ = 30$



(c) Third-order structure function along the spanwise direction computed at $y^+ = 120$

Figure 5.14: Velocity structural functions

phase open channel is the higher magnitude of the streamwise velocity spectra where the production range seems to be extended up to intermediate scale both at $y^+ \approx 30$ and $y^+ \approx 120$. By evaluating the velocity spectra along the streamwise direction at $y^+ \approx 30$ (Figure 5.16 (a)), it can be seen how production occurs up to relative high wave number for wall-normal and spanwise velocity spectra, while the matching between K^{-1} and the slope of the streamwise velocity spectrum is restricted only to large length scales. At $y^+ = 120$ instead, all the spectra shows a trend very similar to the theoretical production curve up to relatively high wave numbers (Figure 15.6 (b)).

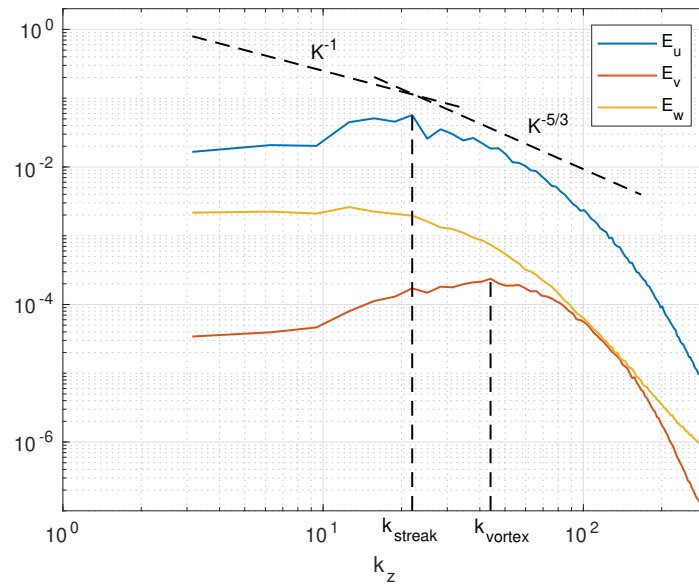
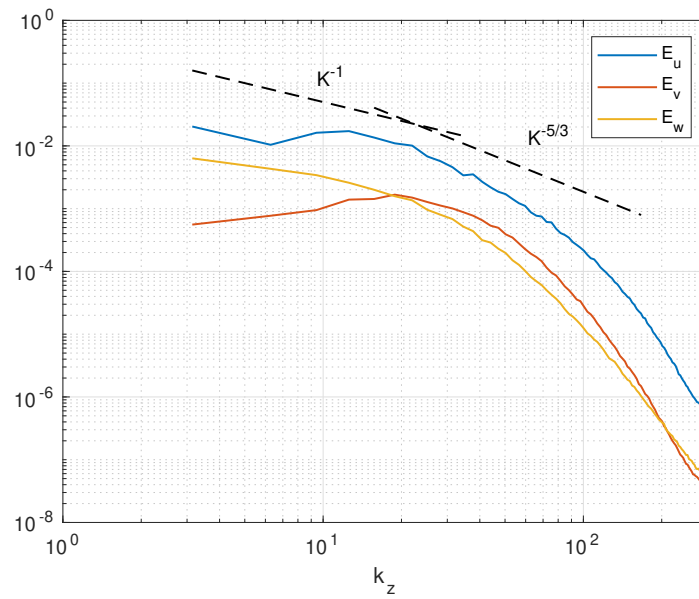
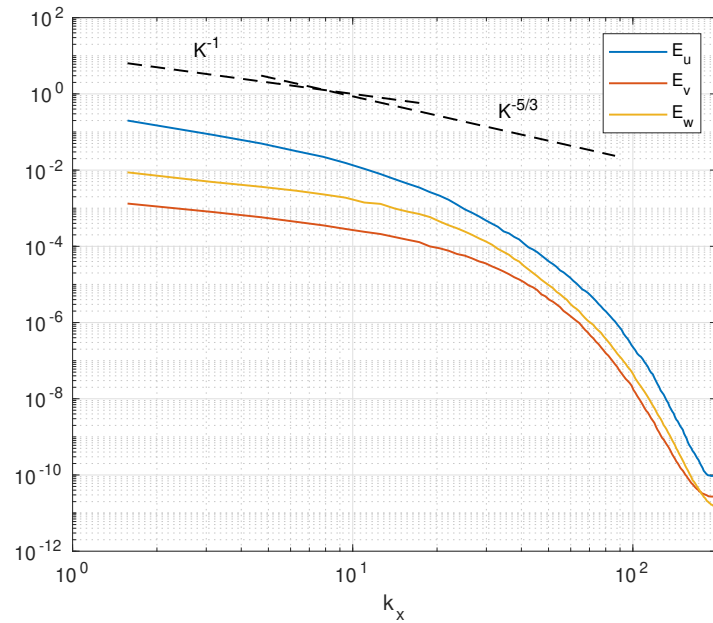
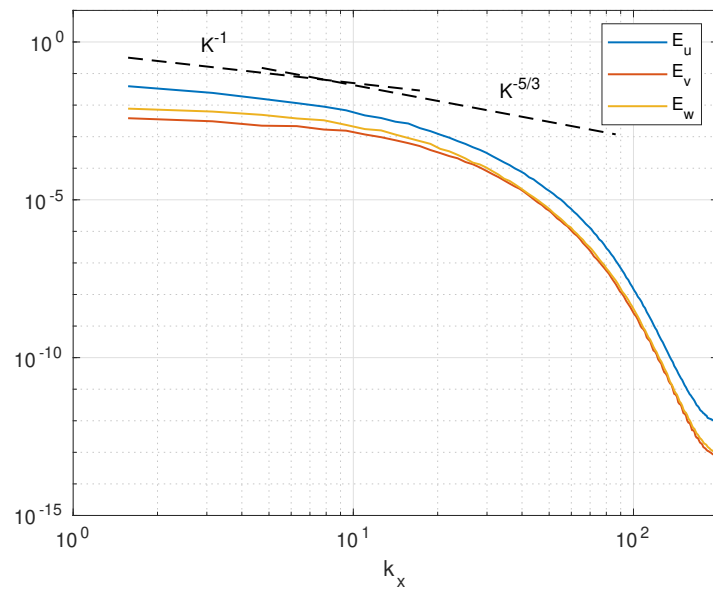
(a) Velocity spectra in the spanwise direction at $y^+ = 30$ (b) Velocity spectra in the spanwise direction at $y^+ = 120$

Figure 5.15: Velocity spectra in the spanwise direction.



(a) Velocity spectra in the streamwise direction at $y^+ = 30$



(b) Velocity spectra in the streamwise direction at $y^+ = 120$

Figure 5.16: Velocity spectra in the streamwise directions

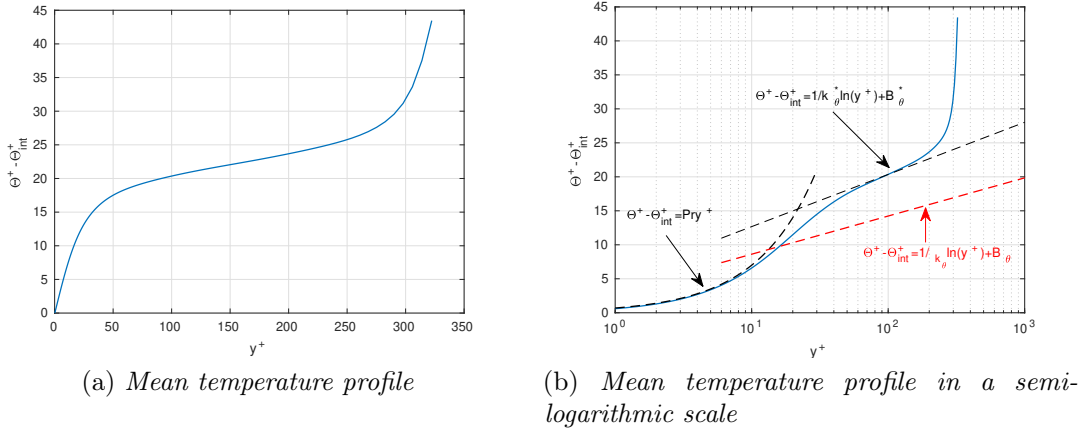


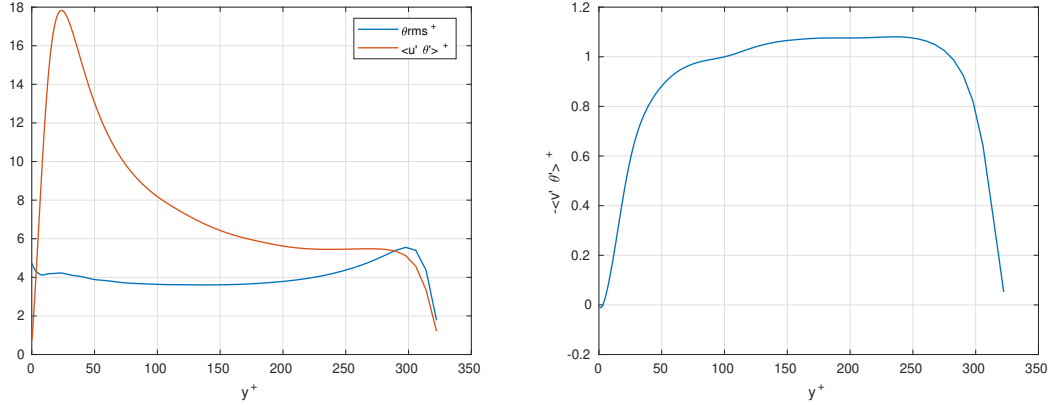
Figure 5.17: Mean temperature profile

5.2.2.2 Turbulent passive heat transport statistics

The mean temperature profile has been plotted in Figure 5.17 and has been computed rescaling the temperature field by means of a mean interface temperature equal to $\Theta_{int} = 301.68K$. As it can be seen in Figure 5.17 (b), close the interface the mean temperature profile shows a perfect matching with the theoretical value while in the logarithm region the roughness induced by the wave motion changes both the von Karman constant and B_θ modifying their values in κ_θ^* and B_θ^* , respectively. As for the single phase open channel, since the mean temperature profile has been plotted with respect to the interface distant, the linearity relation with the air free surface distance and the subsequent logarithmic law can not be visualized.

In Figure 5.18(a), the streamwise turbulent heat flux $\langle u'\theta' \rangle$ and the temperature variance θ_{rms} are represented. Looking at θ_{rms} , it can be seen that the temperature fluctuations do not show anymore a null value close the interface: this is due to the fact that the boundary condition of fixed temperature is not imposed at the interface so that the temperature fluctuations do not go to zero. The higher magnitude of the streamwise turbulent heat flux with respect to the single-phase open channel flow, can be justified by the higher values of both streamwise velocity and temperature fluctuations. Moreover its maximum value moves towards the air free surface just as the streamwise turbulent intensity profile. The wall-normal heat flux is plotted in Figure 5.18(b): contrary to the single phase open channel, it shows a lower value close to the interface and reaches the maximum in the proximity of the air free surface. This can be explained by the smaller values of wall-normal turbulent fluctuations near the interface with respect to the single phase case.

Figure 5.19 shows the thermal budget for the current simulation. In the interface proximity (up to $y^+ \approx 5$) the flow is characterized by a very high value (in magni-



(a) Streamwise turbulent heat flux and temperature variance profile.

(b) Spanwise turbulent heat flux

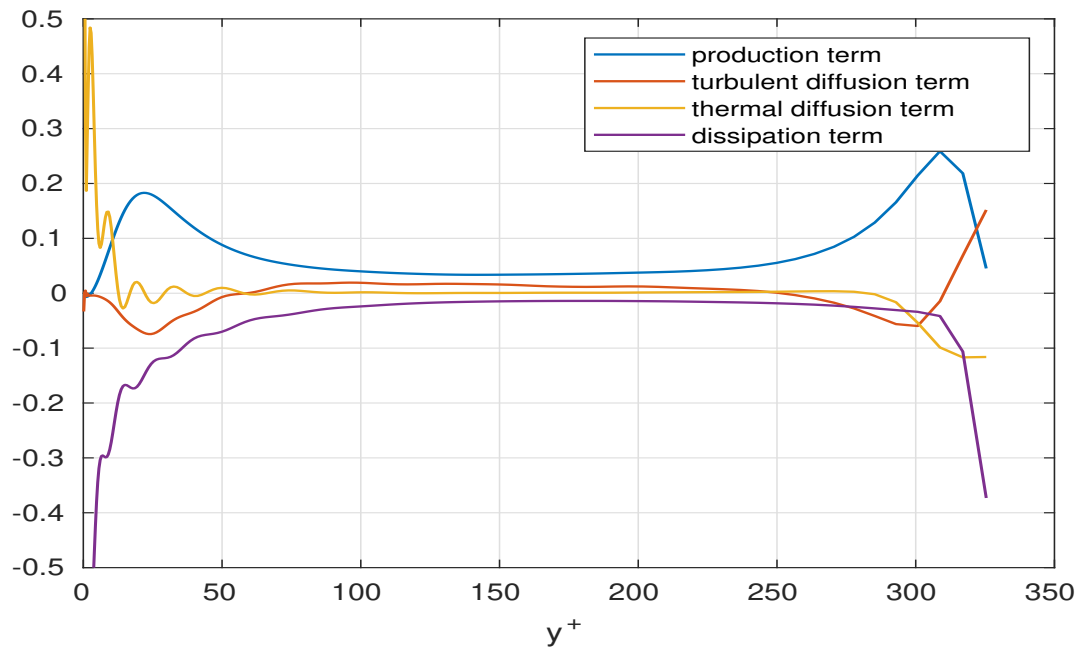
Figure 5.18: Streamwise turbulent heat flux and intensity of heat transfer profile.

tude) of dissipation: it is more or less one order greater than the corresponding single-phase open channel. In the buffer region, where a positive contribution of the source term occurs, the production peak has the same magnitude than the single-phase flow, but it is reached farther from the interface. As confirmed by the balance between the dissipation and production terms, the logarithmic region can be localized in a smaller range with respect to the open channel case, precisely between $80 < y^+ < 250$. Close to the air free surface both production and dissipation are comparable with the single-phase case. This is due to the fact that the boundary condition of fixed temperature is still applied on the upper wall. Looking at the transport terms in the interface proximity, an higher value of the viscous thermal diffusion is shown. It is also possible too see a lower value of turbulent diffusion term close the interface with respect to the single-phase open channel: this means a reduction of the wall-normal turbulent heat flux towards the interface.

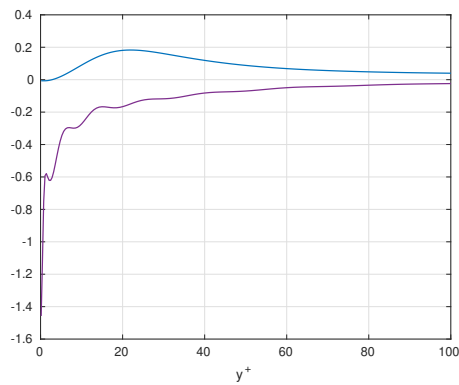
Further considerations about temperature exchanges can be done by considering the third-order temperature structure functions. As for velocity, the third-order temperature structure functions are defined as:

$$\langle \delta\theta^2 \delta u_j \rangle \quad \text{where} \quad \delta\theta = \theta'(x_j + r_j, t) - \theta'(x_j, t) \quad (5.11)$$

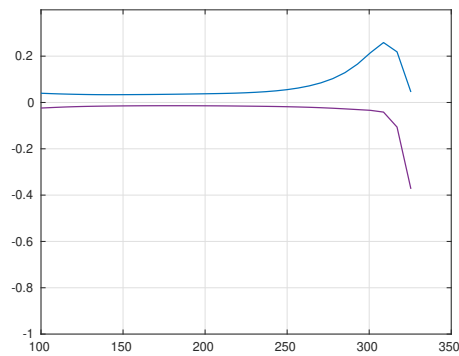
In Figure 5.20, streamwise and spanwise third-order temperature structure functions have been plotted for two different interface distances. As it can be seen from Figure 5.20 (a), along the streamwise direction the temperature is transferred from large to small scales. Looking at the third-order temperature structure functions



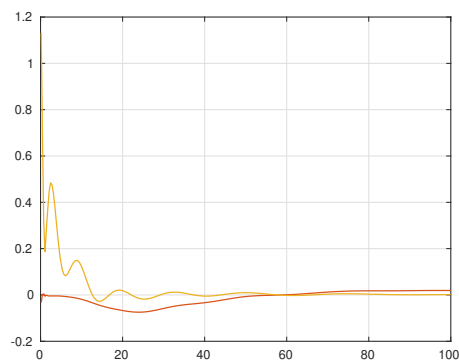
(a) Budget of turbulent heat transfer



(b) Budget of source terms near the wall



(c) Budget of source terms near the free-surface



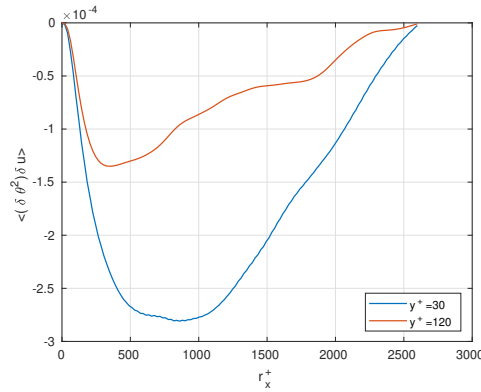
(d) Budget of transport terms near the wall



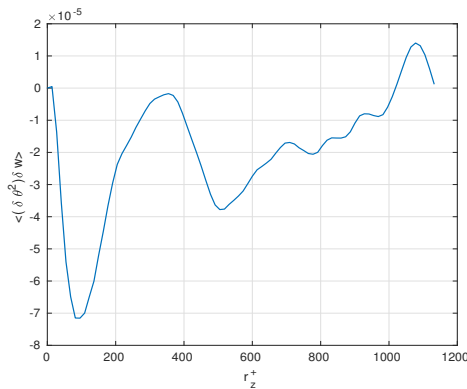
(e) Budget of transport terms near the free-surface

Figure 5.19: Budget of turbulent heat transfer

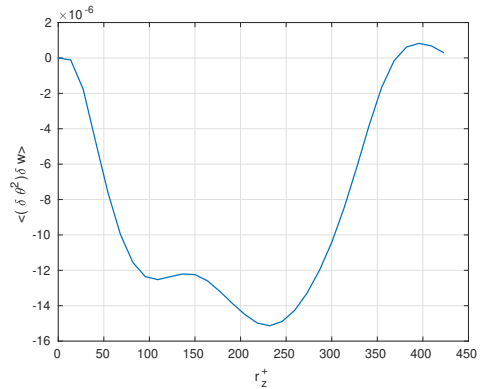
along the spanwise direction (Figure 5.20 (b) (c)), the effect of a reversed cascade is not so marked as for third-order velocity structure functions, therefore the temperature transfer from large to small scales dominates also in the spanwise direction.



(a) Third-order temperature structure function along the streamwise direction



(b) Third-order temperature structure function along the spanwise direction computed at $y^+ = 30$



(c) Third-order temperature structure function along the spanwise direction computed at $y^+ = 120$

Figure 5.20: Third-order temperature structure functions

Figure 5.21 shows the one-dimensional temperature spectra along the streamwise and spanwise directions at two different wall-distances. As it can be seen from Figure 5.21 (a) the spectrum computed at $y^+ = 30$ shows a peak at $k_z = 21.9$, that can be associated to the characteristic wave length of thermal streak spacing. Looking at both the streamwise and the spanwise spectra it is clear how close to the interface the production extends up to relatively small wave numbers with respect to the single phase open channel while transfer of turbulent energy dominates

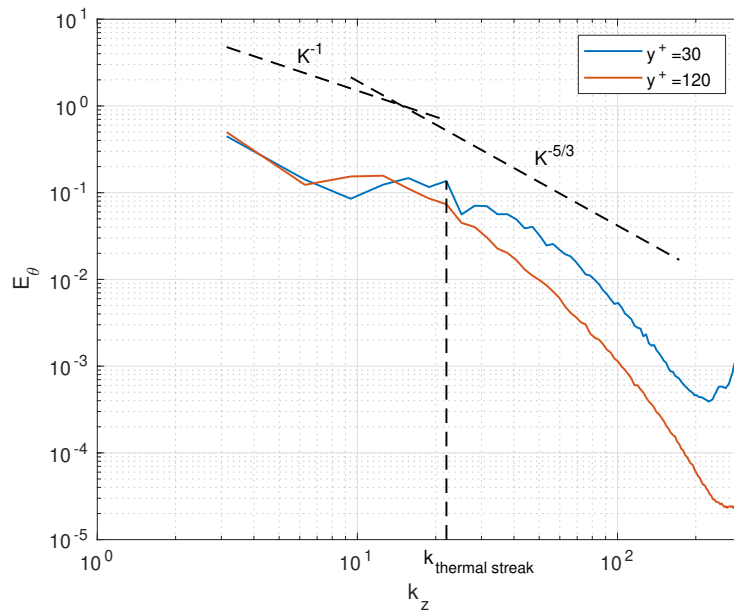
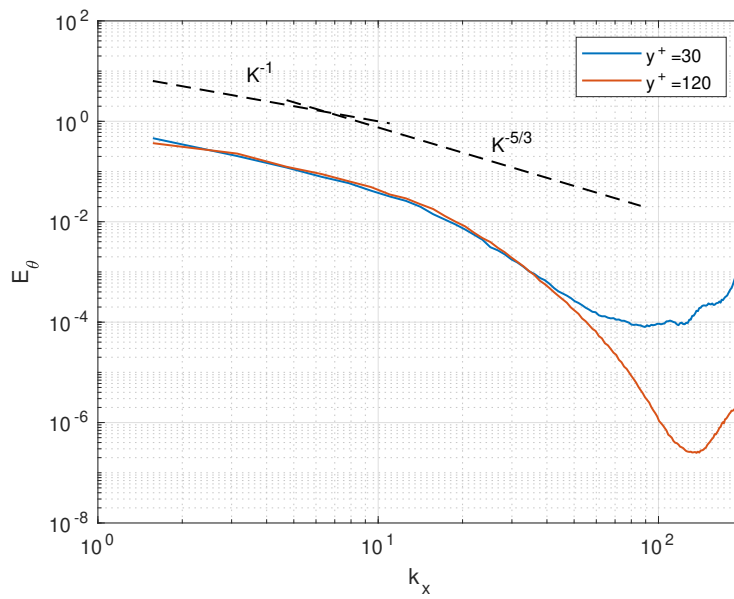
(a) *Temperature spectra in the spanwise direction*(b) *Temperature spectra in the streamwise direction*

Figure 5.21: Temperature spectra

for almost the whole wave numbers range. As can be seen in both the graphs of Figure 5.21, at high wave numbers the small scales seem to be more energetic than the larger ones. This can be related to the different magnitude of temperature fluctuations between water and air, i.e to a discontinuity between air and water temperature scales through the interface.

5.2.3 Wave height statistics

The time evolution of the wave height h' is shown in the left side of Figure 5.22 It is defined as the difference between the water depth and the mean water depth

$$h'(x, z, t) = h(x, z, t) - H$$

and it has been visualized by taking an isosurface of the volume fraction for $\alpha = 0.5$ and plotting the h' values on it. As shown in the visualizations small waves, inclined at 45 degrees with respect the streamwise direction, establish at the beginning. This regular state is then destroyed when the flow becomes fully turbulent ending up with higher and larger waves with a V-shape along the streamwise direction (see Figure 5.23 (a)). On the right part of figure 5.22 it is shown how the pressure distribution follows the wave pattern confirming the Philips'theory and highlighting the role of pressure fluctuations on wave formation. Obviously a more detailed analysis of the water surface state has to be performed, therefore the first, second, third and fourth order statistical moment of the water depth have to be computed:

- *the first order statistical moment* is represented by the mean of the water depth computed as:

$$H = \langle \tilde{H}(t) \rangle = \frac{1}{N} \sum_{i=1}^N \tilde{H}(t_n) = 0.150003m \quad (5.12)$$

Since its value is very close to the initial location of the interface, it possible to say that during the computation the interface dose not diffuse along the wall normal direction, as expected.

- *the second order statistical moment* is represented by the root mean square of the water depth computed as:

$$h_{rms} = \langle \tilde{h}'(t)^2 \rangle^{1/2} = \sqrt{\frac{1}{N} \sum_{i=1}^N \tilde{h}'^2(t_n)} = 2.27 \times 10^{-5} \implies h_{rms}^+ = 0.03 \quad (5.13)$$

As it can be seen, its values is comparable with the roughness length previously computed. This is a very important consideration because would be possible to derive y_0^+ starting by a measured value of h_{rms}^+ and vice versa.

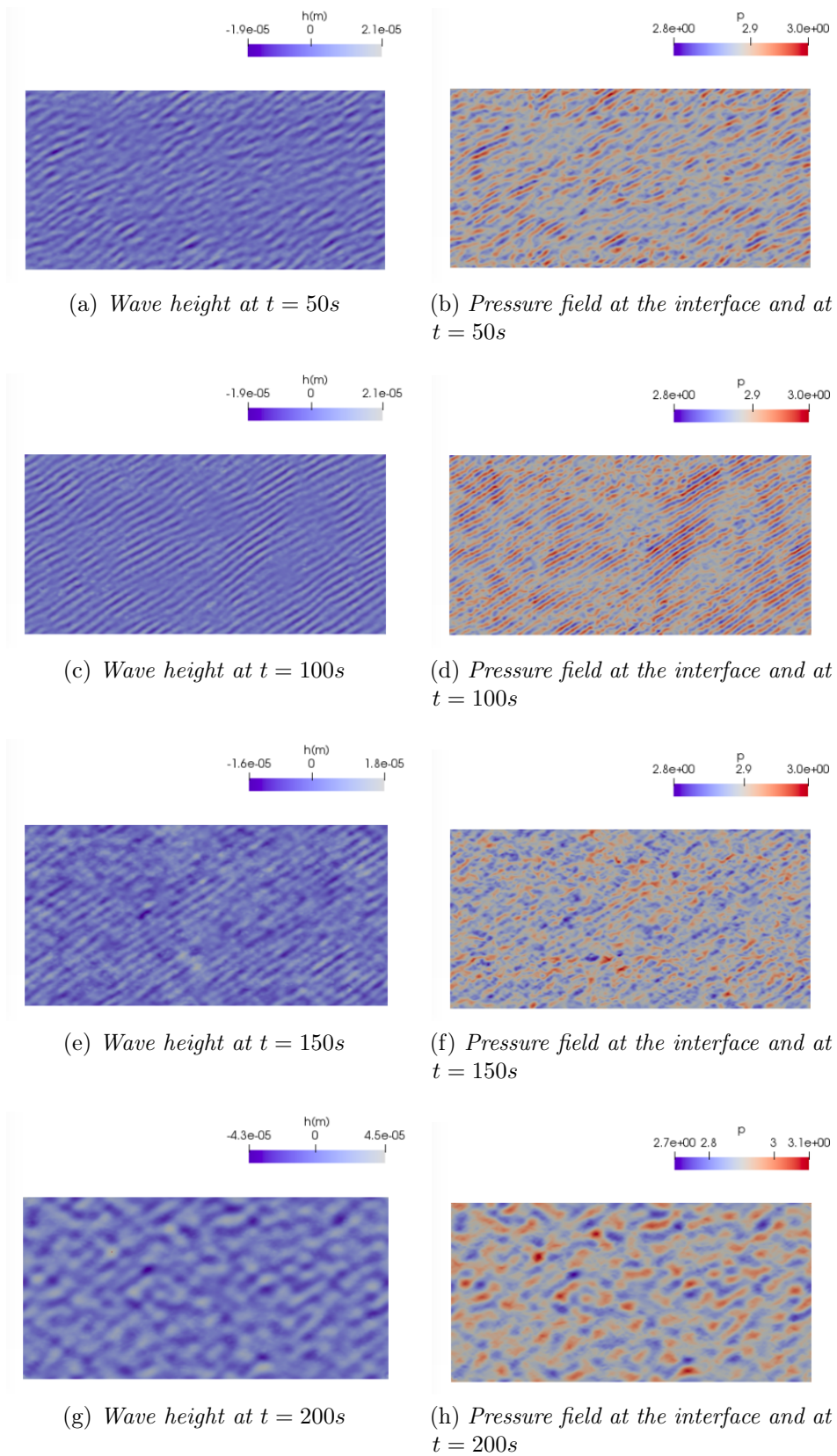
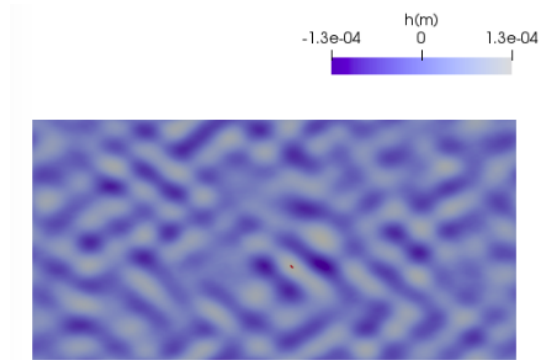
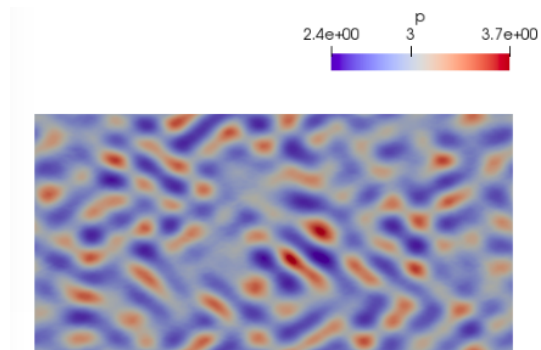


Figure 5.22: Wave height and pressure field at the interface during the transient



(a) *Wave height at $t = 410s$*



(b) *Pressure field at the interface and at $t = 410s$*

Figure 5.23: Wave height and pressure field at the interface after the stationarity

- *the third order statistical moment* is represented by the skewness computed as:

$$S = \frac{\langle \tilde{h}'(t)^3 \rangle}{\langle \tilde{h}'(t)^2 \rangle^{3/2}} = \frac{\frac{1}{N} \sum_{i=1}^N \tilde{h}'^3(t_n)}{\left(\frac{1}{N} \sum_{i=1}^N \tilde{h}'^2(t_n) \right)^{3/2}} = 0.023 \quad (5.14)$$

This variable says if waves with positive or negative heights dominate on the water surface. As a matter of fact if $S > 0$, positive fluctuations h' dominate, while if $S < 0$ the dominating fluctuations are the negative ones. Since the computed value for the skewness is very close to zero, it is possible to assert that positive and negative fluctuations occur with the same probability on the water free surface.

- *the fourth order statistical moment* is represented by the kurtosis computed as:

$$K = \frac{\langle \tilde{h}'(t)^4 \rangle}{\langle \tilde{h}'(t)^2 \rangle^2} = \frac{\frac{1}{N} \sum_{i=1}^N \tilde{h}'^4(t_n)}{\left(\frac{1}{N} \sum_{i=1}^N \tilde{h}'^2(t_n) \right)^2} = 4.57 \quad (5.15)$$

This variable is related to the probability of having rare events of large fluctuations of wave height along the water free surface. As a matter of fact, to a value of the kurtosis larger than the Gaussian value 3, it is associated a high probability to find large fluctuations of h . Since the computed value for the kurtosis is 4.24, it is possible to say that the wave motion is characterized also by rare events of large fluctuations of the elevation.

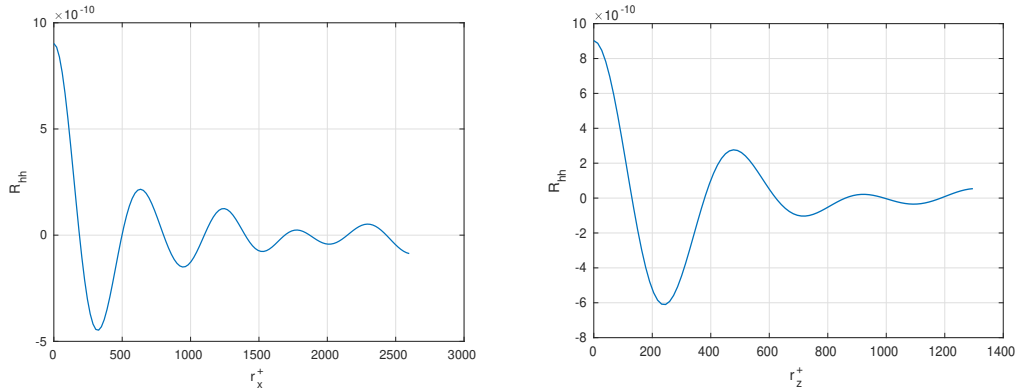


Figure 5.24: Two points correlations of wall-normal and streamwise velocity fluctuations

The wave distribution along the water free surface can be further investigated computing the two point correlation of the wave height, R_{hh} , in the streamwise

and spanwise directions:

$$R_{hh}(y, r_x) = \left\langle \frac{1}{N_x N_z} \sum_{i=1}^{N_x} \sum_{k=1}^{N_x} h'(x_i, y, z_k, t) h'(x_i + r_x, y, z_k, t) \right\rangle \quad (5.16)$$

$$R_{hh}(y, r_z) = \left\langle \frac{1}{N_x N_z} \sum_{i=1}^{N_x} \sum_{k=1}^{N_z} h'(x_i, y, z_k, t) h'(x_i, y, z_k + r_z, t) \right\rangle \quad (5.17)$$

In Figure 5.24 the plots, showing the correlation trend with respect to r_x^+ and r_z^+ , are presented. By looking at these graphs, it is possible to have an idea of the wave length and width. R_{hh} computed along the spanwise direction shows a second peak at $r_z^+ \approx 475$ that can be considered as the characteristic wave width. Similar considerations can be done for R_{hh} computed in the streamwise direction: the second peak occurs at $r_x^+ \approx 635$ that can be considered as the characteristic wave length. Both, in the streamwise and spanwise directions, the spatial correlation further shows oscillations. This behavior is a clear statistical footprint of the spatially repeated pattern taken by the wave motion.

In Figure 5.25 wave height spectra are reported in order to understand which wave numbers contains most part of the total wave energy. As it can be seen for

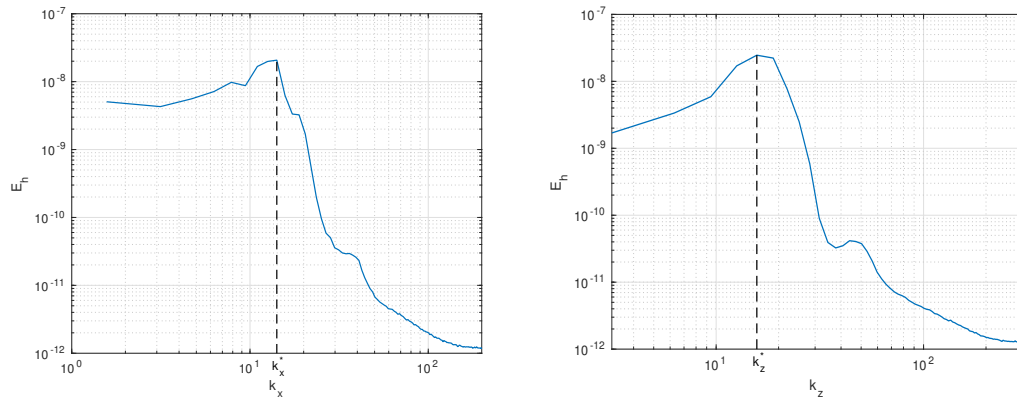


Figure 5.25: Wave height spectra computed along the streamwise and spanwise directions

the wave height spectrum computed along the streamwise direction, the peak is reached for $k_x^* \approx 14.13$ while for the one computed along the spanwise direction, a peak is localized at $k_z^* \approx 15.71$. These wavenumbers are typical of gravity waves, i.e. waves where gravity plays a much more important role than surface tension force. The characterization of waves as gravity waves is done by looking at the Bond number, a dimensionless parameter that measures the relation between gravity and surface

tension force and that is defined as:

$$Bo = \frac{\sigma k^2}{\rho_w g} \quad (5.18)$$

Since in the current case Bo is equal to 0.018, the gravity force has a much relevant role and the waves can be classified as gravity waves.

Additional parameters, coming from the linear wave theory, can be computed in order to have more informations about the wave state:

- *the frequency of the dominant wave* ω , defined as:

$$\omega^2 = \left(gk + \frac{\sigma k^3}{\rho_w} \right) \tanh(kh) \quad (5.19)$$

For deep water gravity waves, Eq 5.19 can be simplified to:

$$\omega^2 \approx gk \approx 154.11 \text{rad/s}^2 \quad (5.20)$$

- *the phase speed* c , defined as:

$$c = \frac{\omega}{k} \approx 0.79 \text{m/s} \quad (5.21)$$

- *the wave age* β , defined as:

$$\beta = \frac{c}{u_\tau} \approx 40.6 \quad (5.22)$$

Usually, from oceanographic references, if $\beta > 20$, than the waves can be considered in the fully developed wind sea regime.

Chapter 6

Laminar water channel

In this chapter the effect of a laminar air flow on the wave state will be evaluated in order to understand if some differences arise on the transitional wave state with respect to the case of a turbulent air flow. Therefore a new DNS of a two-phase flow will be investigated. It has been solved by means of *interFoam* solver and set with the same simulation parameters of the turbulent water channel except for the initial condition.

6.1 Initial Condition

The initialized velocity field is a continuous function with a Gaussian disturbance along the water free surface in order to develop turbulent faster. Therefore the initial velocity has been divided in two components: the component Ul linearly varying with the channel height and the component Ud representing the disturbance on the water free surface. The Ul component has been obtain by considering that it varies linearly with the wall normal direction with different angular coefficients in water and air:

$$Ul(y) = \begin{cases} Ul_w(y) = Ay + B & 0 \leq y \leq l_{water2} \\ Ul_a(y) = Cy + D & l_{water2} \leq y \leq l_{air} \end{cases} \quad (6.1)$$

In order to solve the system and find the A , B , C , D constants some constraints need do be satisfied:

1. the velocity $Ul(y)$ is maximum at the top boundary with a value equal to $1m/s$;
2. the velocity $Ul(y)$ is null at the bottom boundary;
3. the water and air velocities have to coincide at the interface;

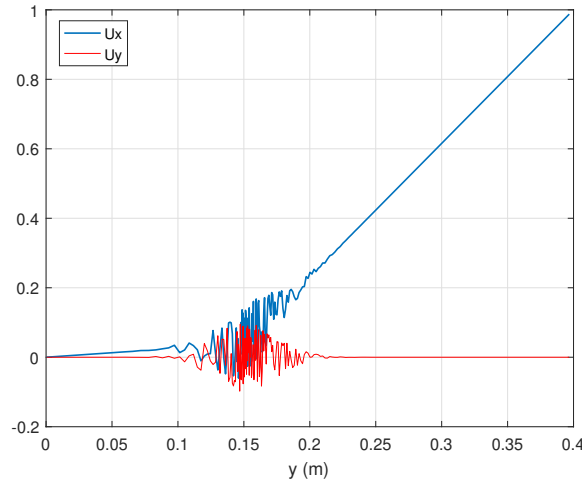


Figure 6.1: Initial velocity conditions

4. the ratio between the angular coefficients is fixed to be the ratio between the kinematic viscosity of water and air.

As regards the Gaussian disturbance, it can be expressed by:

$$Ud(x, y) = A(x, y)e^{-\frac{1}{2\sigma^2}(y-\mu)^2} \quad (6.2)$$

where $A(x, y)$ is a random amplitude function varying between $-0.1 < A(x, y) < 0.1$; σ is the standard deviation fixed to $\sigma = 0.025$ and μ is the mean value around which the disturbance is applied, represented by the water free surface initial position ($\mu = y_{interface}$). Summing up these 2 component $Ud(x, y) + Ul(y)$, the total initial velocity field shown in Figure 6.1 has been obtained. The spanwise component has been left without any initial profile in order to let the initial conditions to fulfill also the continuity equation. According to α and p_{rgh} , they has been initialized as for the turbulent water channel simulation.

6.2 Transitional wave state

In the present section the time evolution of the wave state will be visualized. In Figure 6.2 the wave height and the correspondent pressure field at the interface have been visualized. As can be seen, after the first seconds where the effect of disturbance is still present, the waves show an elongated shape along the spanwise direction. This different transient with respect to that observed for turbulent water channel, highlights how the wave pattern significantly depends on the main features of the air boundary layer at least in the transitional stage. Indeed, establishing

whether the fully developed state recovers or not the one observed for the turbulent water channel, exceeds the available computational resources. As a matter of fact, a simulation long enough to develop a turbulent air boundary layer from the initial laminar condition, would have been required.

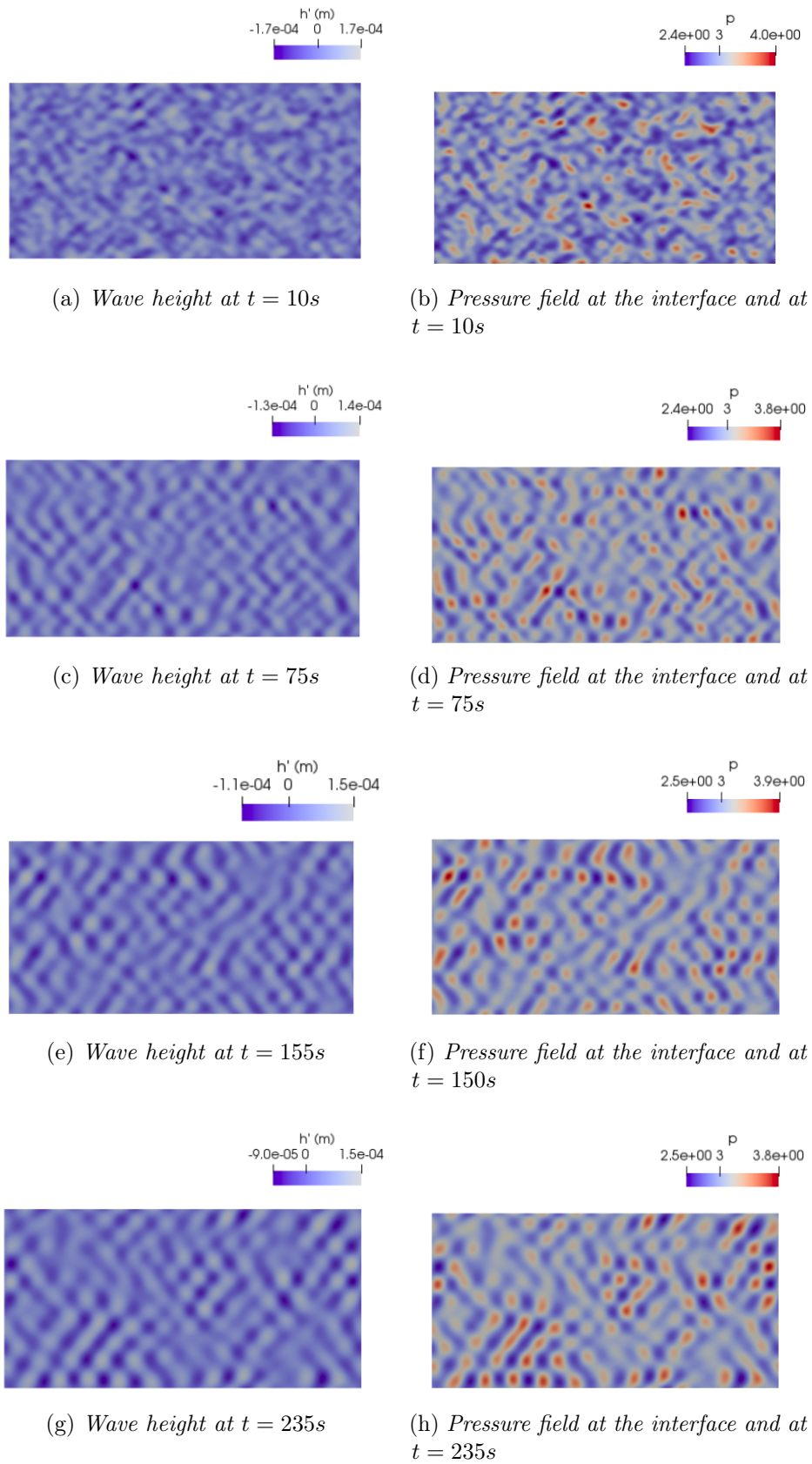


Figure 6.2: Wave height and pressure field at the interface during the transient

Chapter 7

Conclusions

The idea of this thesis arises from a particular interest in the interaction phenomena between atmospheric wind and ocean waves. As a matter of fact a full understanding of this mechanism could improve the actual large scale wind waves coupling models, which estimates the momentum and energy exchanges at the air-sea interface and that are used for wave and atmosphere prediction, climate forecast and loads estimation on marine structures. In order to evaluate the phenomena behind these transfers, the simulations of a single -phase and a two-phase open channel flow have been performed.

What has been found is the presence of larger and stronger turbulent structures close the water surface with respect to wall-bounded flow. They could be associated to a lower dissipative nature of the water surface, that determines a tendency of the turbulent kinetic energy to migrate towards the bulk rather than towards the water surface. This higher turbulent transfer feeds a strong reverse energy cascade in the space of spanwise scales that determine an intense turbulent energy transfer from small to large scale. This mechanism is at the basis of the development of large scale structures and challenge for turbulence theories and closures that should predict a flow of energy from nowhere in the space of small scales.

The transfer of heat has been also analyzed since, together with kinetic energy, is recognized to be of overwhelming importance for the dynamics of the atmospheric boundary layer over sea. A reduction of wall-normal heat flux close to the water surface and a consequent lower Nusselt number, have been observed. Contrary to the velocity, the temperature shows discontinuous behavior on the interface due to a very intensive dynamic also within water. This complex issue is due to interaction between different temperature scales determined by different values of thermal diffusivity and layer thickness in the air and water layers. As a result, the temperature spectra shows a pile up at high wave numbers. Such small scales are

inherently ineffective for the heat transport, thus implying a lower value of Nu .

The dynamics of the air flow shown above are obviously determined by the time and spatially evolving pattern taken by the water surface, which in turn has been created by the air boundary layer itself. For this reason, a statistical analysis of the wave elevation has been also performed. It has been possible to identify the developed waves as gravity waves and address the characterizing parameters computed with the wave linear theory. More over it has been observed a dependence of the transitional evolution of the the waves with the initial conditions of the atmospheric layer: considering air turbulent flow, inclined waves at 45 degrees with respect to the streamwise direction have been observed, while initializing the air flow in a laminar regime, elongated waves along the spanwise direction have been shown. Finally, it is envisaged possible interesting consequences by considering the analogy of the water surface pattern with the action of blow and suction traveling waves commonly used for turbulence control.

Ringraziamenti

Giunta al termine di questo secondo percorso di studi, i ringraziamenti a tutte le persone che con me hanno condiviso questo periodo non saranno mai abbastanza. Nel limite del possibile però, mi preme fissare nelle pagine di questo elaborato, quelle che di fatto hanno determinato un contributo decisivo per il raggiungimento di un traguardo così importante.

Un ringraziamento sentito va al relatore di questa tesi, il Professor Andrea Cimarelli. Il suo supporto costante e la sua continua disponibilità sono stati fondamentali nel conseguimento di questo lavoro. La profonda stima che nutro nei suoi confronti è il frutto, non solo di una grande esperienza e competenza nel campo della Fluidodinamica, ma della umanità con la quale ha saputo incoraggiarmi nei momenti di difficoltà.

Un ringraziamento particolare va alle due persone con cui è iniziato il mio percorso universitario: Giacomo e Francesca. Grazie perché nonostante le nostre strade si siano divise siamo riusciti a non perderci.

Ringrazio inoltre tutti gli amici incontrati a Forlì. Ogni momento, universitario e non, trascorso insieme ha reso questi due anni in indimenticabili e per questo non smetterò mai di ringraziarvi. Vi porterò sempre nel cuore.

Un ringraziamento speciale va a mia sorella Benedetta, che con la sua esuberanza e spensieratezza è sempre riuscita ad alleggerire i momenti più duri e stressanti. Grazie perché nonostante la lontananza in questi due anni ti ho sentita più vicina che mai.

L'ultimo ringraziamento, quello più grande e sentito, va alla mia famiglia e in particolar modo ai miei genitori, Mariella e Luigi. Non smetterò mai di ringraziarvi per avermi dato la possibilità e il privilegio di raggiungere questo importante traguardo. Vi sono grata per tutto il sostegno, l'amore e la comprensione che, soprattutto in questi ultimi anni, mi ha aiutato ad andare avanti con sempre più dedizione. Vi ringrazio per il coraggio con cui mi avete insegnato ad affrontare ogni ostacolo; per

tutti i sacrifici, talvolta anche considerevoli, che hanno permesso tutto questo, ma più di tutto vi ringrazio per avermi reso la persona che sono. Questo traguardo è mio come vostro. Spero di avervi reso orgogliosi di me.

Bibliography

- [1] Lorenzo Silvestri. *Numerical study of wind-wave interfacial phenomena*. Alma Mater Studiorum, 2017.
- [2] Owen M Phillips. *On the generation of waves by turbulent wind*. Journal of fluid mechanics, 3(2):185–204, 1957.
- [3] John W Miles. *On the generation of surface waves by shear flows*. Journal of Fluid Mechanics, 251:109–148, 1993.
- [4] Sullivan, P.P., Edson, J.B., Hristov, T., McWilliams, J.C.. *Large-eddy simulation and observations of atmospheric marine boundary layers above nonequilibrium surface waves*, J. Atmos. Sci. 65 (4), 1225–1245, 2008.
- [5] Jenkins, A.D., Paskyabi, M.B., Fer, I., Gupta, A., Adakudlu, M.. *Modeling the effect of ocean waves on the atmospheric and ocean boundary layers*, Energy Procedia 24,166–175, 2012.
- [6] Katsafados, P., Papadopoulos, A., Korres, G., Varlas, G.. *A fully coupled atmosphere–ocean wave modeling system for the Mediterranean Sea: interactions and sensitivity to the resolved scales and mechanisms*, Geosci. Model Dev. 9 (1), 161–173 2016.
- [7] George Varlas, Petros Katsafados, Anastasios Papadopoulos, Gerasimos Korres. *Implementation of a two-way coupled atmosphere-ocean wave modeling system for assessing air-sea interaction over the Mediterranean Sea* Atmospheric Research, Volume 208, Pages 201-217, 2018.
- [8] Jiménez, P.A., Dudhia, J., González-Rouco, J.F., Navarro, J., Montávez, J.P., García-Bustamante, E.. *A revised scheme for the WRF surface layer formulation*, Mon. Weather Rev. 140 (3), 898–918, 2012.
- [9] Arya, S. P.. *Introduction to Micrometeorology*, Academic Press, 307 pp., 1988.
- [10] Obukhov, A. M.. *Turbulence in thermally non-homogeneous atmosphere*, Tr. Inst. Teor. Geofiz. Akad. Nauk SSSR, 1, 95–115, 1946.

- [11] Panofsky, H. A. *Determination of stress from wind and temperature measurements*, Quart. J. Roy. Meteor. Soc., 89, 85–94, 1963.
- [12] Carlson, T. N., and F. E. Boland. *Analysis of urban-rural canopy using a surface heat flux/temperature model*, J. Appl. Meteor., 17, 998–1013, 1978.
- [13] Grell, G. A., J. Dudhia, and D. R. Stauffer. *A description of the fifth-generation Penn State/NCAR Mesoscale Model (MM5)*, NCAR Tech. Note NCAR TN-398-1-STR, 117 pp., 1994.
- [14] Komen, G. J., Hasselmann, S. and Hasselmann, K.. *On the existence of a Fully Developed Wind-sea Spectrum*, J. phys. Oceanogr. 14, 1271-1285, 1984.
- [15] Smith, S.D. *Coefficients for sea surface wind stress, heat flux, and wind profiles as a function of wind speed and temperature*, J. Geophys. Res.-Ocean. 93 (C12), 15467–15472, 1988.
- [16] Janssen, P.A.E.M.. *Wave-induced stress and the drag of air flow over sea waves*, J. Phys. Oceanogr. 19 (6), 745–754, 1989.
- [17] Janssen, P.A.E.M. *Quasi-linear theory of wind-wave generation applied to wave forecasting*, J. Phys. Oceanogr. 21 (11), 1631–1642, 1991.
- [18] Bidlot, J.R.. *Present status of wave forecasting at ECMWF*, Proceeding from the ECMWF workshop on ocean waves, 25-27 June 2012, reading, UK , 2012.
- [19] Jinhee Jeong, Fazle Hussain *On the identification of a vortex*, J. Fluid Mech., pp.69-94., 1995.
- [20] Vladimir Nikora, *Origin of the “21” Spectral Law in Wall-Bounded Turbulence*, National Institute of Water and Atmospheric Research, P.O. Box 8602, Christchurch, New Zealand, 24 December 1998.
- [21] C. W. Hirt AND B. D. Nichols, *Volume of Fluid (VOF) Method for the Dynamics of Free Boundaries*, Journal of Computational Physics 39, 201-225, 1981.
- [22] Ramshaw, J. D., Trapp, J. A. *A numerical technique for low-speed homogeneous two-phase flow with sharp interfaces*, J. Comput. Phys., 1976, Vol. 21, pp. 438–453.
- [23] Kolmogorov, *Dissipation of energy in locally isotropic turbulence*, Dokl. Akad. Nauk SSSR, , vol. 32, pp. 16–18 ,1941.